University of Pécs

Faculty of Sciences

Institute of Geography and Earth Sciences

Doctoral School of Earth Science

Numerical simulation of the fog

Ph.D. Dissertation

Submitted by:

Jeevan Kumar Bodaballa

Supervisor:

Prof. Istvan Geresdi

Pécs, 20th June 2022

Contents

1 Introduction **7**

2 Theoretical framework **11**

2.1 Köhler theory 11

2.1.1 Hygroscopicity parameter (κ) 15

2.2 Microphysics of liquid drops 17

2.3 Scavenging of aerosol particles in fog 19

2.4 Liquid chemistry in fog 23

2.5 Fog modeling 25

3 Model description **29**

3.1 1D model 29

3.2 WRF model description 31

4 Research objective **36**

5 Data & Methods **37**

5.1 Data observations 37

5.1.1 Observational data over Budapest 37

5.1.2 Observational data over Delhi 41

6 1D model results **45**

6.1 Time profiles of the fog evolution 45

6.2 The impact of the scavenging 47

6.3 The impact of liquid chemistry 52

6.4 WRF sensitivity results 56

6.4.1 Observations 56

6.4.2 Analysis of the model data 59

6.4.3 Liquid Water content (LWC) 62

6.4.4 Visibility calculation 65

7 Discussion **66**

8 Conclusions **70**

List of Figures

1 Kohler curve, here blue dotted lines denote the maximum value of the function and the location where it has the maximum value (critical radius & critical saturation). [Note: orange shaded region contain molecule clusters or haze particles, green shaded shows the activated droplets.] 13

2 Equilibrium saturation (S) as functions of (wet) diameter (D) for compounds with different hygroscopicity of $0.001 < \kappa < 1.2$ (Source: Nakao et al. (2014)) 16

3 (a) The molecular fluxes within one mean free path of the surface. (b) The exchange of momentum, (c) The mechanism which results in diffusiophoresis (Source: Young (1993)) 20

4 The dependence of the relative collection rate due to the Brownian effect (dashed line) and phoretic effect (solid lines) on the size of the aerosol particles (r_p). The symbols 's' gives the supersaturation in the environment of the water drops. These plots are evaluated in the case of droplet diameter of 10 μm 21

5 Schematic view of different physical processes involved in fog. 25

6 Approximation of the observed water drop size distribution by bin (a) and by bulk schemes. Black line with square is the observed size distribution, blue bars are bin distribution over radius ranges, red solid line indicate prescribed exponential distribution (bulk). 27

7 Topography of WRF model domain with observational sites (square indicates Pécs and star indicates Szeged) 32

8 (a): Satellite image of observational site from google maps, (b): Terrain plot of Hungary. 37

9 Evolution of fog detected by street cameras during the morning time at 01-Feb-2015. 38

10 Observed temperature (a), Relative humidity (b), and number concentration of aerosol particles at different size ranges over Budapest (c). (Note: vertical lines indicate fog onset and offset. The dotted line denotes time evolution of simulated total aerosol concentration.) Details about the BLK1 case can be found in the text and in Table 1 38

11 Fitted linear and power functions to give the fraction of NH particles for the whole spectrum. The red dotes denote the observed fractions. Note: LH and NH denotes less hygroscopic and nearly hydrophobic dry aerosol particles . 40
12 Initial size distribution of particles of observed and model input over Budapest and Delhi fog events. Observed dry aerosol size distributions are plotted in panels (a) and (b). Panel (c) and (d) reveal the distinction of aerosol particles into the categories of less hygroscopic (LH) and near hydrophobic (NH) over BLK1 and DSK1 cases. Size distributions plotted in panels (a) and (b) are used if the size dependence of the κ value is neglected. The legend in panel c denotes the way of the separation of LH and NH particles. 41
13 Observational site of India. Satellite image from google maps (a), terrain plot of Indo-Gangetic plain, India (b) 42
14 Observed temperature (a), Relative humidity (b), and number concentration of aerosol particles at different size ranges over Delhi (c). (Note: vertical lines indicate fog onset and offset. The dotted line denotes time evolution of simulated total aerosol concentration.) Details about the DSK1 case can be found in the text and in Table 1. 43
15 Evolution fog over Budapest (at 31 January 2015–1 February 2015) and Delhi (30–31 December 2016). Panel (a) and (b): Observed and calculated temperature and RH for Budapest and Delhi cases. Panel (c) and (d): Simulated LWC and visibility for both Budapest and Delhi cases. The vertical dashed lines indicate the model defined evolution periods of the fog, and solid lines show the observed fog onset and offset time. 45
16 Cumulative effect of Brownian and phoretic forces on scavenging process in (a): Budapest case and (b): Delhi case. (c): Efficiency of Brownian motion and that of phoretic forces in total scavenging rate. The total relative scavenging means the ratio of the scavenged particle concentration and the total initial aerosol concentration 48

17 Contour plots depict the time evolution of aerosol and haze/droplet size distribution for Budapest cases (BLK1 at first row and BMK1 second row). The vertical dotted lines denote the different phases of the fog (see the vertical dashed lines in Figure 14). r_{crit} means the critical radius for water drops at the supersaturation which occurs during the mature phase of the fog, LH and NH mean less hygroscopic and nearly hydrophobic dry aerosol particles, respectively. mean-κ means that all dry aerosol particles have the same hygroscopicity, D_{LH} denotes drops formed on LH particles. $D_{mean-\kappa}$ denotes drops formed on aerosol particles having the same hygroscopicity. The time evolution of the bin boundaries for the aerosol particles and liquid drops are depicted as it is given by the figure legend. 49

18 Contour plots depict the time evolution of aerosol and haze/droplet size distribution for Delhi cases (DSK1 at first row and DMK1 second row). The vertical dotted lines denote the different phases of the fog (see the vertical dashed lines in Figure 14). r_{crit} means the critical radius for water drops at the supersaturation which occurs during the mature phase of the fog, LH and NH mean less hygroscopic and nearly hydrophobic dry aerosol particles, respectively. mean-κ means that all dry aerosol particles have the same hygroscopicity, D_{LH} denotes drops formed on LH particles. $D_{mean-\kappa}$ denotes drops formed on aerosol particles having the same hygroscopicity. The time evolution of the bin boundaries for the aerosol particles and liquid drops are depicted as it is given by the figure legend. 50

19 Time evolution of the accumulated absorption of trace gases (panels (a) – (f)), bulk pH (panels (g) and (h)) and accumulated S(VI) (panels (i) and (j)). The different lines with different colors denote different cases (see the legends in panels (e) and (f)). 53

20 Mass concentration of $S(VI), NH_4^+, NO_3^-$ for the sum of the regenerated aerosol particles by the end of the dissipation phase for Budapest (a) and Delhi (b). 55

21 New hygroscopicity parameter for the regenerated aerosol particles at end of fog for the Budapest and Delhi cases. (a), (b) are the size independence hygroscopicity over Budapest and Delhi. (c), (d) are the chemistry independency hygroscopicity over Budapest and Delhi. 56

22 Satellite image of fog at 24-Nov-2020 07:10 CET (06:10 UTC). [Square symbol shows Pécs and Star symbol shows Szeged meteorological stations.] 57
23 Back scatter data from Pécs (a) and Szeged (b) on 24-Nov-2020 58
24 Time evolution of the surface meteorological parameters over Pécs and Szeged. Visibility data are plotted only at Szeged, because fog was not detected at Pécs. 58
25 Comparing the Pécs and Szeged weather station data with model 2 m temperature (a), (b) and relative humidity (c), (d) at different WRF PBL schemes. 59
26 Heat map of error statistics for the PBL sensitivity simulations over Pécs and Szeged for the observed fog period (see the vertical dashed line in Figure 25b and d). Note: P-MAE indicates the mean absolute error over Pécs and P-RMSE indicates root mean square error over Pécs. S-MAE indicates the mean absolute error over Szeged and P-RMSE indicates root mean square error over Szeged. 60
27 Before (a, d), during (b, e) and after (c, f) the fog vertical profile of temperature (1st row) and relative humidity (2nd row) over Szeged. 61
28 Time series of vertical profile of LWC over Pécs 62
29 Time series of vertical profile of LWC over Szeged 63
30 Histograms of the domain integrated LWC at different ranges at the simulation time of 24-Nov-2020 06:00 UTC (approximately at the middle of the fog period). 64
31 Spatial distribution of LWC at 24-Nov-2020 06:00 UTC at the altitude of 6 m. 65
32 Spatial visibility over 10 m height (first model level) at 24-Nov-2020 06:00 UTC 65

List of Tables

1 WRF model configuration and initial conditions 31
2 Major advantages and disadvantages of PBL schemes along with description. 33
3 Initial conditions with different hygroscopicity parameter (κ) and different gas concentrations (kg/kg) for Budapest and Delhi cases along with sensitivity test ID. (Note: * means constant SO_2 source throughout the simulation.) 39

4 Summary of maximum supersaturation (s_{max}), critical radius of droplet (r_{crit}) for the hygroscopic particles, total activated aerosols at s_{max}, maximum LWC, initial number concentration of the aerosol particles (N), scavenging and relative effect of Brownian and phoretic scavenging and total amount of scavenged particles during the period when RH>95%, change of maximum aerosol size ($\triangle r_p$) by the end of the dissipation period. 46

1 Introduction

Fog is a medium consisting of cloud water droplets suspended in the air, near the Earth's surface. Fog affects various socio-economical activities like aviation, public transport, shipping, agriculture both in Hungary and India. In Hungary the fog is predominantly observed during the winter months (December- February), it frequently spreads widely and lasts for days (average 48 h). However, only few papers have been published on Hungary's fog, and the accurate forecasting of the fog is challenging. Cséplő et al. (2019) analyzed data from different meteorological stations, studied fog climatology and explained fog events frequency by region (they found e.g. most of the fog events occur over northeast Hungary (Miskolc) and the least events are observed near lake Balaton (Siófok)). Vautard et al. (2009) also studied fog and mist over Europe and found that the frequency of fog, mist, and haze has declined in Europe over the past 30 years. Cséplő et al. (2019) asserts that most fog and mist events are reported in the morning time and the cause of these events is radiative cooling. During the past 10-15 years, there has been an increase in fog lifetime as decrease the fog events frequency in the country. Land-use changes and increasing pollution in the region are responsible for growing fog occurrence. Nevertheless, there is still no substantial evidence to support these statements due to a lack of understanding of fog's microphysical and meteorological conditions over Hungary. Apart from fog, other vital factors such as aerosol properties and their hygroscopicity have been studied by several researchers (Enroth et al., 2018; Molnár et al., 2016, 2020). This introduces formidable challenges for fog forecasting over the region. Since fog has large impacts on various sectors, especially in aviation, it is necessary to understand the physical characteristics, factors responsible for genesis, and intensity and ultimately develop reliable models for predicting different characteristics of fog. For the aviation sector, it is necessary to know whether a fog event will occur during the next 24 hours, if so, what could be its intensity when it will start and dissipate or the duration of the fog event.

On the other hand, Delhi is located in the Indo-Gangetic Plain (IGP), which encompasses 630 million acres of fertile land created from the floodplains of the Indus and the Ganga–Brahmaputra River systems those are extensively used for agriculture (Badarinath et al., 2009; Gautam et al., 2007). Usually, during the winter months, IGP is often enveloped by thick fog and haze layer (Gautam et al., 2007). During the winter months, Western Disturbances (WDs) cause light to moderate spells of precipitation over the northern

region of India, which induces a large amount of moisture into the lower troposphere through evaporation (Dimri et al., 2015). WD is an extra tropical storm originating in the Mediterranean region that brings sudden winter precipitation to the north-western parts of the Indian sub-continent. In addition, the dense network of the river systems, canals, irrigation networks, reservoirs, and other local water bodies also adds a significant amount of moisture into the lower atmosphere (Badarinath et al., 2009). A stable atmosphere, lower surface temperature for most of the night/day, and formation of surface-based solid inversions facilitate the development of thick fog above the ground surface (Jenamani, 2007). Recent studies on fog in India indicate that radiation fog generally forms in the rear sector of a WD that influences India during winter. In contrast, advection fog develops in the forward sector of the WD (Sawaisarje et al., 2014). Usually, advection fog in the IGP forms over varied time and spatial scales and shows a significant variability every year depending on the combination of local meteorological conditions and synoptic-scale weather systems (Badarinath et al., 2009; Dimri et al., 2015; Pasricha et al., 2003; Syed et al., 2012). Such fog events may be the fastest in formation, largest in spatial extension, and longest in duration, compared to any other fog area of the world (Ghude et al., 2017). During the past 10-15 years, there has been an increase in frequency and intensity of fog occurrence over the country's northern parts (Ghude et al., 2017; Jenamani, 2007; Syed et al., 2012).

The universal explanation of fog comprises a compilation of suspended water droplets or ice crystals near the Earth's surface that force a devaluation of horizontal visibility below 1 km (Gultepe et al., 2007). Fog forms, strengthen, and disperse as an arising of complex interactions among diverse local, microphysical, dynamical, radiative, and chemical processes, boundary layer conditions (Gultepe et al., 2007). The area's land surface processes and emission sources play a vital role in the moisture supply and it impacts the pollution concentrations, favoring the persistence of such hazy/foggy conditions for extended periods. Based on the formation and location, fog is classified into four types: radiation fog, advection fog, terrain-induced fog, and valley fog. Radiation fog is the most common form of fog formed by the nocturnal cooling of land due to infrared thermal radiation due to the clear sky and calm wind near the surface. It forms near the surface first and slowly thickens as the air continues to cool. Another type of fog is advection fog caused by cooling an air mass to the saturation point as it moves over a colder surface. The surface may be cold ground, snow cover, water, or ice. Unlike radiation fog, advection fog may form under cloudy skies with moderate to strong winds. Initial stability is not essential for

the formation of advection fog since the low-level cooling makes the air-stable near the ground, which allows the formation of the advection fog. Once the advection fog forms, it may move across the landscape, pushed by low-level winds. It can last for several days and is most common during the peak winter months.

The terrain-induced fog is usually formed in the hilly area. As moist air rises, it cools adiabatically, and saturation may result in the formation of upslope fog. Sometimes cold, moist air on-range flow may be blocked by a mountain range if the flow speed (kinetic energy) is not significant enough to lift air parcels upslope against the effects of negative buoyancy. The air parcel ascent initiates saturation on the mountain's slopes in blocked flow/stratus. Finally, the valley fog forms when the air near the ground cools, usually by radiation during the night. When the air cools, it becomes denser than its surroundings and sinks towards the valley's center. This results in a pool of cold air on the valley floor.

Several reviews and observations characterize the fog microstructure that fogs, unlike clouds, are characterized by small liquid water content (typically varying between 0.05 to 0.5 $g m^{-3}$ and tiny water drops (predominantly between 2.5 μm and few tens of micrometers with typical between mean diameter of 10 and 20 μm), low number concentrations (1 to a few hundred per cubic centimeter) (Pruppacher and Klett, 2010). Besides the liquid drops, tiny haze particles in the size range between the radius of 0.5 μm and 2.5 μm, with concentration of several thousand per cubic centimeter can be observed in fog (Garland, 1971; Pruppacher and Klett, 2010). Kunkel (1982) suggests that these haze particles are comprising wet aerosol particles that are not yet activated to form fog drops. Moreover, fog regulated by adjacent water bodies, the topography of the territory, prevailing winds, and readiness of aerosols suspended in the air arose from various natural origins and anthropogenic activities (Safai et al., 2018).

Recent studies in India have indicated that the heavy aerosol load and physical-chemical characteristics of the aerosols in the layer near the surface plays an intricate role in the entire life cycle of the fog (Gautam et al., 2007; Ghude et al., 2017; Mohan and Payra, 2014, 2009; Niranjan et al., 2007; Safai et al., 2008). Observations in India about the aerosol and fog water chemistry so far have indicated a highly polluted environment in which the fog developed. Secondary inorganic compounds like sulfate and nitrate were the dominant ions (38%) in the chemical constituents of fine particles during most of fog

events (Ghude et al., 2017). The chemical partitioning of fog water samples suggests that NH_4^+ (28%) and SO_4^- (26%) dominate the chemical composition. The pH of fog water indicates its alkaline (6.91) nature, NH_4^+ and Ca_2^+ was the major neutralizing component (Ghude et al., 2017). Overall, aerosol fog interaction leads to persistent hazy/foggy conditions for extended winter periods and creates poor air quality over the IGP during the winters (Ghude et al., 2017; Jenamani, 2007). Furthermore, rigorous model studies have been made to improve fog forecasting over this region (Pithani et al., 2018, 2019, 2020). However, there is considerable scope to improve forecasting and detailed understanding of fog microphysics and chemical properties during the fog life cycle.

Apart from fog the smog is one more serious concern in the boundary layer. Smog is air pollution that reduces visibility, and it can form in the same environmental conditions as fog forms. The term "smog" was first used in the early 1900s to describe a mix of smoke and fog. Smog was common in industrial areas and remains a familiar sight in cities today. Today, most of the smog we see is photochemical smog. Photochemical smog is produced when sunlight reacts with nitrogen oxides and at least one volatile organic compound (VOC) happens in the atmosphere. Nitrogen oxides come from car exhaust, coal power plants, and factory emissions. VOCs are released from gasoline, paints, and many cleaning solvents. When sunlight hits these chemicals, they form airborne particles and ground-level ozone or smog. Ozone can be helpful or harmful. The ozone layer high up in the atmosphere protects us from the sun's dangerous ultraviolet radiation. But when ozone is close to the ground, it is bad for human health. Ozone can damage lung tissue, and it is especially dangerous to people with respiratory illnesses like asthma. Ozone can also cause itchy, burning eyes (Dunn, 1989). Countries like India, China facing greatest challenges with smog episodes and mortality rate is more due to air pollution which can cause cardiovascular problems (Terry et al., 2018; Zhang et al., 2017). Cities located in basins surrounded by mountains may have smog problems because the smog is trapped in the valley and cannot be carried away by wind. Budapest locates in Carpathian basin with increasing urbanization which is serious concern to understand the air pollution role in absorbing traces gases and formation of new particulate matter.

This dissertation has been divided into seven chapters, including the current introductory chapter. The content and the essential features of each chapter are highlighted in the following paragraphs. The present chapter contains a brief introduction to the current

status and types of fog are frequent over Hungary. Chapter 2 gives the detailed theoretical framework of this work including literature on fog microphysics, such as aerosol activation based on hygroscopicity and favorable conditions of fog genesis and climatology. Chapter 3 discussed about model description of both 1D and WRF model. Chapter 4 provides the research objective of this work based on current challenges of understanding fog microphysics and liquid chemistry. Chapter 5 discusses two observational sites, data collection, model description, and methodology adopted in this research. Chapter 6 evaluates the model results that detailed fog time profile explanations (temperature, relative humidity, visibility, liquid water content), the importance of scavenging, and chemistry in fog. Also, this chapter explains the results about the new aerosol formation and changing their hygroscopicity. In the Chapter 6.4 mentioned the WRF model sensitivity experiment results. Chapter 7 and 8 gives the summary of the results and conclusions we got from this work.

2 Theoretical framework

The formation of fog in the atmosphere is possible due to a combination of thermodynamic and microphysical processes. Fog can form if a large volume of moist air cools below its dew point. The dew point temperature is defined as the temperature to which moist air must be cooled, at constant pressure and mixing ratio, for it to reach saturation. Foremost important to understand the activation and growth of droplet in the fog.

2.1 Köhler theory

Köhler's theory (Köhler, 1936) explains how the size and hygroscopicity of the aerosol particles impact the formation and growth of water drops by describing the ratio between the equilibrium vapor pressure over a solution droplet (e) to the saturation vapor pressure over a plane surface of water (e_{sat}) which depends exponentially on temperature (T). The relation between the supersaturation and temperature is described by the Clausius–Clapeyron equation:

$$\frac{de_{sat}}{dT} = \frac{L_v e_{sat}}{R_v T^2} \tag{1}$$

where L_v is the latent heat of condensation, T is temperature, R_v is the gas constant for water vapor. However, the saturation pressure depends not only on the temperature, but it is impacted by the radius and the chemical composition of water droplets (Pruppacher

and Klett, 2010):

$$e(T_d) = e_{sat}(T_d) \exp\left[\frac{2M_w\sigma_{w/a}}{RT_d\rho_w r_d} - \frac{\vartheta\phi_s\varepsilon_m M_w\rho_p r_p^3}{M_s\rho_s\left(r_d^3 - r_p^3\right)}\right] \tag{2}$$

where T_d is temperature at drop surface, M_w is the molecular weight of drop, $\sigma_{w/a}$ is the surface tension, ρ_w is the density of liquid water, R is the ideal gas constant and r_d is the radius of the droplet. ρ_p and ρ_s are the density of aerosols and solute, respectively. M_s is the molecular weight of solute, ϑ represents the degree of ionic dissociation of the solute (e.g., $\vartheta_{NaCl} = 2$), ε_w is the soluble fraction of the aerosol particle, ϕ_s is the molal or practical osmotic coefficient that accounts for solution non-idealities. r_p is radius of aerosol particles the droplet formed on. The first and second term in the bracket in above expression describe the curvature and solution effects, respectively. The first term means the increase in saturation vapor pressure that is associated with the formation of the surface (known as Kelvin law or curvature effect), and the second term means the decrease in saturation vapor pressure due to soluble substances in water (known as Raoult's law or solute effect). For homogeneous nucleation of pure water, the growth rate depends on the partial pressure and temperature of water vapor because this variable determines the rate at which water molecules impinge (strike) upon the molecule clusters. The decay of the droplet depends upon its temperature and surface tension. If the equilibrium is established between liquid and vapor, then the rate of condensation is equal to evaporation. Lord Kelvin 1870 (Kelvin, 1998), explained that the equilibrium vapor pressure over a curved liquid surface (droplet) is higher than over the plane surface:

$$\left.\frac{e(T_d)}{e_{sat}(T_d)}\right|_{curv} = \exp\left[\frac{2M_w\sigma_{w/a}}{RT_w\rho_w r_d}\right] \tag{3}$$

In the case of small droplets, the increase of the mass by condensation requires more energy to maintain the curvature than in the case of the flat-water surface ($r_d = \infty$). The molecules over the droplet surface evaporate more freely than the flat-water surface. Likewise, the condensation is more exceptional onto the droplets with small radius than the condensation onto the flat-water surface. Köhler's theory combines the curvature effect (Kelvin effect) and the solute effect (Raoult, 1887). The reduction of saturation vapor pressure over the surface due to the presence of the nonvolatile solute (dissolved solute in a solvent) is called the solute effect:

$$\left.\frac{e(T_d)}{e_{sat}(T_d)}\right|_{sol} = \exp\left[-\frac{\vartheta\phi_s\varepsilon_m M_w\rho_p r_p^3}{M_s\rho_s\left(r_d^3 - r_p^3\right)}\right] \tag{4}$$

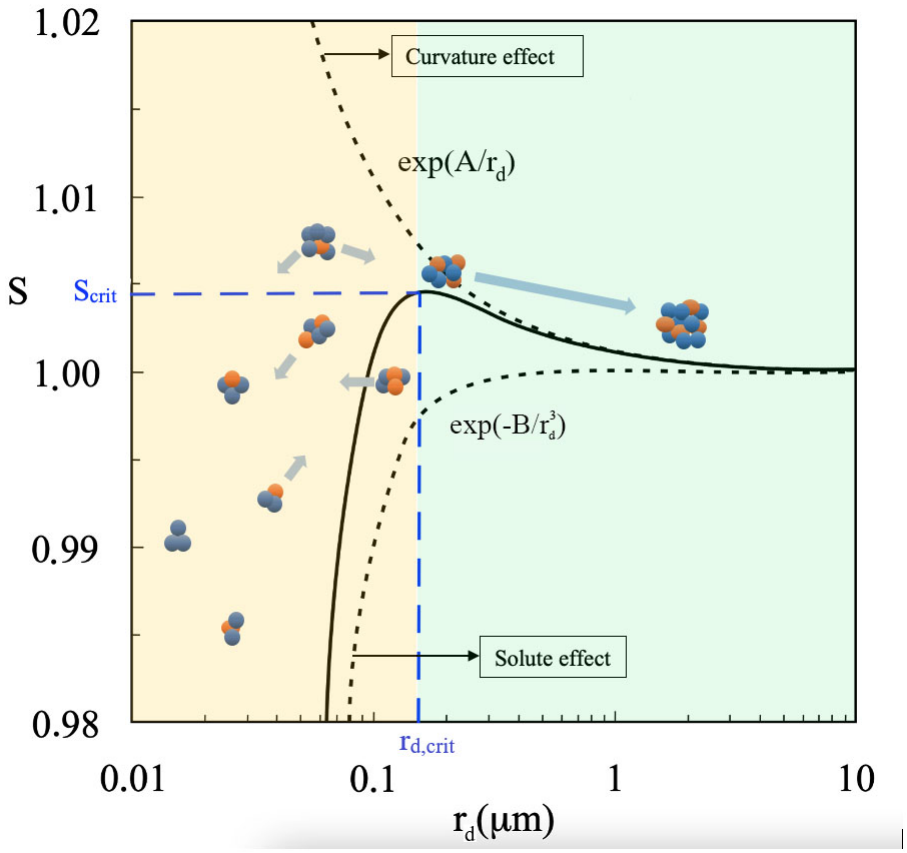

Figure 1: Kohler curve, here blue dotted lines denote the maximum value of the function and the location where it has the maximum value (critical radius & critical saturation). [Note: orange shaded region contain molecule clusters or haze particles, green shaded shows the activated droplets.]

The atmosphere contains aerosol particles which are composite of different chemical compounds. Depending on chemical composition these particles can be hydrophobic (non-water-soluble) or hygroscopic (water-soluble). Köhler's theory predicts how the aerosol particle's physico-chemical properties (i.e., solute mass, molecular weight, bulk density, dissociable ions, and activity coefficient) determine its ability to form droplet even in the case of decreasing trend of supersaturation. Köhler's curve equation is combination of curvature effect and solute effect as follow:

$$S(T_d) = \frac{e(T_d)}{e_{sat}(T_d)} = \exp\left[\frac{2M_w\sigma_{w/a}}{RT_d\rho_w r_d}\right]\exp\left[-\frac{\vartheta\phi_s\varepsilon_m M_w\rho_p r_p^3}{M_s\rho_s\left(r_d^3 - r_p^3\right)}\right] \tag{5}$$

If we consider $A = \frac{2M_w\sigma_{w/a}}{RT_w\rho_w}$, $B = \frac{\vartheta\phi_s\varepsilon_m M_w\rho_N r_p^3}{M_s\rho_s}$ and we neglect the r_p in the denominator because the radius of aerosol is significantly smaller compared to droplet radius (r_d). Then

equation can be written as follow

$$S(T_d) = \exp\left(\frac{A}{r_d}\right)\exp\left(-\frac{B}{r_d^3}\right) \tag{6}$$

Both the curvature and solution term in eq. 6 can be simplified by using first order Taylor series to evaluate these terms in simpler form. The error caused by this approximation steeply decreases with the increase of the drop size. It is less than 20 % if the drop diameter is equal to the 1.5 times of the aerosol diameter, and less than 2 % if the ratio of the drop diameter and the aerosol diameter is equal to 2, even in the case of aerosol diameter of 5 μm.

$$S(T_d) = \left(1+\frac{A}{r_d}\right)\left(1-\frac{B}{r_d^3}\right) \tag{7}$$

$$S(T_d) = 1+\frac{A}{r_d}-\frac{B}{r_d^3}-\frac{A}{r_d}\times\frac{B}{r_d^3} \tag{8}$$

We can neglect last term in right hand side of eq. 8 because its value is negligible comparing with the values of the other terms.
Finally, we have equation in simple form as follows:

$$S(T_d) = 1+\frac{A}{r_d}-\frac{B}{r_d^3} \tag{9}$$

This function frequently cited as Köhler curve or Köhler function. In Figure 1 the blue dotted lines denote the maximum value of the function and the location where it has the maximum value. The location of the peak of the Köhler curve is the barrier between the larger, activated droplets that can continue to grow even in the case of decreasing supersaturation. The smallerdroplets are in equilibrium with their environment. Saturation decreases with increasing droplet size due to releasing the latent heat and the decreasing vapor content and vice versa. The drops do not reach size of $r_{d,crit}$ are considered haze particles, and those are larger than $r_{d,crit}$ are considered drops (or activated droplets). The drop radius at this peak is called critical radius ($r_{d,crit}$) and the corresponding saturation is called critical saturation (S_{crit}). Following equations for $r_{d,crit}$ and S_{crit} can be obtained by differentiating the Köhler equation with respect to r_d and setting the derivative equal to 0:

$$r_{d,crit} = \left(\frac{3B}{A}\right)^{1/2} \tag{10}$$

Substituting this value into the eq. 9 we got the corresponding critical supersaturation:

$$s_{crit} = S_{crit} - 1 = \left(\frac{4A^3}{27B}\right)^{1/2} \tag{11}$$

If the value of aerosol radius (r_p) is not neglected in the solution term, the shape of the Köhler curve is different (see Figure 2):

$$S(T_d) = 1 + \frac{A}{r_d} - \frac{B \times r_p^3}{r_d^3 - r_p^3} \tag{12}$$

Where $A = \frac{2M_w\sigma_{w/a}}{RT_d\rho_w}$, $B = \frac{\vartheta\phi_s\varepsilon_m M_w\rho_N}{M_s\rho_s}$

The result for the activation drops radius at a given value of supersaturation (s) is:

$$r_{d,crit} = \frac{A(B - 3s + \sqrt{B(B+3s)})}{3s(B-s)} \tag{13}$$

Expressing eq.12 in terms of aerosol radius (r_p) we get critical radius of a dry aerosol particles ($r_{p,crit}$) which at a given supersaturation s becomes activated at drop radius of $r_{p,crit}$:

$$r_{p,crit} = r_{d,crit}\left(\frac{A - s \times r_{d,crit}}{A + r_{d,crit}(B-s)}\right)^{1/3} \tag{14}$$

The eq. 13 and 14 are frequently used to evaluate the critical drop radius and critical aerosol radius in the numerical simulation of the microphysical processes, if the model calculates the supersaturation.

2.1.1 Hygroscopicity parameter (κ)

The solute effect depends on the size and hygroscopicity (water uptake tendency) of the aerosol particles. The aerosol particles generally consist of different chemical compounds with different hygroscopicity. Petters and Kreidenweis (2007) introduced a parameter treat that the aerosol particles are not homogeneous with respect to the chemical composition. They suggest to evaluate the overall value of the hygroscopicity of an internally mixed aerosol particle (κ) as the weighted average of the hygroscopicity represent each chemical compound (κ_i):

$$\kappa = \sum_i \kappa_i \frac{V_{p,i}}{V_p} \tag{15}$$

where $V_p$and $V_{p,i}$ are the volume of the dry aerosol particles and the volume of each dry component, respectively.

The parameter κ_i represents the hygroscopicity of each dry component:

$$\kappa_i = \frac{\vartheta_i \phi_{s,i} M_w \rho_{p,i}}{M_{s,i} \rho_w} \tag{16}$$

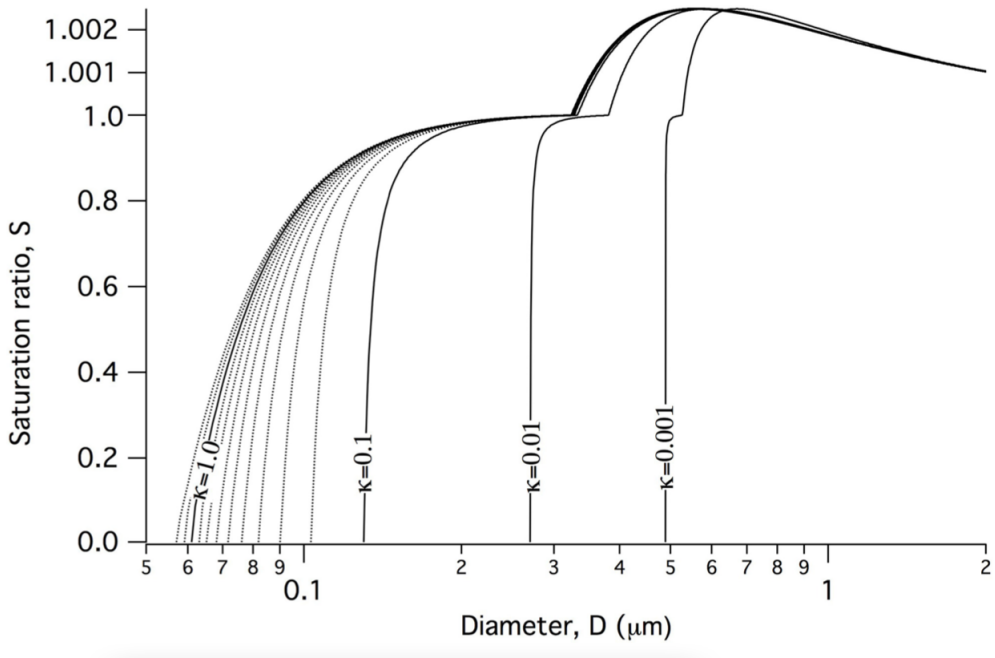

Figure 2: Equilibrium saturation (S) as functions of (wet) diameter (D) for compounds with different hygroscopicity of 0.001< κ < 1.2 (Source: Nakao et al. (2014))

For example, a research in a metropolitan area Wang et al. (2014) explained that more hygroscopic particles were made of aged background particles and that less hygroscopic mode particles were composed of organic carbon, pure elemental carbon (EC) particles, dust particles, and high-mass organic carbon compounds The κ value can be used in the Köhler model as a proxy for the chemical composition without explicitly knowing the density, molecular mass, van't Hoff factor and osmotic coefficient or dissociation number of each chemical component (Enroth et al., 2018). Generally, hygroscopicity value is varied between 0.5 and 1.4 for highly CCN active salts such as sodium chloride and between 0.01 and 0.5 for less hygroscopic particles such as organic species, and 0 for non-hygroscopic components (Nakao et al. (2014), Figure 2). Observations indicate that atmospheric particulate matter is typically characterized by $0.1 < \kappa < 0.9$ and the higher the

value of κ the less critical saturation and critical radius are needed for droplet activation (Figure 2). This parameter helps to reduce the complexity of solving the solute effect in Köhler's theory.

2.2 Microphysics of liquid drops

The growth of liquid drops by diffusion involves two processes. First, the water vapor is transferred to the drop surface by molecular diffusion in the vapor density gradient established around the drop. The condensation of water vapor onto the drop releases latent heat, thereby warming the drop. Since the rate of mass transfer is directly related to the difference in vapor density between the drop surface and its environment, the release of latent heat, which warms the drop, reduces its growth rate. Clearly, heat must be removed from the drop in order to permit the drop to continue to grow. This excess heat can be removed by conduction as the drop becomes warmer than its environment. Thus, both the mass flux of water molecules and the conduction of heat between the drop and its environment must be considered.

The diffusional growth of droplets will be introduced by considering the simplest case, that of an individual water drop grows due to the diffusion of water vapor. The impact of gas kinetic effects for small drops, and the enhancement of mass and heat transfer as the drop falls will be considered as they affect the growth (or evaporation) of the drop. The following equation describes the growth rate of liquid drops due to condensation:

$$\begin{aligned}\frac{dm_d}{dt} &= 2\pi D_d \frac{[S-1-\frac{4\sigma w_a}{R_v T \rho_w D_d}+\frac{\varepsilon \upsilon M_w m_p}{M_s(m_d-m_p)}]f_\upsilon}{\frac{L_\upsilon}{k_a^* T}[\frac{L_\upsilon}{R_v T}-1]+\frac{R_v T}{e_{sat,w} D_v^*}} \\ &= 2\pi D_d \frac{[S-1-\frac{4\sigma w_a}{R_v T \rho_w D_d}+\kappa\frac{\rho_w m_p}{\rho_p(m_d-m_p)}]f_\upsilon}{\frac{L_\upsilon}{k_a^* T}[\frac{L_\upsilon}{R_v T}-1]+\frac{R_v T}{e_{sat,w} D_v^*}}\end{aligned} \tag{17}$$

where m_d and D_d are the mass and the diameter of water drops (sum of liquid water mass and aerosol mass), respectively; m_p and ρ_p are the mass and the density of dry aerosol particles the drop formed on, respectively; M_w and M_s are the molecular weight of water and the compounds the aerosol particles are composed of, respectively. ε and ν are the water-soluble fractions of the aerosol particles and the van't Hoff factor, respectively. S, T, k_a^* and D_v^* are saturation ratio, temperature, the thermal conductivity of air, and the diffusivity of vapor in the air, respectively. $L_\upsilon, R_\upsilon, e_{sat,w}, \sigma$ are the latent heat of condens-

ation, specific gas constant for water vapor, saturated vapor pressure over liquid water surface at ambient temperature, surface tension, respectively. The κ (eq.15 and eq. 16) depends on the chemical composition of aerosol particles. The correction due to the gas kinetic effect is taken into consideration in the case of thermal conductivity and diffusivity (Pruppacher and Klett, 2010). The size distribution of these drops can be approximated by giving the number concentrations in size bins or using continuous functions. For example, the gamma-function is frequently used to describe the size distribution of small drops formed in clouds and fogs (e.g., Morrison et al. (2012):

$$N(D) = \frac{N_t}{\Gamma(n+1)} \lambda^{n+1} D^n \exp(-\lambda D) \tag{18}$$

where D is the particle diameter; n, λ and Γ are the shape, slope parameters and Euler gamma function, respectively. N_t is number concentration of drops. The mixing ratio of liquid drops (q_{cw}) is defined by following integral:

$$q_{cw} = \int m_d N(D) \cdot dD \tag{19}$$

Once the droplets reach certain size, they start to sediment due to terminal velocity which results in negligible amount of surface precipitation in the case of fog. The sediment of the drops depends on the gravity and drag force. Because the density of water (ρ_w) is much greater than the density of air (ρ_a), the buoyancy force can be neglected:

$$F_G = g\left(\rho_w - \rho_a\right)\frac{4}{3}\pi r_d^3 \approx g\rho_w \frac{4}{3}\pi r_d^3 \tag{20}$$

where g is the acceleration due to gravity. If the drop size is small (this is the case for fog drops) the Stoke's law describes the drag force impacts motion of drops (Young, 1993):

$$F_D = 6\pi\eta r_d v \tag{21}$$

where v is the falling velocity and η is the dynamic viscosity If the inertial and drag force are balanced the drops fall at constant velocity (defined as terminal fall velocity):

$$v_t = \frac{2\rho_w}{9\eta} g r_d^2 \tag{22}$$

If r_d = 10 μm the terminal velocity is about 0.003 ms^{-1}.

2.3 Scavenging of aerosol particles in fog

The primary sources of aerosols in urban areas are traffic and household, and their concentration is mostly affected by the advection, turbulent mixing, sedimentation, and scavenging processes. Scavenging can occur due to nucleation, or by impaction scavenging. Nucleation scavenging occurs if the aerosol particles act as cloud condensation nuclei (CCN) and liquid droplets, larger than the critical size form on them. Not all aerosols act as CCN due to their size and/or chemical composition. While the scavenging by nucleation strongly depends on the chemical composition of aerosol particles (Gilardoni et al., 2014), the impaction scavenges are affected mainly by the size of aerosol particles and that of collector water drops. However, wet deposition is the most dominant process of aerosol removal, and it transports aerosols to Earth's surface in the aqueous form such as rain, snow, hail or fog. The wet removal process can be split into two categories: in-cloud scavenging (washout) and below cloud scavenging (rainout). Nucleation and impaction scavenging are the main contributions in in-cloud scavenging (e.g., Pruppacher et al. (1998); Santachiara et al. (2012)). Numbers of observations and numerical model results have proven that in the case of clouds the nucleation of hygroscopic particles is the dominant scavenging mechanism in the washout of water-soluble aerosol particles (Elbert et al., 2000; Quaas et al., 2014; Steinfeld, 1998).
However, this does not necessary happen in the fog, where the supersaturation is generally less than 0.05%, and due to this low supersaturation, only a few percent of water-soluble aerosol particles are activated. The aerosol particles (nature by both hydrophobic and hygroscopic) smaller than 0.1 μm can remain as interstitial (un-activated wet particles) aerosol particles or can be scavenged by tiny drops in the fog. Because these small drops do not sediment (or they sediment very slowly), even most of the activated aerosol particles remain in the atmosphere after the dissipation of the fog. The impaction scavenging reduces aerosol number concentration by promoting wet removal and it can modify aerosol hygroscopicity and particle size distribution due to the collection of less hygroscopic particles by droplets (Gilardoni et al., 2014).

Different types of scavenging can occur in clouds/fog but mainly two types of scavenging processes are taking place in fog which are forced by Brownian motion and phoretic effect. The random motion of aerosol particles under bombardment by air molecules result in a net transportation in the direction of smallest aerosol concentration is called

Brownian motion/diffusion. The collection rate of aerosol particles with radius of r_p and with concentration of n_p by a water drop with radius of r_d is given by (Pruppacher and Klett, 2010):

$$\left.\frac{dn_p}{dt}\right|_{Br} = 4\pi r_w D_p f_p n_p \tag{23}$$

where D_p refers to the diffusivity of aerosol particles,

$$D_p = \frac{kT_\infty(1+N_{Kn})}{6r_p\eta_\infty} \tag{24}$$

where N_{Kn} being the Knudsen number (the ratio of the mean free path for air molecules to the radius of the aerosol), η referring to the dynamic viscosity and the subscripts ∞ referring to conditions at an 'infinite' distance from the drop, i.e., ambient conditions. n_p is the concentration of aerosol particles, f_p is the factor in Brownian collection rate corrects for the motion of the drop as it falls (Pruppacher and Klett, 2010). Review studies of Santachiara et al. (2012) asserted, that Brownian diffusion dominated drop scavenging of aerosol with a radius of less than 0.1 μm, and inertial impaction controls scavenging of aerosol with radius range higher than 1 μm. The particles in the size range of 0.1 μm - 1 μm can be collected at special environmental condition due to phoretic forces (Figure 3). Figure 4 shows how the collection efficiency due to the Brownian diffusion depends on the size of aerosol particles. The number concentration of small aerosol particles (r_p < 0.1 μm) is reduced due to this effect.

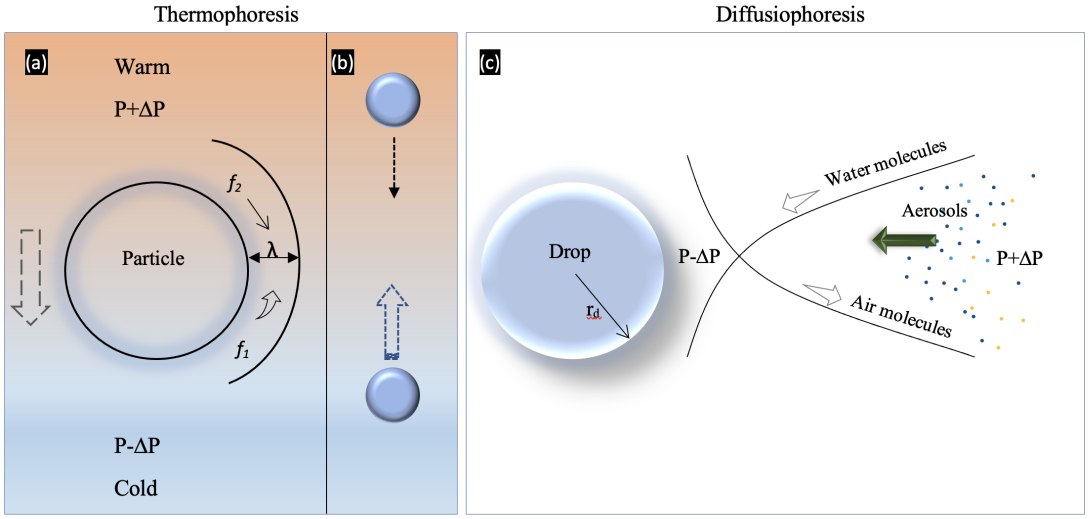

Figure 3: (a) The molecular fluxes within one mean free path of the surface. (b) The exchange of momentum, (c) The mechanism which results in diffusiophoresis (Source: Young (1993))

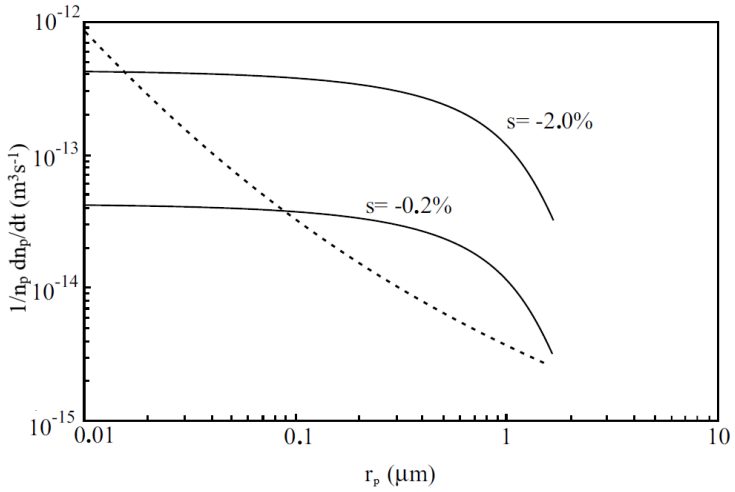

Figure 4: The dependence of the relative collection rate due to the Brownian effect (dashed line) and phoretic effect (solid lines) on the size of the aerosol particles (r_p). The symbols 's' gives the supersaturation in the environment of the water drops. These plots are evaluated in the case of droplet diameter of 10 μm

Phoretic force means the combination of two forces, which are thermophoresis and diffusiophoresis. Thermophoresis refers to the transport of aerosol particles in a temperature gradient, from warm to cold region (Young, 1993). Actually, there are two process responsible for thermophoresis. First there is molecular transfer from cold to warm along the edge of the aerosol within one mean free path of its surface (Figure 3a). Figure 3a shows, that since $f_1 > f_2$, there is a net flux from cold to warm region ($f_1 and f_2$ means flux from cold to warm and from warm to cold region, respectively), resulting in a pressure change (ΔP) which produces a hydrodynamic flow carrying the aerosol towards the cold side. Second, the exchange of momentum as particles arriving from the warm side lose momentum and particles arriving from the cold side gain momentum. The net result is to impart momentum to the aerosol, directed toward the cold side (Figure 3b).
The collection rate due to thermophoresis is given by the next equation (Pruppacher and Klett, 2010):

$$\left.\frac{dn_p}{dt}\right|_{Th} = 4\pi r_d^2 f_{th} \frac{Q}{p} n_p \tag{25}$$

where p is the atmospheric pressure, Q is the heat flux and f_{th} is the thermophoretic factor (see Pruppacher and Klett (2010)).

Whereas diffusiophoresis refers to the transport of aerosol particles in association with flux of vapor Young (1993). The water vapor field surrounding a growing drop is such that the vapor pressure increases with increasing distance from the drop. Since

the total pressure is assumed to be roughly constant, the pressure of the dry air must decrease with increasing distance from the drop (see Figure 3c). Water vapor diffuses toward the drop, where it condenses on the drop. The air molecules also find themselves in a concentration gradient and diffuse away from the drop. Since there is no source of air molecules at the drop surface, the partial pressure of the dry air (and also the total pressure) decreases in the vicinity of the drop and increases further away from the drop. This sets up a pressure gradient, resulting in a hydrodynamic flow called Stefan flow. The Stefan flow is in the opposite direction as the diffusive flux of condensing water molecules. The aerosol particle is carried with the Stefan flow, i.e., in the same direction as the diffusive flux of water molecules. It is incorrect to assume that the flux of water molecules is directly responsible for the movement of the aerosol particle. In addition to the Stefan flow the concentration gradients of molecules having different masses, contributes to diffusiophoresis Young (1993). The net effect of the thermophoresis and diffusiophoresis can be given by the following equation:

$$\frac{1}{n_a}\frac{dn_a}{dt}\bigg|_{Th+Ph} = \frac{4\pi r_d^2 s \cdot f_v \left[\frac{C}{\rho_a} - \frac{L_v f_{th}}{p}\right]}{\left[\frac{L_v}{k_a T}\left(\frac{L_v}{R_v T} - 1\right) + \frac{R_v T}{D_v e_s(T)}\right]} \tag{26}$$

where C is diffusiophoresis term (can be find more detail in Pruppacher and Klett (2010)). Because at general atmospheric conditions the sign of term in the bracket in the numerator is negative, the water drops can collect aerosol particles due to the phoretic effect only subsaturated environment (s < 0). The eq. 26 describes the total effectiveness of the phoretic mechanism in capturing the sub-micron particles by the droplets (Goldsmith et al., 1963; Santachiara et al., 2012).

Figure 4 depicts the efficiency of scavenging rate for the two mechanisms. Only Brownian effect depends strongly on the size of the aerosol particles, the collection rate decreases rapidly with increasing particle size. Phoretic effect is essentially independent of the aerosol size if the radius of the aerosol particle is less than 0.5 μm. However, the impact of the phoretic effect significantly depends on value of the subsaturation. While in the case of small subsaturation of -0.2% Brownian collection dominates for aerosol particles smaller than 0.1 μm, if the subsaturation is more significant (e.g., well under the cloud base) even the aerosol particles smaller than 0.01 μm are efficiently captured due to the phoretic forces.

2.4 Liquid chemistry in fog

Nevertheless, another critical factor in fog is the chemical composition of aerosol particles and the chemical processes occur inside of water drops. The size distribution and the chemical composition of aerosol particles are impacted not only by gas-phase chemical reactions but also by aqueous chemistry in fog drops. Fog is physically related to clouds, but the pollutant concentration in fog drops is usually higher than in clouds, as urban fog generally forms in a shallow boundary layer, which traps local emissions (Fisak et al., 2002; Li et al., 2011). Although fog cannot provide the amount of precipitation compared to rain, its chemical and biological composition could also affect many environmental processes (Cereceda et al., 2008; Collett et al., 2008). Furthermore, the dissolution of some ambient gases into droplets and their consequent aqueous-phase chemical reactions can impact the size and hygroscopicity of the aerosol particles (Kerminen and Wexler, 1995; Meng and Seinfeld, 1994). To understand this in detail (Fuzzi et al., 1998) carried out the Po Valley Fog Experiment which was a joint effort by several European research groups from five countries. The physical and chemical behavior of the multi phase fog system were studied experimentally by following the temporal evolution of the relevant chemical species in different phases (gas, droplet, solid interstitial aerosol). They tracked the evolution of micro-meteorological and microphysical conditions, from the pre-fog state, through the whole fog life cycle, to the post-fog period. Fuzzi et al. (1998) also conducted a second field project called CHEMDROP (CHEMical composition of DROPlets) that took place in the Po Valley region and measured the concentration of different trace gases (SO_2, NO_2, HNO_3, NH_3 ,and $HCHO$). They found, that three major ions ($NH_4^+, NO_3^-, SO_4^{2-}$) contributed nearly 90% in the fog water and pH varied in the range of 2.58 – 7.18 during all fog events. Gundel et al. (1994) also sampled fog water and interstitial particles for marine fog over California, USA. The major components of sea salt, Na^+, and Cl^- were the most abundant ions in fog water, followed by NH_4^+, SO_4^{2-},and NO_3^- in that order. They assumed that all the Na^+ at their site came from sea salt. Fog water pH ranged from 3.4 to 6.2 with a median and average of 4.0. Also Li et al. (2011); Nath and Yadav (2018); Nieberding et al. (2018); Safai et al. (2008); Straub (2017) made several observations about small aerosol particles (PM2.5), and they asserted, that the total ionic concentrations of such as $NH_4^+, NO_3^-, SO_4^{2-}$were larger during foggy nights than non-foggy nights and fog drops were more acidic in polluted regions. Li et al. (2011) found, that ion concentrations in fog droplet over Shanghai were often much higher than

those observed in other urban cities in North America, Europe, and Asia. Straub (2017) studied chemical composition of drops formed in radiation fog and its temporal trend over an eight-year period over Central Pennsylvania. They asserted, that the average sum of sulfate, nitrate, and ammonium was eight times greater in the Po Valley in Italy (Giulianelli et al., 2014), four times greater in Poland, 21 times greater in Shanghai (Li et al., 2011), eight times greater in Switzerland, and 13 times greater in Strasbourg, France than in Central Pennsylvania. Chemical composition of fog drops should be influenced significantly both by scavenging of aerosol particles and uptake of soluble trace gases due to the long residence time of the small droplets in the atmosphere. The chemical composition of fog water can vary as a function of droplet size, due to the inhomogeneous chemical composition of cloud condensation nuclei, differences in the rates of soluble gas uptake by small and large drops, and other factors (Li et al., 2011; Moore et al., 2004). Fog can promote the change of the chemical composition of aerosol particles through the fog droplets are serving as micro-reactors to convert some trace gases, e.g., SO_2, to secondary ones such as sulfates SO_4^{2-} through oxidation process. The rate of absorption/desorption of trace gases through the surface of water drops with radius rd can be calculated by the equation as follows (Pruppacher and Klett, 2010):

$$\frac{dc_l}{dt} = \frac{3D_g}{r_d^2}\left(c_{g,\infty} - \frac{c_l}{K_H^* RT}\right) f_v \tag{27}$$

where c_l and $c_{g,\infty}$ are the concentration of a gas in the drop and far from the drop, respectively; D_g is the diffusion coefficient of a given gas in the air, which depends on the temperature; r_d is the radius of the drop; f_v is the ventilation coefficient; K_H^* is the modified (due to dissociation) Henry coefficient; R is the universal gas constant, and T is the temperature.

The oxidation rate of the $S(IV)$ by H_2O_2 and by O_3 are given by equations as follow (Pandis and Seinfeld, 1989):

$$-\frac{d[S(IV)]}{dt} = \frac{k\left[H^+\right][H_2O_2]\left[HSO_3^-\right]}{1+K\left[H^+\right]} \tag{28}$$

where k = $7.5 \pm 1.16 \times 10^7 \mathrm{M}^{-2}\ \mathrm{s}^{-1}$ and K = $13\mathrm{M}^{-1}$ at 298 K temperature. (M is equivalent to $\mathrm{mol}\, l^{-1}$)

$$-\frac{d[S(IV)]}{dt} = \left(k_0\left[(SO_2)_{aq}\right] + k_1\left[HSO_3^-\right] + k_2\left[SO_3^{2-}\right]\right)[O_3] \tag{29}$$

where $k_0 = 2.4 \times 10^4, k_1 = 3.7 \times 10^5, k_3 = 1.5 \times 10^9 M^{-1}\ s^{-1}$

2.5 Fog modeling

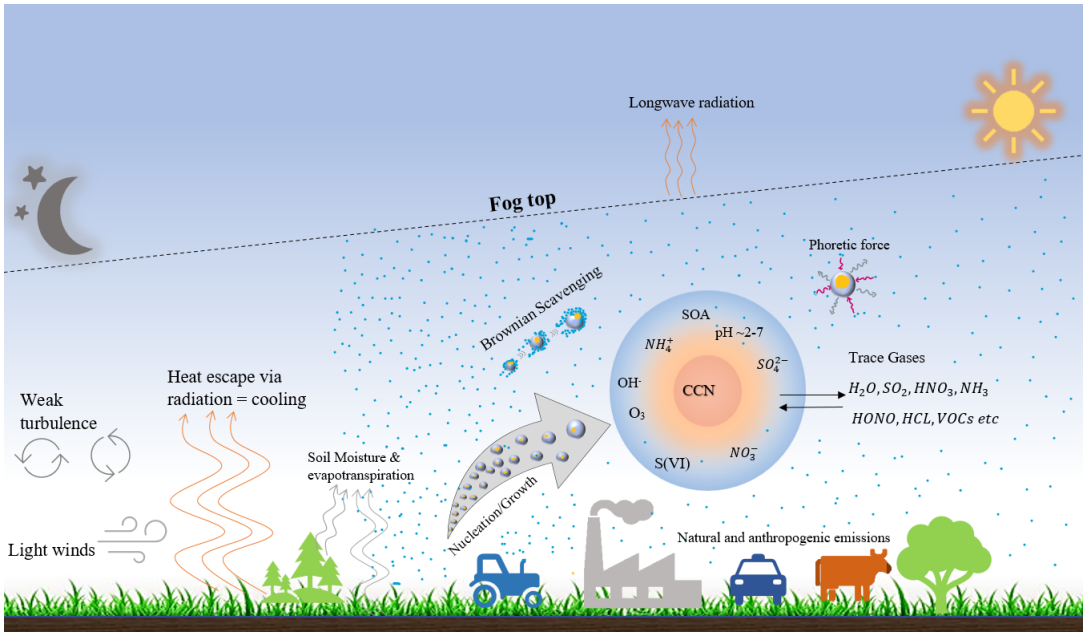

Figure 5: Schematic view of different physical processes involved in fog.

Numerical models include the description of physical and chemical processes occur in fog (Figure 5) at different complexities. Conventional mesoscale, weather prediction models have not yet adequately been developed for accurate predicting of fog formation and visibility conditions near the surface. There are several models available to simulate the weather, such as US Rapid Update Cycle (RUC) model (Benjamin and al., 2004), the Weather Research and Forecasting (WRF) model (Skamarock et al., 2008; William C. Skamarock, Joseph B. Klemp, Jimy Dudhia, David O. Gill, Dale M. Barker, Michael G. Duda, Xiang-Yu Huang, Wei Wang, 2001), the Consortium for Small Scale Modeling (COSMO) (Rockel et al., 2008), the Japan Meteorological Agency Non-Hydrostatic Model (JMA-NHM) (Saito et al., 2006), and the Canadian Mesoscale Compressible Community (MC2) model (Benoit et al., 1997). Among all models, WRF is widely used not only to forecast the weather, but also used for research purposes. However, these models have been focused the attention on the cloud formation, so the improvement of the microphysical and chemical processes occur in fog is required.

The WRF model has a broad spectrum of physical parametrizations representing the cumulus, microphysics, planetary boundary layer (PBL), atmospheric radiation, and land surface processes that account for the interaction between the atmosphere and the Earth's

surface. Depending on the model domain, spatial resolution, location, and application, researchers have been published results about different simulation performances using various combinations of physical schemes to simulate atmospheric processes. In the case of fog simulation, the prognostic variables are the dynamical variables (such as the three velocity components and the pressure), the thermodynamic variables (temperature) and the mixing ratio of water vapor and liquid water. If only the mixing ratio is available, the size distribution of the water drops is described by a prescribed function (e.g., eq. 15. This type of parametrization of the microphysical processes is called bulk parametrization. This parametrization is computationally efficient, but it does not allow to track the formation and evolution of the droplet spectrum. Furthermore, application of the bulk simulation can result in misleading conclusion in the case of the numerical simulation of the liquid chemistry (Schmeller and Geresdi, 2019). A wide range of WRF communities from all over the world made several sensitivity tests to perform weather simulations according to their requirements and areas of interest (Chaouch et al., 2017; Pithani et al., 2018, 2019). For example, in Delhi there was an extensive campaign on fog data collection and several sensitivity tests about WRF simulation were accomplished (Ghude et al., 2017; Pithani et al., 2018, 2019, 2020). The improved forecast are provided through their Government official site. Román-Cascón et al. (2019) compared the results of WRF and that of HARMONIE numerical weather prediction model, and concluded that both models have greater difficulties to forecast fog over Spain and WRF showed better performance simulate surface variables such as temperature, specific humidity, wind and turbulence. For radiation fog, both models showed inability to reach low surface temperature affected the fog simulation, except in some cases, when fog did not form, the saturation conditions were well simulated (Román-Cascón et al., 2019). Müller et al. (2010) studied model performance for fog over high complex terrain in Switzerland. They asserted, that the vertical structure of LWC inside the fog was mainly impacted by the sedimentation of cloud droplets, and in order to model the sedimentation accurately, a second-moment cloud water scheme should have been implemented. This means, that beside the mixing ratio another prognostic variable, the number concentration of the droplets should be evaluated in the model. In general, currently the numerical weather forecast models are inadequate to anticipate the fog periods, their specific location and time evolution (Mazoyer et al., 2019).

It is well-known fact that cloud microphysics is affected by aerosols particles through liquid and ice nucleation. An increase in aerosol concentration generally leads to more

numerous but smaller droplets for a given liquid water content, which results in a rise in the cloud albedo, known as the first indirect effect (Twomey, 1984). Even nowadays most of the NWP (numerical weather prediction) models simulate the impact of aerosol particles by using a fixed concentration of droplet neglecting the effect of spatial and temporal changes of size distribution and chemical composition of the aerosol particles. Thompson and Eidhammer (2014) introduced a new updated WRF microphysics scheme. They implemented a new scheme to improve the simulation of the impact of aerosol particles on precipitation formation. This aerosol-aware microphysics scheme allows to estimate the concentration of aerosol particles by using the output of Goddard Chemistry Aerosol Radiation and Transport (GOCART) model (Chin et al., 2002; Ginoux et al., 2001). The output of GOCART model includes major tropospheric aerosol types of sulfates, dust, organic carbon (OC), black carbon (BC), and sea salt aerosols, providing global distributions of aerosol mass concentrations, vertical profiles for mass distribution and optical thickness of each type of aerosols as well as that of total aerosols (Chin et al., 2002). Even these advancing model capabilities have inconsistencies to forecast the fog due to lack of detailed information of aerosol size distribution and their hygroscopic nature. Advanced study of the microphysics of fog with mesoscale NWP models is difficult due to strong interaction between the highly inhomogeneous surface and fog formed above it.

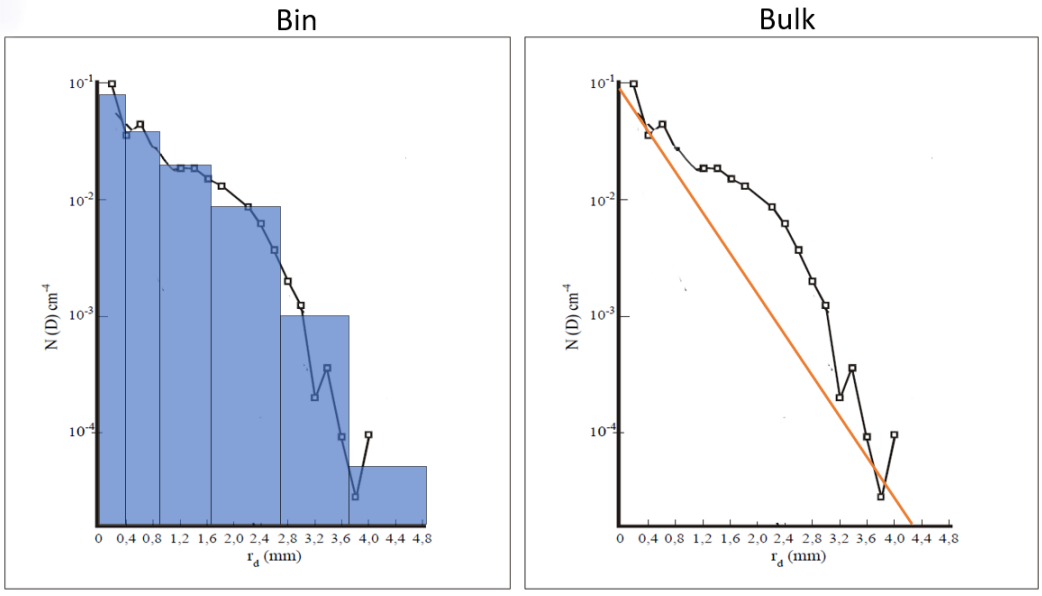

Figure 6: Approximation of the observed water drop size distribution by bin (a) and by bulk schemes. Black line with square is the observed size distribution, blue bars are bin distribution over radius ranges, red solid line indicate prescribed exponential distribution (bulk).

Generally, microphysics schemes are divided into two categories: bulk and bin microphysics. Bulk microphysics schemes predict one or a few variables that describe bulk properties of cloud hydrometers (e.g., mixing ratio of the liquid drops and ice particles) within a grid volume. Figure 6 shows the simplified illustration of bin and bulk schemes. A lot of information can be lost in bulk estimation compared to bin distribution. The bin microphysical schemes allow to track the evolution of the size distribution of both of aerosol particles and different types of hydrometers(e.g., liquid drops, snowflakes) without using any prescribed function. In the current study the number concentration of the droplets, furthermore the mixing ratio of liquid drops and the mass concentration of aerosol particles inside of the drops for each bin are prognostic variables. The size resolving bin scheme allows to integrate the diffusional growth rate equation (eq. 17) for any sizes of particles. So not only the growth of the drops formed on activated aerosol particles can be evaluated, but evolution of haze particles can be also taking into consideration. Because the numbers of the bins are near to 40 or larger, the number of the variables is significantly larger comparing to the bulk schemes. So, even nowadays, the application of this type of microphysical schemes is computationally too expensive, and it is generally used for only research purposes.

Due to the long lifetime of the fog and the low sedimentation of fog droplets, large number of gases can be absorbed by the fog and the chemical composition of the aerosol particles can be significantly impacted by the chemical reactions occur inside of the drops. However, only a few researches have focused on the liquid chemistry occurs inside of the drops (e.g., Jeevan Kumar et al. (2021); Schmeller and Geresdi (2019); Wang et al. (2016)). Bin scheme haven been used mostly to simulate both the formation and diffusional growth of water drops rather accurately, but the chemical processes occur in fog have not been studied. Besides, considering chemistry in fog models the greatest challenge is the lack of observational data about the trace gases and the chemical composition of aerosol particles to give initial condition and to validate the model. In our model, the liquid chemistry is also simulated by bin scheme. This increase further the number of the variables, because the concentration of the absorbed gases and the mass concentration of the sulfate are evaluated for each bin. Due to the requirement of the large computer resources one-dimensional (the independent variable is the time, hereafter 1D) dynamical models have been applied for the simulation of microphysical and liquid chemical processes occur in fog.

3 Model description

3.1 1D model

Fog formation was simulated using 1D model. Some dynamical processes (e.g., turbulent mixing, sedimentation of the water drops), which can be important in the evolution of the fog, were not taken into consideration since we focused on fog microphysics and the interaction between microphysics and chemistry in this approach. A detailed bin scheme with moving boundaries was adopted from Geresdi et al. (2005) to simulate the diffusional growth or evaporation of water drops (eq. 17). In the current research microphysics scheme with moving bin boundaries is implemented instead of fixed bins. The advantage of the moving bin method is that it inherently conserves the number concentration of particles and allows the tracking of aerosol mass inside of drops without numerical diffusion in mass. The model involves 28 bin categories in the Budapest case and 95 bins in the Delhi case (the number of the bins depends on the size resolution of the observation). Initially, the whole spectrum of bins extends from the mass of 1.22×10^{-22} to 1.02×10^{-15} kg and from 5.55×10^{-22} to 1.59×10^{-17} kg, respectively. The evolution of the haze particle and water droplet size distributions and the changing of the aerosol composition via chemical processes were calculated at each bin.

In our mode visibility is calculated as per the following equation (Silverman et al., 1974):

$$V = \frac{3.912}{\pi \sum_{i=1}^{n} K_i N_i r_i^2} \tag{30}$$

where N_i, $r_{d,i}$ are the concentration and radius of droplets/haze particles in the i^{th} particle size category (bin), respectively. K_i is the scattering efficiency, with a value of 2 regardless of the drop size. The size dependence of the extinction coefficient can be significant if the drop radius is less than 3 μm (Gultepe et al., 2006a; Song et al., 2019). However, our model sensitivity study proves that neglecting the size dependence of the extinction coefficient results in a false visibility value only in the case of haze. If the fog consists of drops larger than a few microns, the impact of the haze particles on the visibility is small.

The fog formation is simulated by holding the water content (sum of vapor and liquid) constant and decreasing the temperature gradually. The radiative cooling causes cooling of air mass, and changing the saturation is simulated by reducing the temperature at

prescribed rates. In simple terms, the fog evolution is mimicked by a prescribed cooling and warming rate based on the time evolution of the observed temperature. The impact of the latent heat of condensation and evaporation is taken into consideration for the prescription of the cooling and warming rate. The diffusional growth was calculated by integrating eq. 17 using a time step of 10^{-4} sec. The advantage of such a small-time step is the elimination of the potential error that caused by overestimating the impact of the solution and Kelvin effect. The diffusional growth of droplet formed on particles with different diameters and hygroscopic properties can be calculated in parallel. The terms in the square brackets in eq. 17 describe how the curvature and solution effects impact the growth rate of water drops and give the diffusional growth of an individual drop, however the fog consists of drops with different sizes. Using the above-mentioned small-time step, the competition for available vapor among drops with different sizes and different types and sizes of aerosol particles inside them can be evaluated accurately. In the numerical simulation the formation of haze particles is initiated as the saturation ratio reaches the value of 95%. The initial mass of the haze particles is supposed to be double the mass of the aerosol particles they formed on.

Both microphysical and chemical processes are simulated in current research. In the diffusional growth equation, we used hygroscopicity parameter to describe the solution effect. This size dependence hygroscopicity parameter is explained in sections 2.1.1 and 5.1. Later we extended some sensitivity tests with different hygroscopicity parameter and trace gas concentrations (see details in Table 3). Theory published by Pruppacher and Klett (2010) is used to evaluate the impact of Brownian and phoretic impaction scavenging. While Brownian scavenging is efficient if the aerosol size is less than 0.1 μm, phoretic scavenging can reduce significantly the concentration of aerosol particles with a radius of about 0.1 μm (Santachiara et al., 2013). The latter process persists only in a subsaturated environment during either the formation or dissipation of the fog. In this study the effect of gravitation collection (efficient for the aerosol radius larger than 1.0 μm) and scavenging due to the turbulent motion of the atmosphere are neglected, we focus on the scavenging due to Brownian motion and phoretic forces. The scavenging of particles with a radius less than 1 μm, both dry aerosol particles and haze particles, due to the Brownian motion and phoretic scavenging are calculated separately by using eq. 23 and 26. The absorption and desorption of the trace gases of $SO_2, NH_3, H_2O_2, HNO_3, O_3$, and CO_2 are calculated by using eq. 27. Sulfate formation in the liquid phase due to oxidation of $S(IV)$ by O_3 and H_2O_2 is evaluated by using eq. 29. The amount of the dissolved trace gases and sulfate

formed due to the chemical reaction were evaluated for each bin with a droplet radius larger than 1 μm. The stiff, ordinary differential equations about the chemical processes are solved by using implicit Euler scheme with time step of 10^{-4} s.

3.2 WRF model description

Several sensitivity experiments have been accomplished to study how the accuracy of fog forecast depends on planetary boundary layer (PBL) schemes implemented in the WRF Advanced Research Core (ARW, V4.3). The horizontal extension of the model domain is 800 km × 740 km with horizontal spatial resolution of 2 km. The domain covers whole Hungary and some part of Hungary's neighbor countries Austria, Croatia, Bosnia, Serbia, Romania, Ukraine, and Slovakia. We use Lambert coordinate configuration with center at (47°N, 19°W) to define the domain, and 61 vertical levels (18 levels below 1000 m and 8 levels below 100 m). The large vertical spatial resolution under 100 m allows to properly simulate the vertical structure of the fog and to resolve the inversion layer formed at the top of the fog.

Table 1: WRF model configuration and initial conditions

Version	4.3
Initial Boundary conditions	WRF-ECMWF
Model Domain and resolution	400 x 370 grids (2km)
Land use and land category	USGS
Vertical resolution	61 vertical levels (18 levels below 1000m & 8 levels below 100m)
Radiation Scheme (LW & SW)	RRTMG
Microphysics scheme	Aerosol-aware Thompson Scheme
Land Surface physics	Noah-mp land surface model
PBL & Surface layer physics	• YSU & MM5 (Monin-Obukhov scheme) • Eddy-diffusivity mass flux (QNSE) & QNSE. • MYNN3 & MYNN • ACM2 & Pleim-Xiu
Spin up	4 hrs (Model initialized at 18:00 hr UTC)
Total duration	36 hrs

Meteorological initial and boundary conditions are provided by reanalysis products of the European Centre for Medium term Weather Forecasting (ECMWF). ERA5 data are operational global analysis available on $0.25^\circ \times 0.25^\circ$ grids with 1 h temporal resolution. For the mesoscale simulations, the geographical data for the land-use and topography are obtained from the standard U.S. Geological Survey dataset (Figure 7). Initial conditions at 23 November 2020 1800 UTC are selected for simulation of the fog.

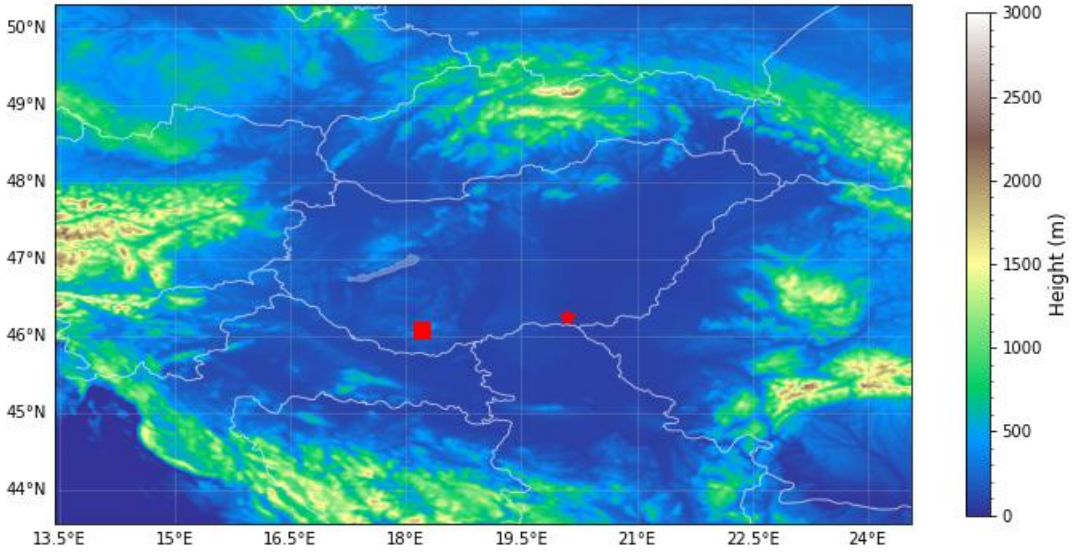

Figure 7: Topography of WRF model domain with observational sites (square indicates Pécs and star indicates Szeged)

The following parameterization schemes are set to simulate the different physical processes: (i) the rapid radiative transfer model (RRMTG) for both longwave radiation and shortwave radiation (Iacono et al., 2008); (ii) the Thompson aerosol aware two – moment bulk scheme for microphysics (Thompson and Eidhammer, 2014), (iii) Noah land surface scheme to simulate the impact of the soil and land use (Chen and Dudhia, 2001). The advantage of Thompson and Eidhammer (2014) scheme, comparing with other bulk microphysics scheme, is that it able to take into consideration the spatial variability of the concentration of aerosol particles impact both the drop and ice formation. This microphysics scheme allows to evaluate not only the liquid water content (hereafter LWC), but the number concentration of liquid drops explicitly as well. The calculation of prognostic variable of number concentration of liquid drops not only results in more reliable forecast for the fog formation, but also improve the accuracy of the evaluation of the visibility. The PBL schemes and surface layer (SFC) formulations are set to be different in each experiment. PBL schemes parameterize turbulent vertical fluxes of heat, momentum, and components like moisture in the PBL. Because some of PBL schemes are

suggested tightly coupled to particular surface layer schemes in WRF, it is not possible to have a common surface layer scheme for all experiments. In this case study, we evaluate four PBL schemes, MYNN3.0 (Nakanishi and Niino, 2006), YSU (Hong et al., 2006), QNSE (Sukoriansky et al., 2005) and ACM2 (Pleim, 2007). The considered four PBL schemes and the coupled surface schemes are given in Table 1. Cohen et al. (2015) aserted that MYNN3.0 was reasonably good at the simulation of radiation fog development. The YSU scheme enhances mixing in the stable boundary layer by increasing the critical bulk Richardson number from 0 to 0.25 over land (Chen et al., 2020). The ACM2 scheme (Pleim, 2007) was elaborated to improve the shape of vertical profiles of temperature and dew point temperature near the surface. Both nonlocal (YSU & ACM2) schemes may lead to strong vertical mixing, sometimes resulting in drier and warmer daytime PBLs. In the local scheme, the eddy-diffusivity is determined independently at each point in the vertical, based on local vertical gradients of wind and potential temperature. The non-local scheme determines an eddy-diffusivity profile based on a diagnosed boundary layer height and a turbulent vertical scale (Mihailovic, 2006).

Table 2: Major advantages and disadvantages of PBL schemes along with description.

PBL Scheme	**Description**	**Advantage(s)**	**Disadvantages(s)**
YSU	First-order closure; and it represents entertainment at the top of the PBL explicitly	More accurately simulates deeper vertical mixing in buoyancy-driven PBLs with shallower mixing in strong-wind regimes (Hong et al., 2006)	The depth of the PBL is overestimated for springtime deep convective environments, resulting in too much dry air near the surface and underestimation of convective available potential energy in mixed layer related to environments of deep convection (Cohen et al., 2015)

ACM2	First-order closure; it represents the upward fluxes within the PBL as interactions between the surface layer and each and every layer above (with local eddy diffusion also included); while downward fluxes extend from each layer to each immediately underlying layer; this represents convective plumes arising from the diurnally heated surface layer, whereas downward fluxes are more gradual.	Pleim (2007) indicates that the profile of potential temperature and velocity through the PBL are depicted with greater accuracy when both local and nonlocal viewpoints are considered regarding vertical mixing (ACM2); further validates the use of the ACM2 scheme owing to its support of PBL heights similar to those based on afternoon.	Coniglio (2012) reveals that this scheme results too deep PBL layers.
QNSE	1.5 order local closure and is intended to account for wave phenomena within stable boundary layers.	Provides realistic depiction of potential temperature profiles, PBL height, and kinematic profiles based on observational data and corresponding large eddy simulations (Cohen et al., 2015) for its designed environment (stable conditions).	In the case of the less-stable PBL, QNSE depicts too cool, moist, and shallow PBL in the case of simulations of springtime convective environments.

MYNN3	Second-order closure schemes; expressions of stability and mixing length are based on the results of large eddy simulations rather than on observations, while the expressions of mixing length are more applicable to a variety of static stability regimes.	MYNN3 more accurately portrays deeper mixed layers and reasonably depicts statically stable boundary layer simulations supporting radiation fog development (Nakanishi and Niino, 2006).	It still may not fully account for deeper vertical mixing associated with larger eddies and associated counter gradient flux correction terms (Cohen et al., 2015).

Table 2 shows the major advantages and disadvantages of PBL schemes and furthermore detailed information about all applied PBL schemes applied in this study can be found in following papers: Chaouch et al. (2017); Cohen et al. (2015); García-Díez et al. (2013); Pithani et al. (2019).

4 Research objective

Budapest and Delhi are the capital cities of Hungary and India, respectively. These cities have different characteristics based on population density, traffic, industrialization, and agricultural activities. In Hungary the fog is also frequent phenomena during the winter. The interaction between air pollution and fog can also result in a weather situation that can cause a serious emergency or economic damage. Such is the drastic reduction in visibility, the formation of dense fog, smoke in the cities, which can, among other things, make aviation impossible and causes serious accidents in road transport. Since fog has a very high damage potential (physical as well as economical), it is necessary to develop objective tools for forecasting the characteristics, such as timing of onset, intensity, and duration of fog well in advance. For better fog forecasting it is not enough to understand large-scale to mesoscale, micro-meteorological processes, but it is essential to know more about the microphysical processes occur in fog to improve the parameterization of these processes.

Main aims of this research:

- Understand the impact of hygroscopicity and size distribution of aerosol particles on the fog formation.
- Understand the impact of the scavenging process in the wash out of the aerosol particles during the fog event.
- Understand the impact of the chemical process occur in the fog droplets on changing of size and hygroscopicity of the aerosol particles.
- Evaluate the WRF model performance in fog prediction.

Most of the results shown in this dissertation have been recently published in Jeevan Kumar et al. (2021). The manuscript includes the results about the WRF simulation is intended to submit soon.

5 Data & Methods

5.1 Data observations

5.1.1 Observational data over Budapest

In this study, we used data from two different observational sites in two countries which are Budapest, Hungary, and Delhi, India. For the Budapest case, the size distribution and hygroscopicity of the aerosol particles were obtained in a field project at the Budapest platform for Aerosol Research and Training (BpART) Lab (Figure 7 in Salma et al. (2016)) in Budapest (47.474° N, 19.062°E) from 9 December 2014 to 9 February 2015 (Enroth et al., 2018). The observational setup was located at 114 m above mean sea level, at 85 m distance from the river Danube, and at the height of 12-13 m from street level (Figure 8a). More details about the experiments can be found in Enroth et al. (2018).

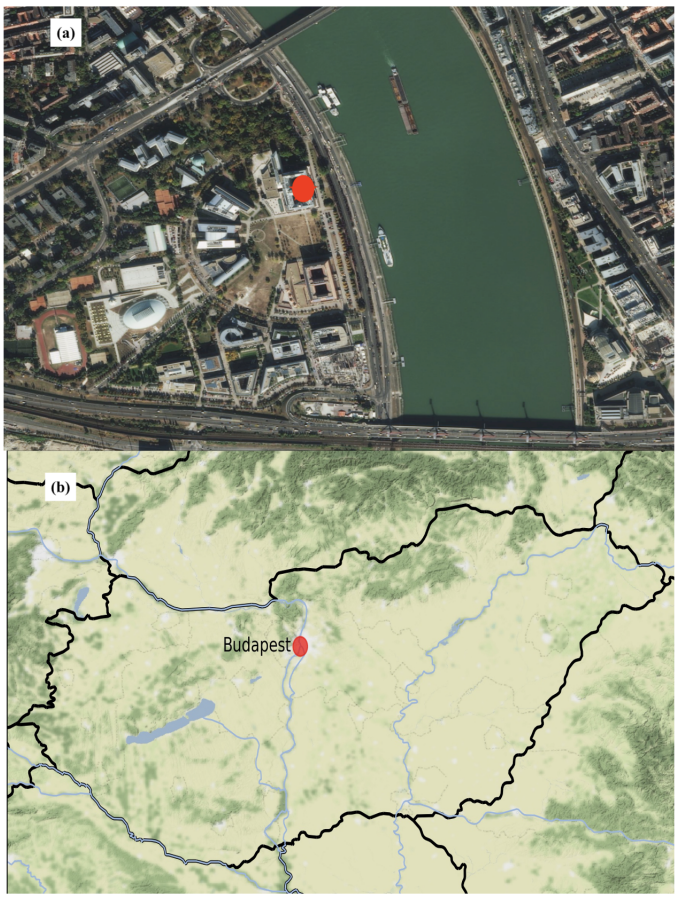

Figure 8: (a): Satellite image of observational site from google maps, (b): Terrain plot of Hungary.

The focus of this research (Enroth et al., 2018) was not on fog, so data about visibility is not available. However, both the temperature and the relative humidity of ambient air was measured at the observational site. It is supposed that fog is formed if the observed

relative humidity is equal to or larger than 99% for longer than 1 hr. Based on this RH observational data, 14 fog periods were defined in the observational period based on this data. The Hungarian Meteorological Service (hereafter HMS) also confirmed these fog events in the Budapest region. The radiation fog event from 31 January 2015 to 01 February 2015 was chosen for this study. The presence of this event and its duration were confirmed by low wind speed (< 1 ms^{-1}), street cameras (Figure 9), and it was also detected by HMS at the South–East region of Budapest. Figure 9 shows the fog evolution detected by the street camera at the BpART during morning time, and fog disappeared after 09:00 AM due to increase of solar radiation.

Figure 9: Evolution of fog detected by street cameras during the morning time at 01-Feb-2015.

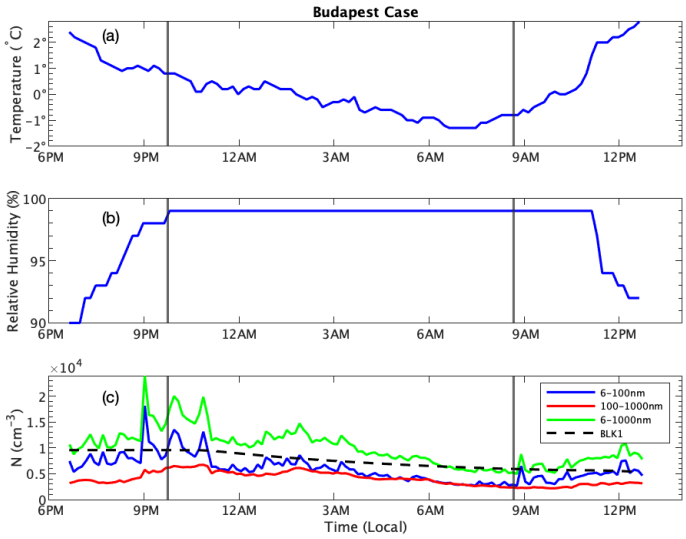

Figure 10: Observed temperature (a), Relative humidity (b), and number concentration of aerosol particles at different size ranges over Budapest (c). (Note: vertical lines indicate fog onset and offset. The dotted line denotes time evolution of simulated total aerosol concentration.) Details about the BLK1 case can be found in the text and in Table 1

Table 3: Initial conditions with different hygroscopicity parameter (κ) and different gas concentrations (kg/kg) for Budapest and Delhi cases along with sensitivity test ID. (Note: * means constant SO_2 source throughout the simulation.)

Case	Category	Test ID	SO_2 (kg/kg)	HNO_3 (kg/kg)	NH_3 (kg/kg)	H_2O_2 (kg/kg)	O_3 (kg/kg)
Budapest Case	Linear function ($\kappa_{LH} = 0.2$, $\kappa_{NH} = 0.03$)	BLK1	$*6.4 \times 10^{-9}$	4.2×10^{-11}	4.5×10^{-10}	1.1×10^{-10}	4.8×10^{-9}
		BLK2	$*6.4 \times 10^{-9}$	0	4.5×10^{-10}	1.1×10^{-10}	4.8×10^{-9}
		BLK3	6.4×10^{-9}	4.2×10^{-11}	4.5×10^{-10}	1.1×10^{-10}	4.8×10^{-9}
		BLK4	6.4×10^{-9}	0	4.5×10^{-10}	1.1×10^{-10}	4.8×10^{-9}
	Powe function ($\kappa_{LH} = 0.2$, $\kappa_{NH} = 0.03$)	BPK1	$*6.4 \times 10^{-9}$	4.2×10^{-11}	4.5×10^{-10}	1.1×10^{-10}	4.8×10^{-9}
		BPK2	$*6.4 \times 10^{-9}$	0	4.5×10^{-10}	1.1×10^{-10}	4.8×10^{-9}
		BPK3	6.4×10^{-9}	4.2×10^{-11}	4.5×10^{-10}	1.1×10^{-10}	4.8×10^{-9}
		BPK4	6.4×10^{-9}	0	4.5×10^{-10}	1.1×10^{-10}	4.8×10^{-9}
	homogenous hygroscopicity ($\kappa_{mean} = 0.145$)	BMK1	$*6.4 \times 10^{-9}$	4.2×10-11	4.5×10^{-10}	1.1×10^{-10}	4.8×10^{-9}
		BMK2	$*6.4 \times 10^{-9}$	0	4.5×10^{-10}	1.1×10^{-10}	4.8×10^{-9}
		BMK3	6.4×10^{-9}	4.2×10^{-11}	4.5×10^{-10}	1.1×10^{-10}	4.8×10^{-9}
		BMK4	6.4×10^{-9}	0	4.5×10^{-10}	1.1×10^{-10}	4.8×10^{-9}
Delhi case	$\kappa_{LH} = 0.42$, $\kappa_{NH} = 0.03$	DSK1	$*1.78 \times 10^{-8}$	2.2×10^{-10}	2×10^{-8}	1.1×10^{-9}	3.3×10^{-8}
		DSK2	$*1.78 \times 10^{-8}$	0	2×10^{-8}	1.1×10^{-9}	3.3×10^{-8}
		DSK3	1.78×10^{-8}	2.2×10^{-10}	2×10^{-8}	1.1×10^{-9}	3.3×10^{-8}
		DSK4	1.78×10^{-8}	0	2×10^{-8}	1.1×10^{-9}	3.3×10^{-8}
	homogenous hygroscopicity ($\kappa_{mean} = 0.3$)	DMK1	$*1.78 \times 10^{-8}$	2.2×10^{-10}	2×10^{-8}	1.1×10^{-9}	3.3×10^{-8}
		DMK2	$*1.78 \times 10^{-8}$	0	2×10^{-8}	1.1×10^{-9}	3.3×10^{-8}
		DMK3	1.78×10^{-8}	2.2×10^{-10}	2×10^{-8}	1.1×10^{-9}	3.3×10^{-8}
		DMK4	1.78×10^{-8}	0	2×10^{-8}	1.1×10^{-9}	3.3×10^{-8}

Figure 10 shows the observed temporal variability of the T, RH, and number concentration (N) of ultrafine (6-100 nm), chemically aged (100-1000 nm), and total particles (6-1000 nm) during the fog event in the time period of 31/01/2015 – 01/02/2015. Enroth et al. (2018) found that urban aerosol particles contained an external mixture of particles with a diverse chemical composition. The unique aspect of the Budapest data for the aerosol particles is that it involves information about the size dependence of the hygroscopicity (Enroth et al., 2018). The hygroscopic properties were derived by a Volatility-Hygroscopicity Tandem Differential Mobility Analyzer (VH-TDMA) measurement system. Less-hygroscopic (LH) and nearly hydrophobic (NH) particles are separated, based on the measurements of the hygroscopic growth factors (HGFs) at different dry diameters of 50, 70, 110, and 145 nm. The number fraction of nearly hydrophobic particles, based on this observation, is plotted in Figure 11. The linear or power function trend lines are used to give the ratio of the number concentration of the NH particles relative to concentration of the LH + NH particles at any sizes (Figure 11). Figure 12a and c depict the aerosol size distributions were used to give initial conditions for the numerical simulation. Figure 12a depicts the size distribution involving both the LH and NH particles. Figure 12c depicts the initial size distributions if linear and power function trend lines are fitted to make the distinction between LH and NH particles (Figure 11). To study the sensitivity of fog formation in terms

of the size dependence of the hygroscopicity, a mean hygroscopicity would characterize all the aerosol particles evaluated in the Budapest case:

$$\kappa_{mean} = \sum_{i=1}^{n} \frac{V_{1,i} N_{1,i} \kappa_{LH} + V_{2,i} N_{2,i} \kappa_{NH}}{V_{1,i} N_{1,i} + V_{2,i} N_{2,i}} \tag{31}$$

where n is the number of bins, $V_{1,i}, V_{2,i}$ are volumes of LH and NH particles in the i^{th} bin, respectively, $N_{1,i}, N_{2,i}$ are the number concentrations of the LH and NH categories at the i^{th} bin. κ_{LH} and κ_{NH} are measured hygroscopicity parameters of less-hygroscopic and nearly-hydrophobic particles (κ=0.2 and 0.03), respectively.

In order to better understand the changes in the characteristics of aerosol particles in

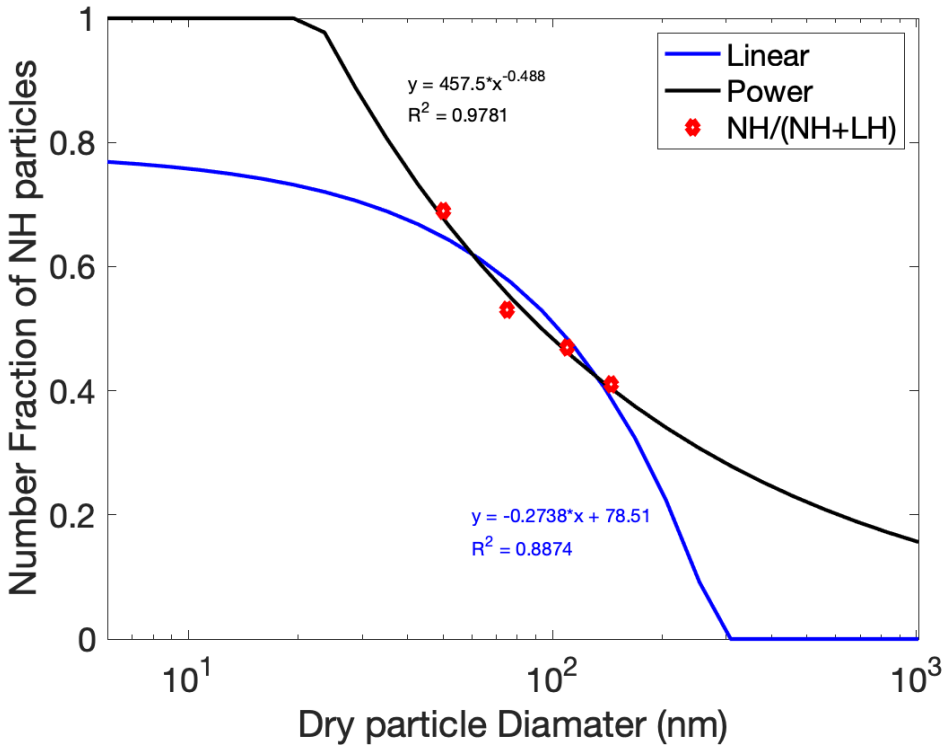

Figure 11: Fitted linear and power functions to give the fraction of NH particles for the whole spectrum. The red dotes denote the observed fractions. Note: LH and NH denotes less hygroscopic and nearly hydrophobic dry aerosol particles

the fog, we simulate the impact of trace gases. Concentrations of SO_2, NH_3, HNO_3, O_3 provided by HMS are used to give the trace gas concentration for the Budapest case. The daily average trace gas concentrations are available for NH_3, and HNO_3 so we consider these as initial values. Furthermore, the concentration of these trace gases in the atmosphere is not allowed to reduce under one-tenth of the initial concentration (Table 3). This means that we suppose the trace gases are partly supplied by advection or local sources. In the case of SO_2 and O_3, the hourly measured data show that their concentrations were

nearly constant during the fog event. In this case, we make a sensitivity test to study how the concentration impacts the chemical processes occurring in the fog droplets: (i) the SO_2 concentration is held constant as it was observed, (ii) the SO_2 concentration is allowed to reduce, but not below one-tenth of the initial concentration due to the absorption.

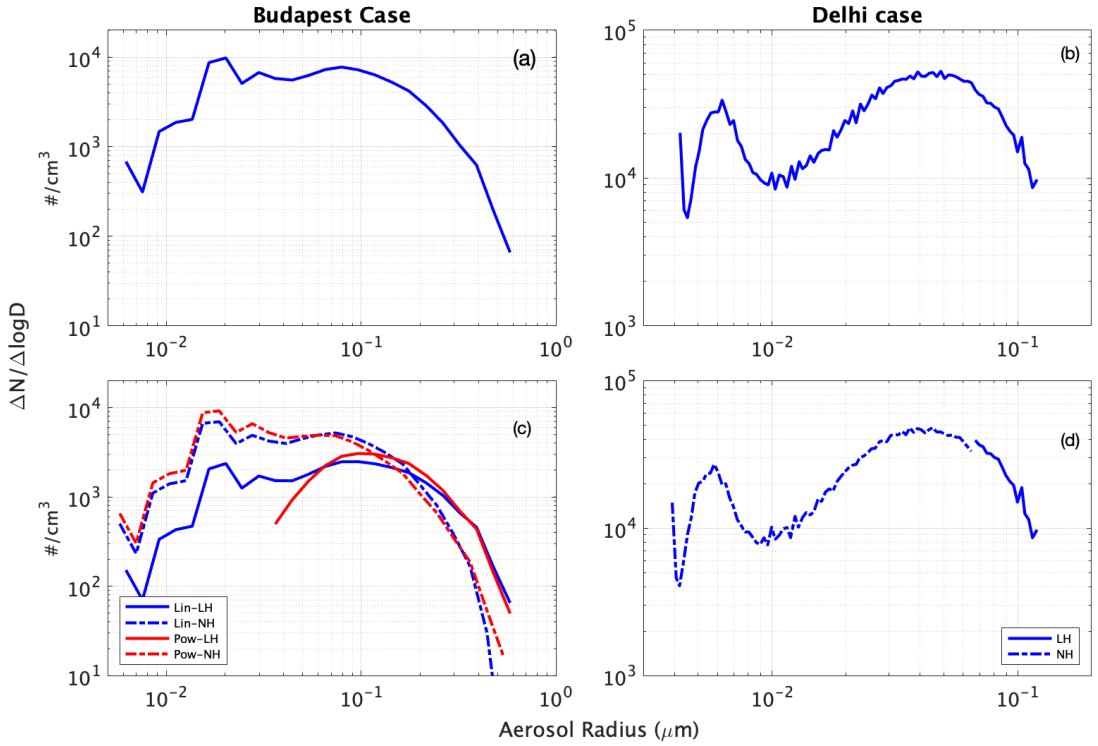

Figure 12: Initial size distribution of particles of observed and model input over Budapest and Delhi fog events. Observed dry aerosol size distributions are plotted in panels (a) and (b). Panel (c) and (d) reveal the distinction of aerosol particles into the categories of less hygroscopic (LH) and near hydrophobic (NH) over BLK1 and DSK1 cases. Size distributions plotted in panels (a) and (b) are used if the size dependence of the κ value is neglected. The legend in panel c denotes the way of the separation of LH and NH particles.

5.1.2 Observational data over Delhi

The observational site was located at Indira Gandhi International Airport (IGIA, 28.56°N, 77.09° E), Delhi, India. This is one of the biggest airports in the world and it is about 240 m above mean sea level. In the current research, we use the data observed in intensive observational periods during winter fog experiments (WIFEX; Ghude et al. (2017)). Fog formed on 30 December 2016, 23:30 LT (18:00 UTC) and disappeared on 31 December 2016, 07:30 LT (02:00 UTC) was chosen to simulate the fog formation in this study.

Sensitivity tests are made with different κ values and trace gas concentrations. Figure 12b, 12d shows initial size distributions of aerosol particles over Delhi. During this experimental campaign, a micro meteorological tower with a height of 20 m was set up at the site,

Figure 13: Observational site of India. Satellite image from google maps (a), terrain plot of Indo-Gangetic plain, India (b)

which measured the boundary layer characteristics such as T and RH at three different levels (Figure 14). For our model simulation, data observed at 10 m height was considered. A scanning mobility particle sizer (SMPS) was used to measure the concentration and the size distribution of dry aerosol particles in a diameter range of 10 – 300 nm (Figure 14c, Figure 12b). Bulk hygroscopicity parameters were measured in Delhi during the Delhi Aerosol Supersite (DAS) campaign, there is no available information about the size dependence of the κ value in this case. The average hygroscopicity parameter is evaluated from the observed data by using the mixing rule (Petters and Kreidenweis, 2007), which resulted in approximately 0.3 (Arub et al., 2020) . Pringle et al. (2010) simulated the global continental (land mass) mean κ value and obtained 0.27±0.21, which is in line with our estimated and adopted κ value. The sensitivity on the size dependence of hygroscopicity is studied by separate simulations:

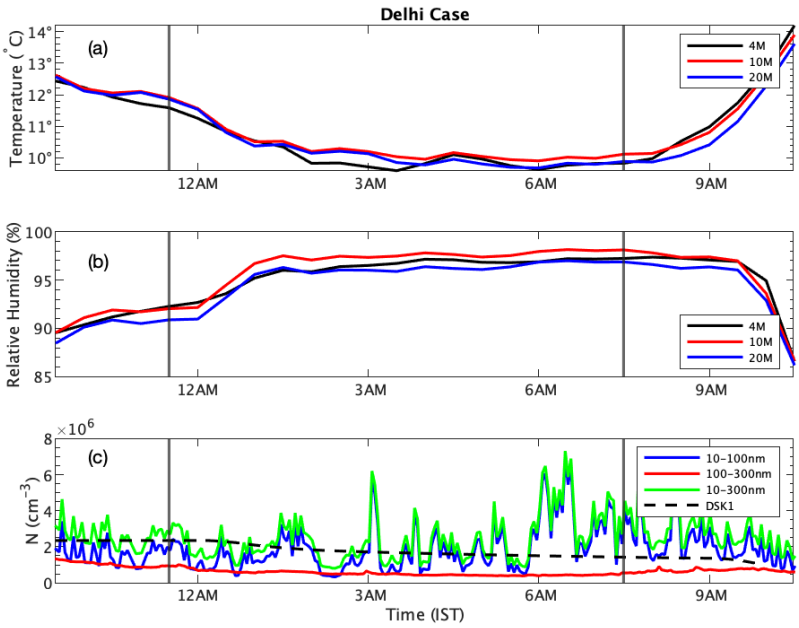

Figure 14: Observed temperature (a), Relative humidity (b), and number concentration of aerosol particles at different size ranges over Delhi (c). (Note: vertical lines indicate fog onset and offset. The dotted line denotes time evolution of simulated total aerosol concentration.) Details about the DSK1 case can be found in the text and in Table 1.

- The hygroscopicity of all aerosol particles is the same as the value available from the field project (Figure 12b).

- The aerosol particles for the Delhi case are hypothetically divided into two categories. All the particles less than 200 nm in diameter are supposed to be NH particles and their κ value is supposed to be equal to 0.03. On the base observation in China, Wang et al. (2018) asserted that dry aerosol particles with a diameter of 200 nm had significantly larger hygroscopic growth factors compared to the particles with a diameter of 50 nm.

  Using these assumptions and substituting the average κ value (0.3) into the left-hand side of eq. 31 the value of the κ value for the LH particles can be evaluated. In this case, the evaluated κ value of LH particles larger than 200 nm is 0.42 (Figure 12d).

Trace gas concentrations of SO_2, NH_3, HNO_3 were measured in this project. Unfortunately, data are not available for the selected day. So data published by Acharja et al. (2020) for the same location but different fog events are given as initial conditions, due to the lack of available trace gas concentration data on 30 December 2016. The temporal evolution of the gas concentration is treated the same way as in the Budapest case. The initial conditions for the numerical simulation are the size distributions of the aerosol

particles before the onset of fog over Budapest and Delhi plotted in Figure 12a, as well as in Figure 12b, respectively. Initial aerosol size distributions are shown in Figure 12c and 12d represent the cases when the aerosol particles are divided into categories of LH and NH. For a better understanding of fog chemistry, we performed several sensitivity tests with different hygroscopicity, and different environmental conditions (trace gas concentrations) summarized in Table 3 along with test ID.

6 1D model results

6.1 Time profiles of the fog evolution

Figure 15 shows the time profiles of simulated and observed fog events. Also, the fog onset, mature period and dissipation for both the Budapest and Delhi cases are indicated. In the Budapest case, the fog onset and dissipation were based on the observed RH ≥99% and street camera visibility. Our model shows a 1-hour delay of fog onset in the Delhi case, but in the Budapest case fog onset is simulated well. Figure 15 shows that fog phases distinguished (vertical dotted lines) based on model results, have 2 - 3 hrs delay comparing to the observed fog life cycle (vertical solid lines).

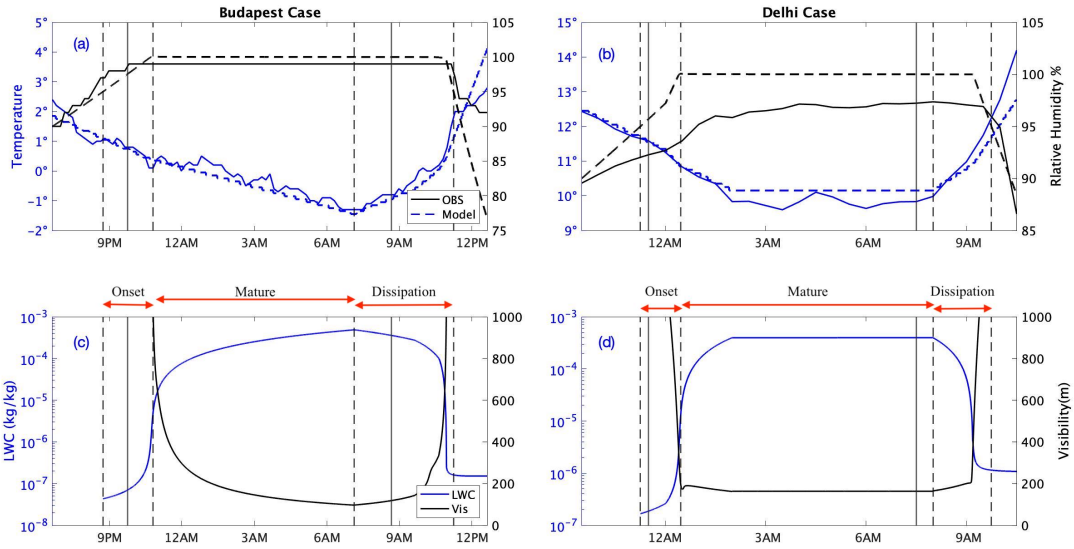

Figure 15: Evolution fog over Budapest (at 31 January 2015–1 February 2015) and Delhi (30–31 December 2016). Panel (a) and (b): Observed and calculated temperature and RH for Budapest and Delhi cases. Panel (c) and (d): Simulated LWC and visibility for both Budapest and Delhi cases. The vertical dashed lines indicate the model defined evolution periods of the fog, and solid lines show the observed fog onset and offset time.

These discrepancies can be the consequence of the fact that in our 1D model only the impact of the cooling/warming is taken into consideration, and the effect of any other processes (e.g., turbulent mixing, sedimentation, radiative cooling at the top of the fog) are neglected. Figure 15a, and 15b show the observed and simulated time profiles of temperature and relative humidity of the Budapest and Delhi cases. The fitting of the temperature profiles in both cases shows how well the observed temperature profile is reproduced by prescribed cooling and warming rates (Note: the temperature is affected by both the radiative cooling rate and the releasing latent heat of condensation). The

Table 4: Summary of maximum supersaturation (s_{max}), critical radius of droplet (r_{crit}) for the hygroscopic particles, total activated aerosols at s_{max}, maximum LWC, initial number concentration of the aerosol particles (N), scavenging and relative effect of Brownian and phoretic scavenging and total amount of scavenged particles during the period when RH>95%, change of maximum aerosol size ($\triangle r_p$) by the end of the dissipation period.

Test ID	s_{max}	r_{crit} (μm)	Activated aerosol ($\#/cm^3$)	LWC_{max} (gm^{-3})	N ($\#/kg$)	N_{Br} ($\#/kg$)	N_{Br}/N	N_{ph} ($\#/kg$)	N_{ph}/N	Total scavenged %	$\triangle r_{aer}$ (μm)
BLK1	4.61×10^{-4}	1.74	16	0.487	8.5×10^{9}	3.29×10^{9}	38.84%	8.63×10^{7}	1.02%	39.86%	0.45
BLK2	4.61×10^{-4}	1.74	16	0.487	8.5×10^{9}	3.29×10^{9}	38.84%	8.61×10^{7}	1.02%	39.86%	0.39
BLK3	4.61×10^{-4}	1.74	16	0.487	8.5×10^{9}	3.29×10^{9}	38.84%	8.55×10^{7}	1.01%	39.85%	0.28
BLK4	4.61×10^{-4}	1.74	16	0.487	8.5×10^{9}	3.29×10^{9}	38.84%	8.52×10^{7}	1.01%	39.85%	0.19
BPK1	4.75×10^{-4}	1.69	16	0.487	8.5×10^{9}	3.34×10^{9}	39.50%	6.69×10^{7}	0.79%	40.29%	0.45
BPK2	4.75×10^{-4}	1.69	16	0.487	8.5×10^{9}	3.34×10^{9}	39.50%	6.68×10^{7}	0.79%	40.29%	0.4
BPK3	4.75×10^{-4}	1.69	16	0.487	8.5×10^{9}	3.34×10^{9}	39.50%	6.63×10^{7}	0.78%	40.29%	0.28
BPK4	4.75×10^{-4}	1.69	16	0.487	8.5×10^{9}	3.34×10^{9}	39.51%	6.61×10^{7}	0.78%	40.29%	0.19
BMK1	5.09×10^{-4}	1.58	19	0.487	8.5×10^{9}	3.12×10^{9}	36.90%	7.48×10^{7}	0.88%	37.79%	0.44
BMK2	5.09×10^{-4}	1.58	19	0.487	8.5×10^{9}	3.12×10^{9}	36.90%	7.46×10^{7}	0.88%	37.79%	0.39
BMK3	5.09×10^{-4}	1.58	19	0.487	8.5×10^{9}	3.12×10^{9}	36.90%	7.40×10^{7}	0.88%	37.78%	0.28
BMK4	5.09×10^{-4}	1.58	19	0.487	8.5×10^{9}	3.12×10^{9}	36.91%	7.37×10^{7}	0.87%	37.78%	0.18
DSK1	6.42×10^{-4}	1.18	161	0.397	4.12×10^{10}	1.56×10^{10}	37.86%	5.41×10^{9}	13.15%	51.01%	0.57
DSK2	6.42×10^{-4}	1.18	161	0.397	4.12×10^{10}	1.56×10^{10}	37.86%	5.29×10^{9}	12.85%	50.72%	0.5
DSK3	6.35×10^{-4}	1.18	161	0.397	4.12×10^{10}	1.56×10^{10}	37.86%	5.07×10^{9}	12.32%	50.17%	0.39
DSK4	6.35×10^{-4}	1.18	161	0.397	4.12×10^{10}	1.56×10^{10}	37.85%	4.72×10^{9}	11.46%	49.31%	0.26
DMK1	7.57×10^{-4}	1.00	161	0.397	4.12×10^{10}	9.32×10^{9}	22.64%	4.25×10^{9}	10.32%	32.96%	0.57
DMK2	7.57×10^{-4}	1.00	161	0.397	4.12×10^{10}	9.32×10^{9}	22.64%	4.14×10^{9}	10.06%	32.70%	0.5
DMK3	7.57×10^{-4}	1.00	161	0.397	4.12×10^{10}	9.32×10^{9}	22.63%	3.91×10^{9}	9.51%	32.14%	0.39
DMK4	7.57×10^{-4}	1.00	161	0.397	4.12×10^{10}	9.32×10^{9}	22.63%	3.61×10^{9}	8.76%	31.39%	0.26

difference between the simulated and observed time profiles of the relative humidity is more significant, mostly in the Delhi case. However, this discrepancy can be explained by measurement error. Generally, the RH sensors measure up to 95%, and they usually do not reach 100% (Gultepe, 2007, 2019).

Based on the time evolution of liquid water content, we define three phases in the life cycle of the fog (Figure 15c, 15d). The period when the LWC increases significantly before the supersaturation reaches its maximum value is called the onset period of the fog. (LWC hereafter means the sum of the liquid water mixing ratios calculated in each bin, and as such in our model output the LWC includes the haze particles as well, however the mixing ratio of the haze particles is about one-two order smaller than that of the fog droplets.) The next period remains until the supersaturation drops below 0, this period is called the mature fog phase. The last phase is when the drops start to evaporate, which is called dissipation period. These periods are indicated by vertical dashed lines in Figure 15. At the time when visibility drops below 200 m, the value of LWC is 0.13 g/kg (near 0.13 g m^{-3}) and 0.08 g/kg (near 0.08 g m^{-3}) in the Budapest and Delhi case, respectively. The larger concentration of haze particles and water drops in the Delhi case explains why

the dense fog can form in Delhi even at a smaller LWC. Unfortunately, no observed LWC data is available to verify our calculated data. The formula suggested by (Gultepe et al., 2006b) can be used to estimate LWC if the visibility and concentration of the fog drops are known. Since the reported visibility is between 50 and 100 m (Pithani et al., 2020), and the number concentration of the fog drops is about 250 cm^{-3} (see the concentration of the activated aerosol particles in Table 4), the LWC should be between 0.41 and 0.14 g m^{-3}. During the WIFEX campaign, the evolution of the fog events in Delhi was simulated by WRF mesoscale model (Pithani et al., 2020), and presented the LWC about 0.2 g m^{-3} at the middle phase of the fog development. However, in our current simulation the maximum value of LWC is about 0.4 g m^{-3} in the mature phase of the fog for the same case. The discrepancy between these two values can be explained by different model configurations (e.g., the turbulent mixing and sedimentation is not considered in our model simulation). The dissipation rate of the fog depends mostly on the warming rate. The LWC starts to decrease when the saturation drops below 100% at about 7:00 am in the Budapest case and at about 8 am in the Delhi case. The LWC decreases only slightly between 7 am and 11 am in Budapest, because of the small warming rate (about 0.3 $^{\circ}Ch^{-1}$) in this time period. Later, the warming rate becomes significantly larger (about 1.5 $^{\circ}Ch^{-1}$), and the fog dissipates very fast, within 30 min. In the Delhi case, the average warming rate is about 1 $^{\circ}Ch^{-1}$ which results in different dissipation pattern comparing to the Budapest case. As a consequence of the different warming rates, it takes more than 90 min. and less than 60 min. to drop the relative humidity from near 100% to 90% in the Delhi and Budapest cases, respectively.

6.2 The impact of the scavenging

Scavenging of small aerosol particles by water drops is a self-cleaning mechanism in the atmosphere. Due to the very small supersaturation (of 0.0004 and 0.0007 in the Budapest and Delhi cases respectively, shown as s_{max} in the second column of Table 4), the activation reduces the number concentration of even the hygroscopic particles in fog only slightly. Figure 16 summarizes the results of the numerical simulation about the efficiency of the different scavenging mechanisms.

Figure 16a and 16b show the temporal evolution of the accumulated numbers of scavenged particles in the BLK1 and BMK1, as well as in the DSK1 and DMK1 cases (these cases provide a good representation well of all the simulated cases if only scavenging is

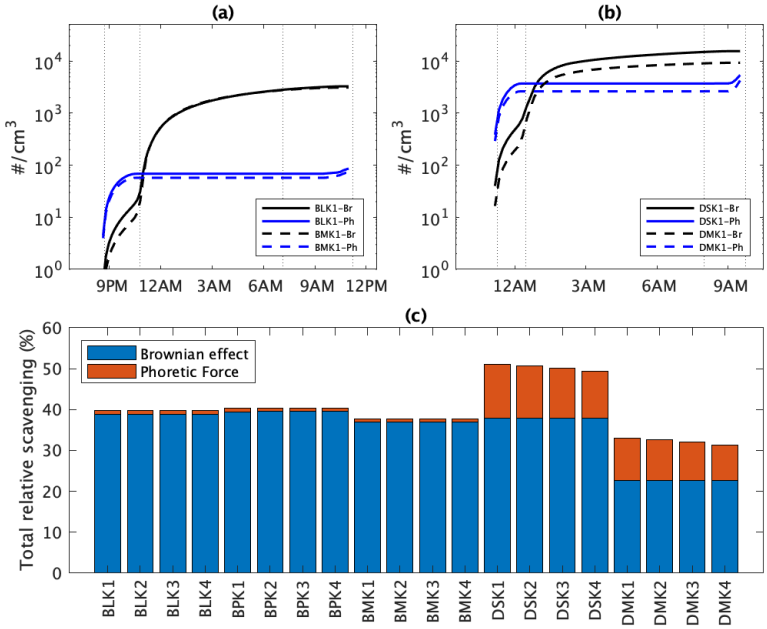

Figure 16: Cumulative effect of Brownian and phoretic forces on scavenging process in (a): Budapest case and (b): Delhi case. (c): Efficiency of Brownian motion and that of phoretic forces in total scavenging rate. The total relative scavenging means the ratio of the scavenged particle concentration and the total initial aerosol concentration

considered). Figure 16c reveals that the liquid chemical processes have no impact on the scavenging processes in either the Budapest or the Delhi cases (see case ID's in Table 3). In both cases, the temporal variation of the scavenging rates is related to temporal variation of the LWC. While the impact of the Brownian motion is dominant in all of the investigated cases, the role of the phoretic scavenging mechanism is negligible in the Budapest cases and is more significant in the Delhi cases (Figure 16c and Table 4). In the Budapest cases, the results do not depend on the function (linear or power) used to give the fraction of the number concentration of the near-hydrophobic particles, or the average hygroscopicity supposed for all the particles (Figure 16c). However, both in the Budapest case (although to a lesser extent) and in the Delhi case (to a larger extent), the efficiency of Brownian scavenging decreases significantly if the hygroscopicity is supposed to be same for all the particles (Figure 16 and Table 4). These results stem from the fact that if the aerosol particles are identical (BMK1-BMK4 as well as DMK1-DMK4) with respect to hygroscopicity, the width of the wet aerosol/drop spectrum remains smaller during the evolution of the size distribution compared to the other cases (BLK1-BPK4, furthermore DSK1-DSK4). While in the first group of cases the drops can form and grow on both the small aerosols particles (haze) and on the larger ones as well, in the second group of the cases the drops formed on the larger and more water-soluble aerosol particles grow

by diffusional growth, and a large fraction of the smaller particles becomes only slightly wet. At 10:30 pm, when the difference between the accumulated Brownian scavenging rates is the largest between the BLK1 and BMK1 cases, the number concentrations of particles smaller than 0.1 μm are 8.48×10^4 and 7.57×10^4 cm^{-3}, respectively. Furthermore, these numbers in the case of DSK1 and DMK1 at 12:00 am are $1.94 \times 10^6$and 1.47×10^6, respectively. The larger reduction (ca. 25%) of particle concentration in the Delhi case proves that the efficiency of Brownian scavenging is higher if the small aerosol particles ($< 0.1 \mu$m) are mostly NH particles (see the initial size distribution of the aerosol particles in Figure 12). If the aerosol particles are internally mixed, the efficiency of the Brownian scavenging becomes significantly smaller.

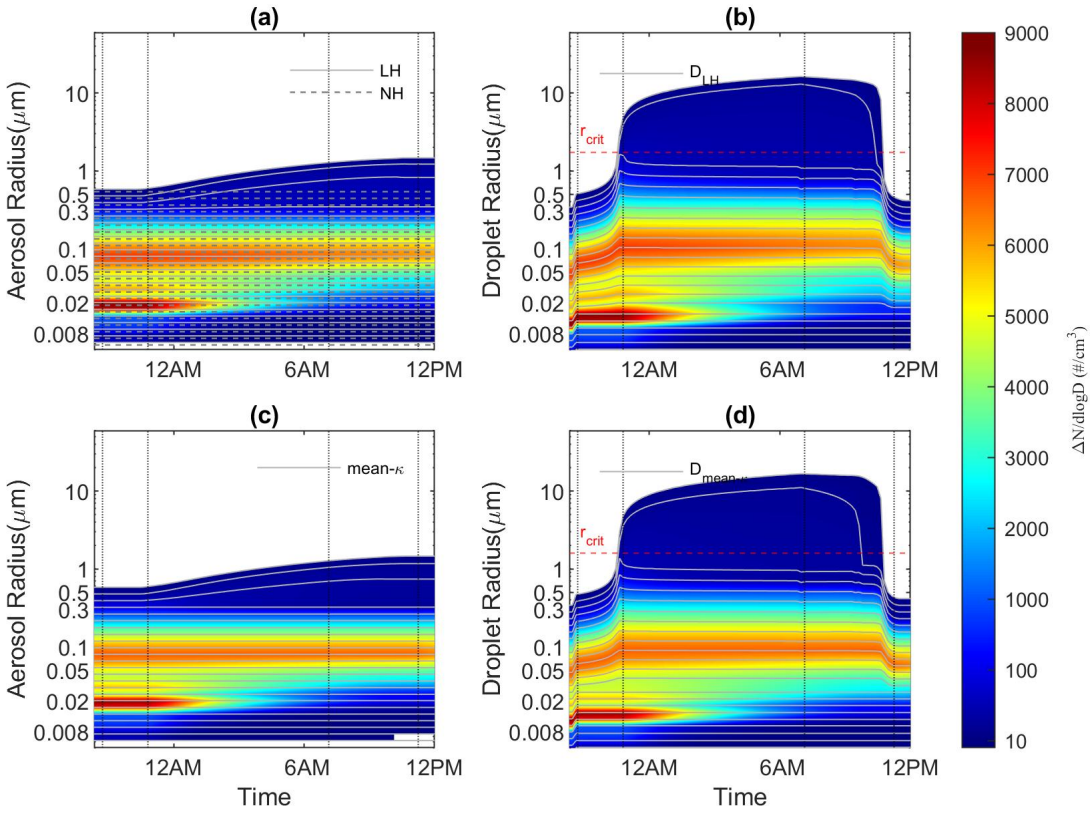

Figure 17: Contour plots depict the time evolution of aerosol and haze/droplet size distribution for Budapest cases (BLK1 at first row and BMK1 second row). The vertical dotted lines denote the different phases of the fog (see the vertical dashed lines in Figure 14). r_{crit} means the critical radius for water drops at the supersaturation which occurs during the mature phase of the fog, LH and NH mean less hygroscopic and nearly hydrophobic dry aerosol particles, respectively. mean-κ means that all dry aerosol particles have the same hygroscopicity, D_{LH} denotes drops formed on LH particles. $D_{mean-\kappa}$ denotes drops formed on aerosol particles having the same hygroscopicity. The time evolution of the bin boundaries for the aerosol particles and liquid drops are depicted as it is given by the figure legend.

Figure 16a reveals that in the Budapest case, the number concentration of captured aerosol particles increases from 8:30 pm to midnight due to the formation and growth of liquid drops. In the dissipation phase of the fog, the number concentration of captured particles by phoretic forces increases only slightly (Figure 16a). In the Delhi case the impact of phoretic scavenging is more significant. This process is efficient at the end of the offset period of the fog (Figure 16b).

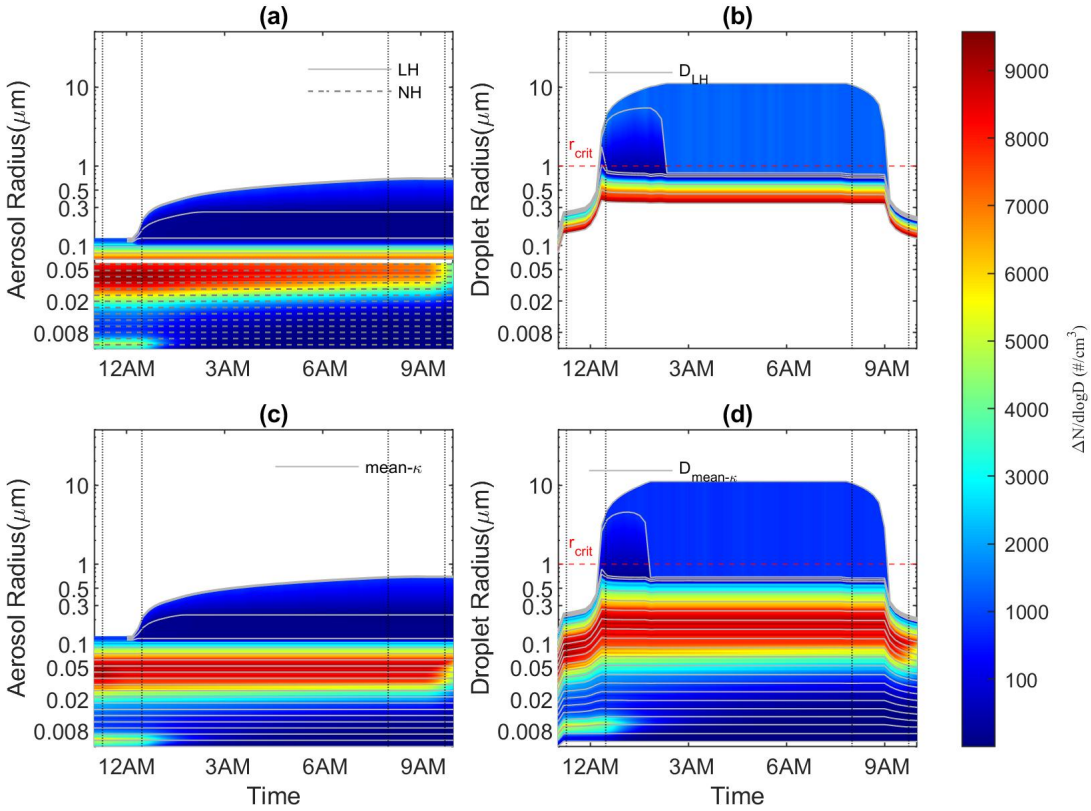

Figure 18: Contour plots depict the time evolution of aerosol and haze/droplet size distribution for Delhi cases (DSK1 at first row and DMK1 second row). The vertical dotted lines denote the different phases of the fog (see the vertical dashed lines in Figure 14). r_{crit} ***means the critical radius for water drops at the supersaturation which occurs during the mature phase of the fog, LH and NH mean less hygroscopic and nearly hydrophobic dry aerosol particles, respectively. mean-κ means that all dry aerosol particles have the same hygroscopicity,*** D_{LH} ***denotes drops formed on LH particles.*** $D_{mean-\kappa}$ ***denotes drops formed on aerosol particles having the same hygroscopicity. The time evolution of the bin boundaries for the aerosol particles and liquid drops are depicted as it is given by the figure legend.***

The contour plots in Figure 17 and Figure 18 show the time evolution of size distribution of dry aerosol/aerosol inside the droplets over the Budapest and Delhi cases, as well as the size distribution of droplets for the BLK1, BMK1, DSK1 and DMK1 cases. In Figure 17a and Figure 18a the solid and dashed lines denote boundaries for the LH and the NH bins, respectively. In Figure 17b and Figure 18b the time evolution of the size distribution (DSD)

of droplets formed on LH particles is plotted. The solid lines denote the bin boundaries for the liquid drops, both haze and fog drops, in Figure 17b and Figure 17d as well in in Figure 17b and Figure 17d. The evolution of aerosol size distribution is the consequence of two different processes. The size distribution of NH particles is impacted only by the scavenging processes. The size distribution of the LH particles is also impacted by the scavenging processes, additionally, the broadening of the final bins is the consequence of chemical reactions occurring inside of the water drops. During the onset period of the fog, the significant decrease of aerosol concentration at the radius smaller than 0.05 μm is the consequence of Brownian scavenging (e.g., Santachiara et al. (2012)) both in the Budapest and Delhi case (panels a and c in Figure 17 and Figure 18). Because of its smaller effect, the impact of phoretic forces cannot be recognized in panels related to the Budapest cases. The efficiency of phoretic scavenging is more obvious in the Delhi case. Figure 18a and 18c reveal a significant decrease of the concentration of aerosol particles with a radius around 0.05 μm at the end of the offset period. This difference can be explained by the following two reasons:

- The concentration of aerosol particles at the size of about 0.1 μm is significantly larger in the Delhi case, than in the Budapest case (Figure 12). At this aerosol size, phoretic scavenging is more dominant than Brownian scavenging, because the Brownian effect is small if the aerosol size is near or larger than 0.1 μm (Santachiara et al., 2012, 2013).

- During the onset and dissipation periods, aerosol particles with a radius around 0.1 μm can only be captured by water drops due to phoretic forces in a subsaturated environment. The smaller warming rate and the larger hygroscopicity of water-soluble aerosol particles resulted in longer dissipation and subsaturated periods in the Delhi case (Figure 15).

The contour plots about the drop size distribution both in Figure 17 and Figure 18 reveal that the number concentration of droplets larger than the critical radius is small in both Budapest and Delhi case (see also the number concentration of the activated aerosol particles in Table 4). In the mature phase of the fog, drops larger than the critical size keep growing, and they collect the sub-micron particles of the LH and NH modes through Brownian motion. Note, the critical radius is evaluated by using a near constant supersaturation in the mature phase, and not the maximum supersaturation at the end of the onset period. Drops smaller than the critical size evaporate slightly even during the mature

phase of the fog (see the time profiles of the bin boundaries for the drops/haze particles). By the end of the dissipation phase of the fog, the drops completely evaporate, and only wet aerosol particles remain. Comparison of the size distribution of aerosol particles in the onset and the dissipation period reveals the impact of the scavenging process (see the decrease of the concentration of aerosol particles smaller than 0.1 μm) and the sulphate formation occurring inside of the drops (see the broadening of the aerosol size distribution for particles larger than 0.3 μm in Budapest case and larger than 0.2 μm in Delhi case).

6.3 The impact of liquid chemistry

The initial composition of a droplet is determined by the dissolution of soluble materials contained within an aerosol particle, which serves as the cloud condensation nucleus (CCN). Further variations in the composition come from subsequent scavenging of other non-activated, interstitial particles and from uptake of water-soluble gases and aqueous-phase reactions. We study how the hygroscopicity of the aerosol particles and the concentration of different inorganic trace gases (Table 3) affect the evolution of the chemical characteristics of fog and the aerosol regeneration process. Due to the long lifetime of the fog and the slow sedimentation of the drops, they absorb large amounts of different types of trace gases. All gases are depleted rapidly by drops in line with increases of the LWC (Figure 19). The amounts of the absorbed gases increase less during the mature phase of the fog, and no further increase occurs during the dissipation period, if LWC decreases significantly. Figure 19e and Figure 19f shows that the absorption of HNO_3 is affected only by its concentration in the atmosphere. Because the Henry constant of this gas is large, the amount of the absorbed HNO_3 depends neither on the absorption of other gases, nor on the pH of the drops. The absorption of the SO_2 gas is also mostly impacted by the concentration of this gas. However, in the Delhi case, where the concentration of the HNO_3 gas is about 50 times larger than in the Budapest case, the presence of the HNO_3 gas in the atmosphere mitigates the absorption of the SO_2 gas only slightly (see also in Figure 20). As a result of more pollution (the larger concentration of trace gases and aerosol particles) in the Delhi case, the time profiles describing the absorption of SO_2 and NH_3 diverge during the onset period of the fog. In the Budapest case, due to the less polluted atmosphere, this divergence started a few hours after the onset of the fog. Figure 19g and 19h shows the time profile of the bulk pH. (The bulk pH plotted in these Figure 19g and Figure 19h is calculated by summarizing liquid water content and the different

compounds in them over the size spectrum.) Comparison of panels c and g, along with panels d and h in Figure 19 reveals that the absorption of NH_3 is regulated by pH. The pH of the water drops is affected not only by the absorption of the gases previously mentioned, but also the formation of $S(VI)$.

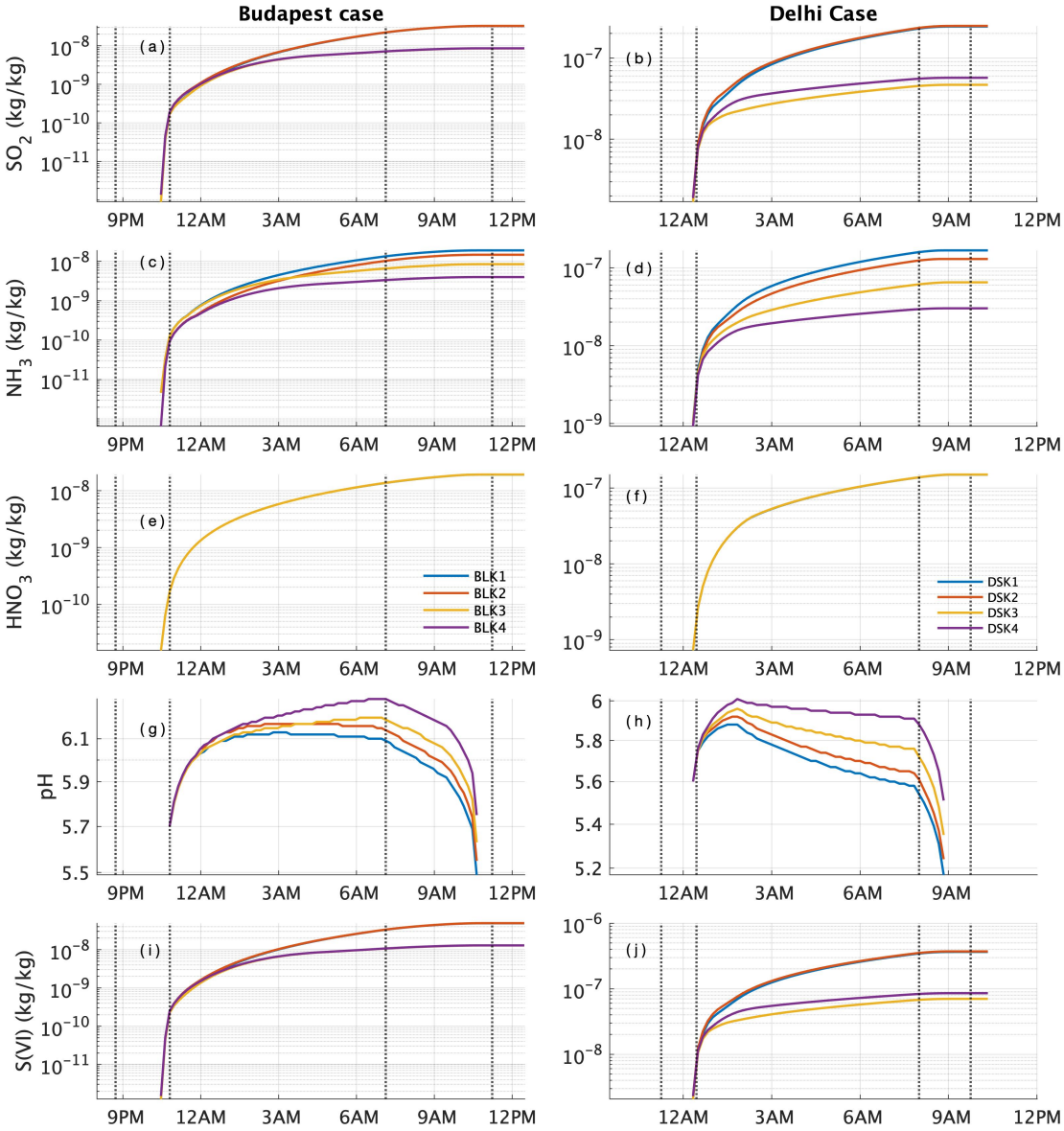

Figure 19: Time evolution of the accumulated absorption of trace gases (panels (a) – (f)), bulk pH (panels (g) and (h)) and accumulated S(VI) (panels (i) and (j)). The different lines with different colors denote different cases (see the legends in panels (e) and (f)).

The pH of the drops remains in the interval from 5 to 6.5. This enhances the absorption of NH_3 without the drops becoming saturated with respect to the NH_4^+ ions (Schmeller and Geresdi, 2019). As we can see in Figure 19i and 19j, the time evolution of accumulated

$S(VI)$ significantly depends on the amount of SO_2 absorption for both the Budapest and the Delhi cases. In the Delhi case, the uptake of HNO_3 results in the decrease of $S(VI)$ formation by increasing the acidity significantly in fog droplets. Fog becomes the most acidic in the BLK1 and DSK1 cases (HNO_3 is present in the atmosphere and a large amount of SO_2 is absorbed). The lower pH promotes the absorption of NH_3, which results in the enhancement of NH_4^+ ion accumulation (Figure 20). In the BLK4 and DSK4 cases (a lesser amount of SO_2 is absorbed and the concentration of HNO_3 is set equal to zero) the fog becomes less acidic. The simulated time evolution of pH in the Budapest cases is plotted in Figure 19g. During the onset period the fog is more acidic (pH=5.6–5.7) and pH gradually increases with respect to time due to increase of LWC. During the mature period, the pH of the solute concentration remains near constant because the absorption of trace gases and the sulfate formation is balanced by the increase in the drop size. In the dissipation period pH decreases along with LWC mostly due to the evaporation of the droplets. In the more polluted environmental (Delhi case) conditions pH reaches nearly 6 at by the end of the onset period, and in the mature period the fog becomes gradually more acidic (Figure 19h). Because in the Delhi case the LWC remains near constant during the mature phase, the absorption of gases and the sulfate formation results in a decrease of the pH. This decrease becomes more evident in the dissipation phase of the fog. The pH curves are more divergent due to the larger impact of changes in the concentration of gases in Delhi from case to case.

Figure 20 summarizes the results of all chemistry sensitivity tests for the mass concentration of $S(VI), NH_4^+, NO_3^-$ formed and accumulated inside of the droplets by the end of fog dissipation phase. The pattern of the histograms reveals that size dependence of the hygroscopicity has no effect on the liquid chemistry occurring in the drops. Our model results also show that $S(VI)$ has significant role, and it modulates the fog acidity over both Budapest and Delhi (Figure 19i and Figure 19j). Figure 20 shows that large amounts of $S(VI)$ correspond highly to the amount of total SO_2(g) absorption. As expected, the mass concentration of NH_4^+ depends on the absorption of SO_2(g) and on the absence/presence of HNO_3(g). The amount of the mass concentration of $S(VI)$ is also affected (slightly reduction) by the presence of HNO_3(g). The final column in Table 4 gives the broadening of the size distribution of aerosol particles due to the liquid chemistry. In Figure 17a, Figure 17c and Figure 18a, Figure 18c the time profiles of solid grey lines depicting the evolution of the size distribution of aerosol particles reveal the broadening of the distribution due to the liquid chemistry. The mass of aerosol particles is increased by the accumulated ions of

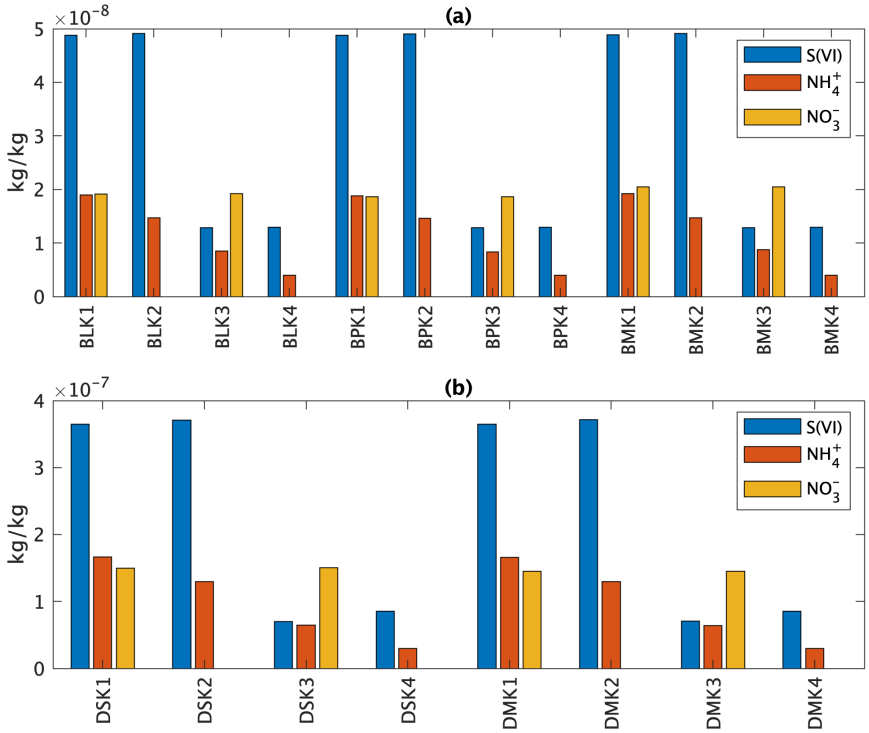

Figure 20: Mass concentration of $S(VI), NH_4^+, NO_3^-$ ***for the sum of the regenerated aerosol particles by the end of the dissipation phase for Budapest (a) and Delhi (b).***

$NH_4^+, NO_3^-, S(VI)$. The addition of these species not only increases the mass of the aerosol particles, but they change the hygroscopicity of the particles as well. The impact of the collected hydrophobic particles is negligible because their mass is about one – two orders of magnitude less than the mass of the sulfate formed inside of the drops. Figure 21 shows the calculated new hygroscopicity parameter for each bin for the regenerated aerosol particles at the end of the dissipation phase for all sensitivity tests. The new hygroscopicity parameter is calculated by the volume weighted averages (Petters and Kreidenweis, 2007):

$$\kappa_i = \frac{V_{i,o}\kappa_{LH} + V_{i,s}\kappa_s}{V_{i,o} + V_{i,s}} \tag{32}$$

where $V_{i,o}$ and $V_{i,s}$ are the volumes of the less hygroscopic particles and those of the sulphate forms in the i^{th} bin, respectively. κ_{LH} and κ_s are the hygroscopicity parameters for the less-hygroscopicity particles, and for the sulphate compounds. We suppose that the hygroscopicity of the mix of NH_4^+, NO_3^- and $S(VI)$ ions is 0.6 (Note: liquid chemistry was simulated for the drops with radius of equal or larger than 1 μm).

The hygroscopicity related to the smallest sizes was not impacted by the chemistry (see the size limit for the liquid chemistry above), so these values are equal to the initial ones. The sensitivity test reveals that initial conditions for the size dependence of the

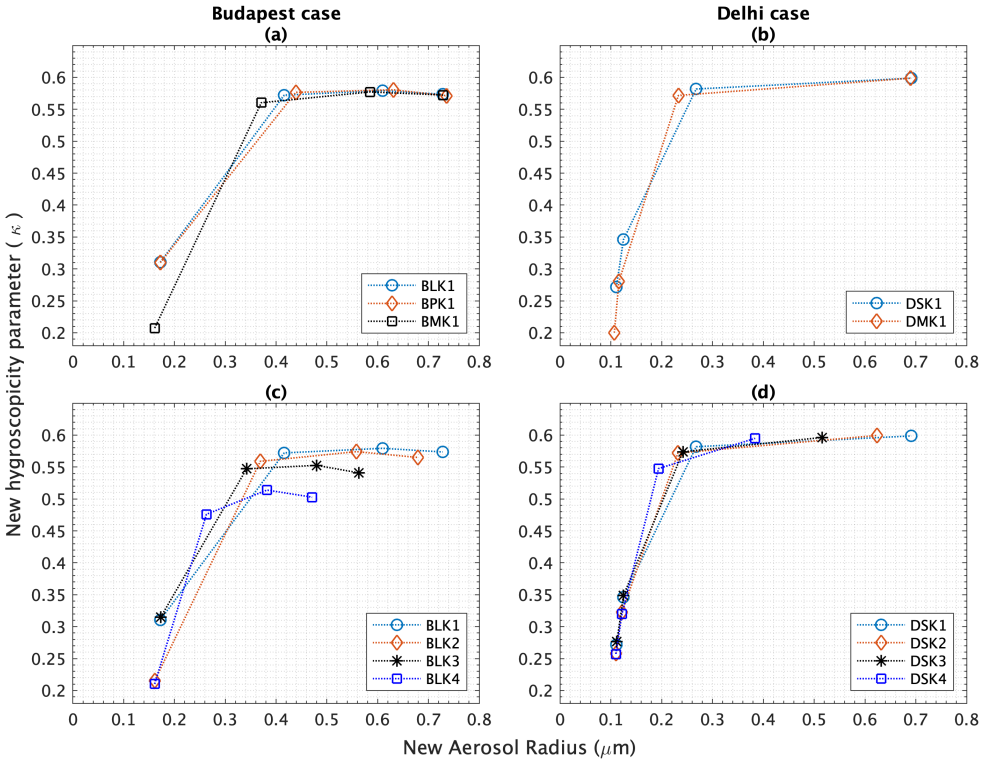

Figure 21: New hygroscopicity parameter for the regenerated aerosol particles at end of fog for the Budapest and Delhi cases. (a), (b) are the size independence hygroscopicity over Budapest and Delhi. (c), (d) are the chemistry independency hygroscopicity over Budapest and Delhi.

hygroscopicity has no effect on the hygroscopicity of the regenerated aerosol particles with a radius larger than 0.3 μm in neither the Budapest nor in Delhi cases. This finding stems from the fact that the chemical processes occurring in the liquid drops formed on LH aerosol particles do not depend on the value of hygroscopicity. In the Budapest case the final hygroscopicity depends on the initial concentration of the trace gases. While in BLK1 and BLK2 cases the hygroscopicity increases to nearly 0.6 for the radius larger than 0.3 μm due to a large amount of SO_2 and the presence of HNO_3 in the BLK1 case, meanwhile in the BLK4 cases the hygroscopicity increases only to 0.5. In the Delhi case, the hygroscopicity of the regenerated aerosol particles do not vary from case to case due to the high amount of trace gas concentration available in the environment in each investigated case.

6.4 WRF sensitivity results

6.4.1 Observations

Research was extended further from 1D model experiments to mesoscale modeling by using Weather Research and Forecast (WRF) Model. For this modeling experiment we

have taken the fog event occurred on 24-November-2020 morning time as a case study. Figure 22 shows the EUMETSAT satellite image of wide covered fog over Hungary at 24-November-2020 07:10 local time. At this time most of cloud path covered eastern and north-west part of Hungary.

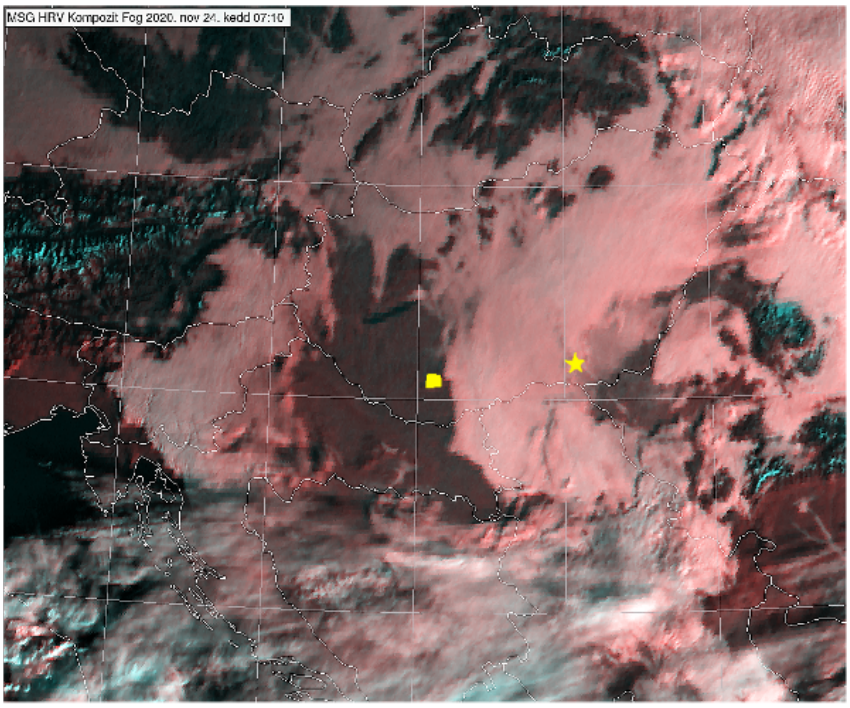

Figure 22: Satellite image of fog at 24-Nov-2020 07:10 CET (06:10 UTC). [Square symbol shows Pécs and Star symbol shows Szeged meteorological stations.]

The time evolution of back scatter profile observed by ceilometer over Pécs and Szeged is depicted in the Figure 23. Figure 23 shows that while at Szeged fog existed during morning, and before noon fog lifted up due to solar radiation, at Pécs fog did not formed, only low level cloud was detected at late afternoon. Satellite image also shown that presence and absence of fog at the observational sites of Pécs and Szeged (Figure 22).

Figure 24 shows the diurnal cycle of temperature, relative humidity, visibility, and wind speed at Pécs and Szeged. In Figure 24g, black sold line shows the visibility calculated from ceilometer back scattered data over Szeged. The color lines denote simulated visibility (at first model level) using different PBL schemes. A continues temperature decrease before fog onset and sharp decrease in seen immediately after the fog onset, and the wind parameter remained low until the end of the fog event over Szeged. Calm winds and continues temperature drops are showing favorable conditions for fog formation. In consistent with this variation, visibility decreases sharply early morning and becomes as low as 200 m at 04:30 UTC, indicating the presence of fog. It increases sharply in response to increasing temperature until about 09:30 UTC (Figure 24g). In this study we focused on

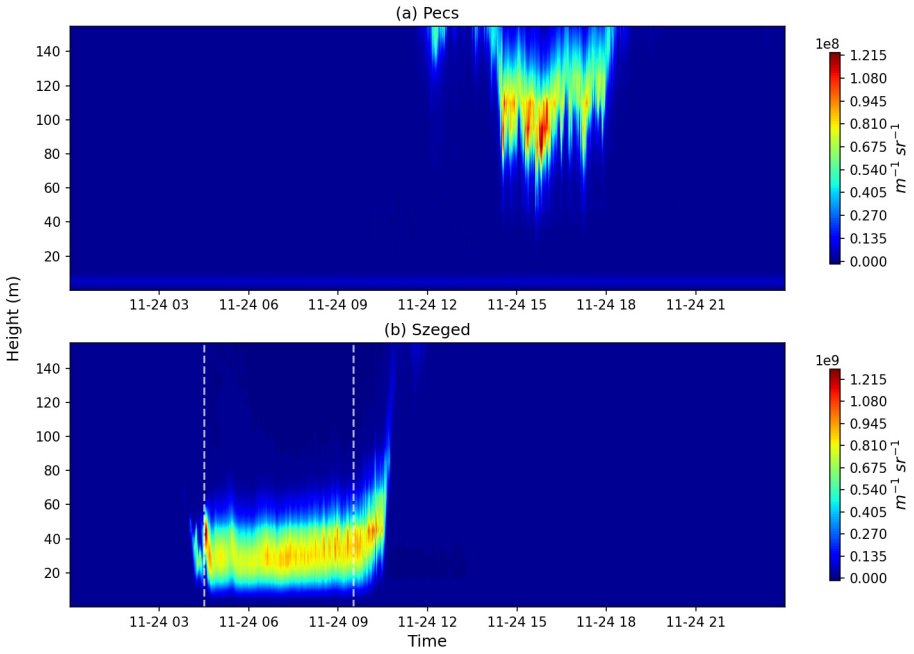

Figure 23: Back scatter data from Pécs (a) and Szeged (b) on 24-Nov-2020

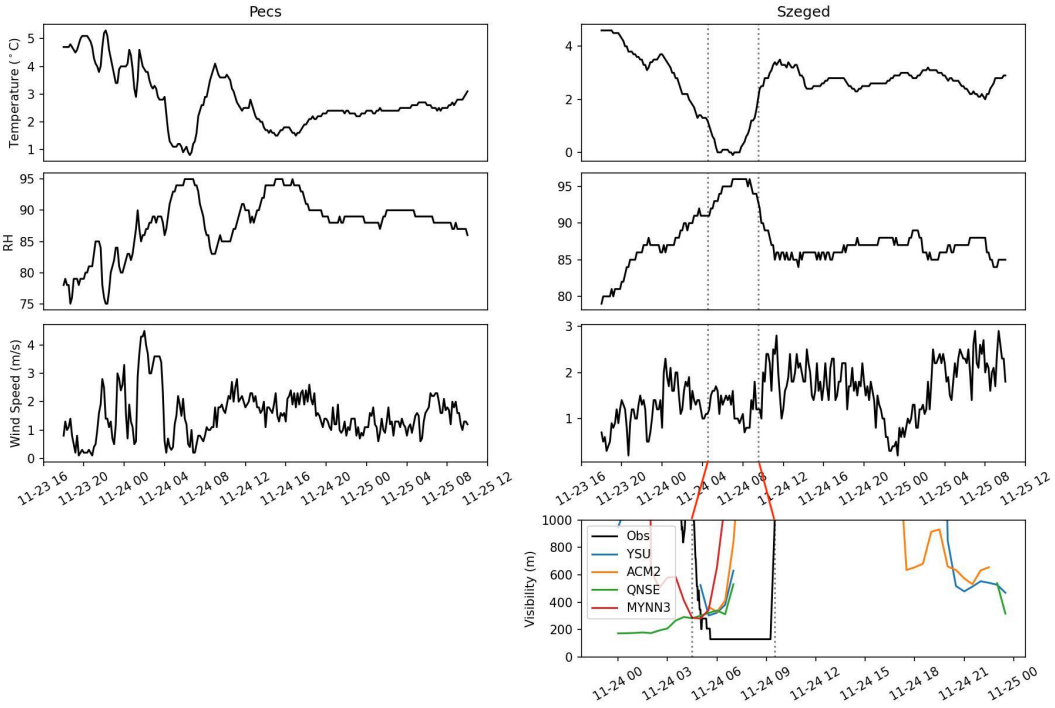

Figure 24: Time evolution of the surface meteorological parameters over Pécs and Szeged. Visibility data are plotted only at Szeged, because fog was not detected at Pécs.

sensitivity of the fog simulation on PBL parametrization.

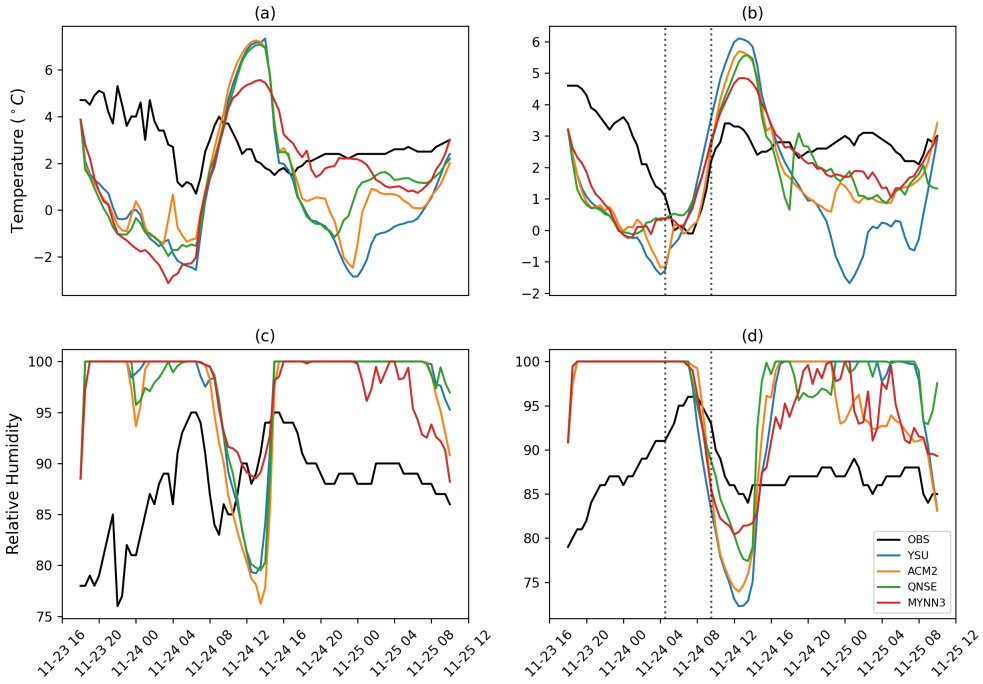

Figure 25: Comparing the Pécs and Szeged weather station data with model 2 m temperature (a), (b) and relative humidity (c), (d) at different WRF PBL schemes.

6.4.2 Analysis of the model data

Model (1st level) corresponding grid point 2 m temperature (hereafter T2) is evaluated by directly comparing observation data measured at Pécs and Szeged locations (Figure 25). However, magnitudes of simulated surface variables differed among various PBL runs. It was found that in all sensitivity runs the simulated T2 suffers from substantial warm and cold bias during daytime and nighttime (approximately 3 – 5 °C; Figure 25). However, fog event was noticed in Szeged at 24-Nov-2020 between 04:30 – 09:30 UTC and no fog event was noticed in Pécs weather station (Figure 23). The best fitting between the observed and simulated T2, RH occurs in the case of MYNN3 scheme. Cold bias can be observed in nighttime at non-foggy period compared to foggy period (Szeged at 24-Nov-2020).

Figure 26 shows the heatmap of calculated error statistics for the PBL sensitivities for the simulation of fog period at Szeged station and Pécs to reveal the performance of the model with each PBL and to identify the better performing of schemes. Figure 26 gives the mean absolute error (MAE) and root mean square error (RMSE) statistics for temperature (T), wind speed, and relative humidity (RH) at Pécs and Szeged. ACM2 PBL scheme produced comparatively better MAE and RMSE values for the temperature at both locations (Pécs: 0.94 and 1.54 °C, Szeged: 0.2 and 0.85 °C) during the fog period. YSU

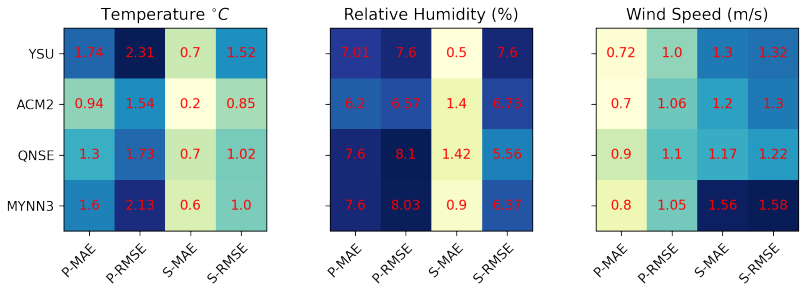

Figure 26: Heat map of error statistics for the PBL sensitivity simulations over Pécs and Szeged for the observed fog period (see the vertical dashed line in Figure 25b and d). Note: P-MAE indicates the mean absolute error over Pécs and P-RMSE indicates root mean square error over Pécs. S-MAE indicates the mean absolute error over Szeged and P-RMSE indicates root mean square error over Szeged.

scheme shows the largest of temperature bias, and it results in the largest mean absolute error and root mean square error. In the case of relative humidity ACM2 gave better result only with MAE and RMSE over Pécs but YSU scheme has low MAE and QNSE has low RMSE value over Szeged. For wind speed ACM2 have low MAE and MYNN3 has low RMSE values over Pécs and QNSE has low MAE and RMSE values in Szeged. But if we consider the whole simulation period MYNN3 shown relatively less values. Comparison of the observed and simulated time profiles of temperature (Figure 25a and 25c) shows the temperature was underestimated during middle nights by numerical simulation (independently of the applied PBL schemes) and was overestimated during afternoon time at both Pécs and Szeged locations. However, all PBL schemes simulated well the change of the temperature during morning time and MYNN3 scheme slightly better than others in throughout the simulation period. While calculated relative humidity was near to 100 % during almost whole simulated time period, the observed RH never reached this maximum value (Note, the observation error about RH). However, the decrease of simulated RH starts earlier, and it is steeper than the observed one.

Figure 27 shows the vertical profile of temperature and RH in three phases of the fog evolution such as before fog onset (24-Nov-2020 00:00 UTC), during the fog (24-Nov-2020 06:00 UTC) and after the fog (24-Nov-2020 10:30 UTC) at a grid point near Szeged. In the Figure 27a, 27d the calculated vertical profiles of temperature and RH are compared with sounding profile. (The observed profiles are plotted only in Figure 27a and 27d, because sounding data are available only at 00:00 UTC.) The numerical simulation underestimates the temperature in the layer of 0 ~ 200 m. While YSU and MYNN3 PBL schemes, similarly to the observed profile, result in strong inversion below 100 m from surface, ACM2 and QNSE PBL schemes perform inversion layer started above the surface. The RH is overestimated

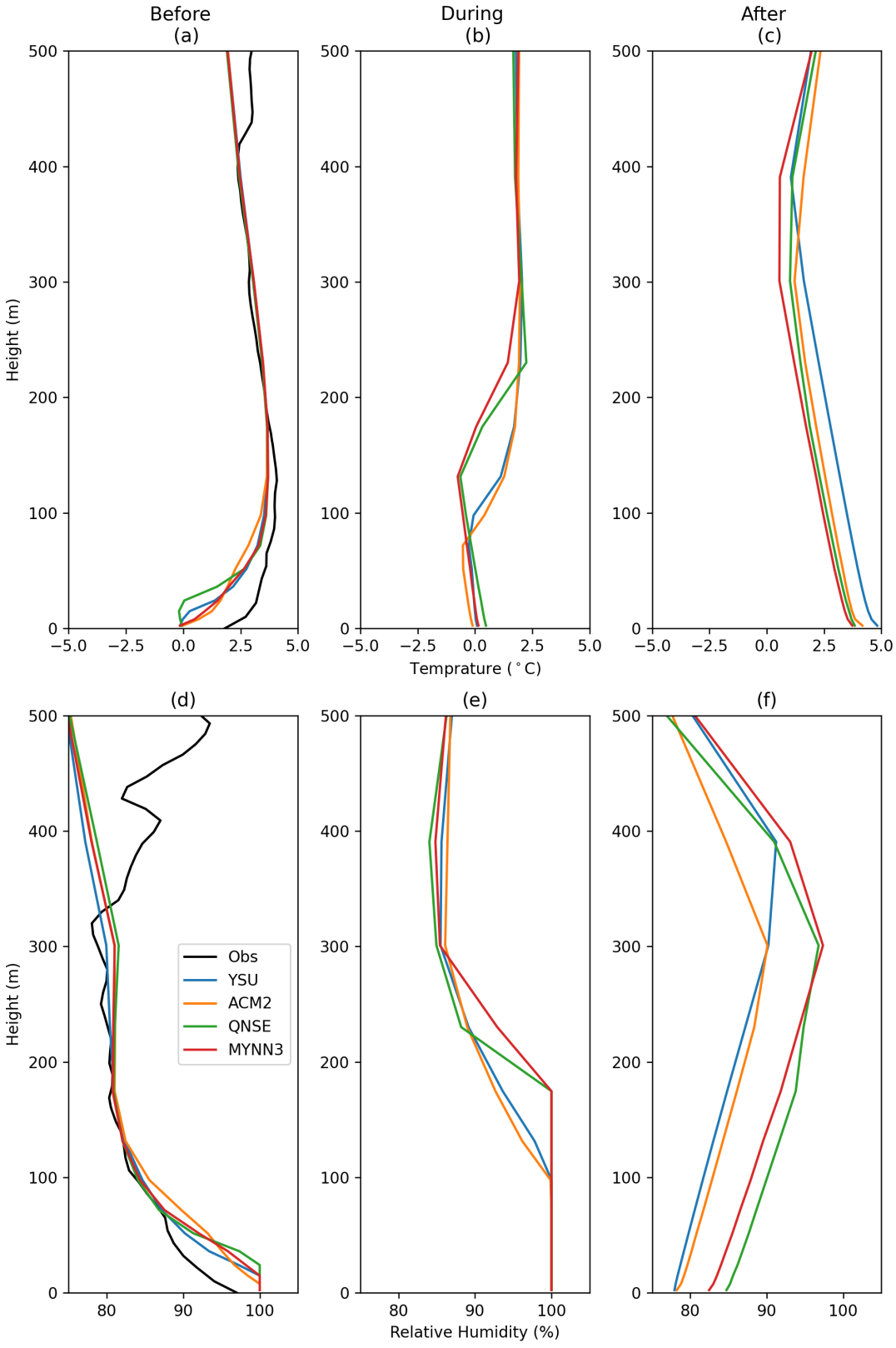

Figure 27: Before (a, d), during (b, e) and after (c, f) the fog vertical profile of temperature (1st row) and relative humidity (2nd row) over Szeged.

in each case in a very shallow layer of about 50 m. Note: the observation error can be significant when the atmosphere is near the saturation. The applied PBL parameterization technique significantly impacts the vertical profiles during and after the fog. The non-local

schemes (YSU and ACM2) result in shallower fog layer than the local schemes (QNSE and MYNN3). The layer characterized by 100% RH and altitude of the inversion layer is deeper in the case local PBL schemes than in the case of the non-local schemes (Figure 27b and 27e). The altitude of the inversion layer approximately should coincide with the top of the fog. The plots about RH also supported above statements. During the fog event the atmosphere is saturated near the surface and the depth of the saturated layer correspond to the altitude of inversion layer (Figure 27e and 27b). The difference between the local and non-local schemes are more conspicuous if the RH profiles are compared in Figure 27f.

6.4.3 Liquid Water content (LWC)

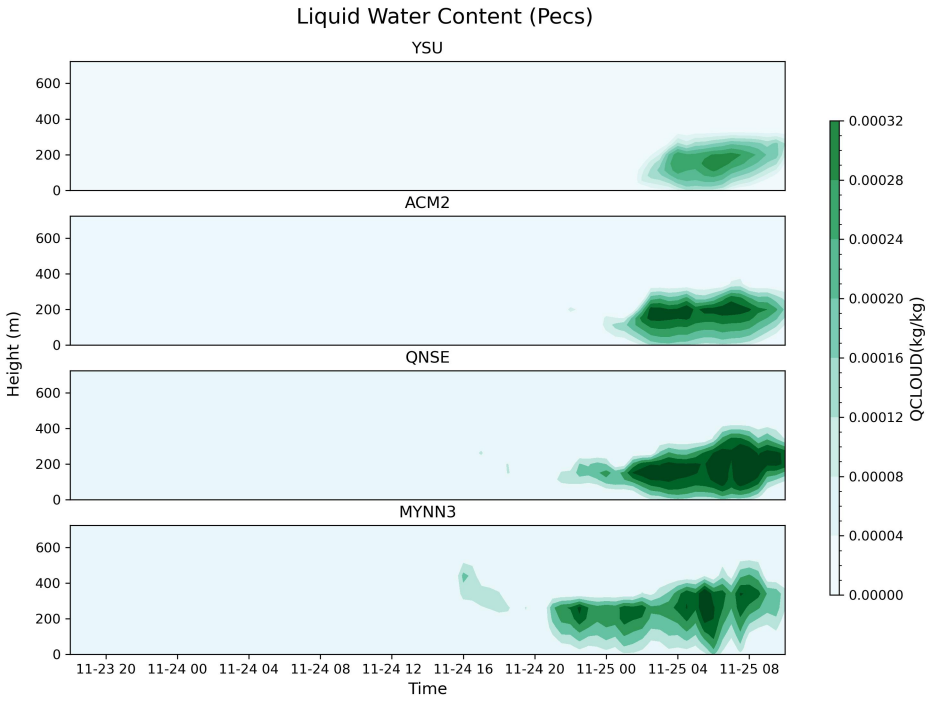

Figure 28: Time series of vertical profile of LWC over Pécs

The processes occur in PBL affect not only the dynamics and thermodynamics of the atmosphere, but also impact the fog microphysics. The most important characteristic of the fog is the amount of the condensed vapor, the liquid water content (hereafter LWC). In this section the results about the sensitivity of the LWC on the applied PBL schemes are presented. The objective is to determine which PBL scheme is able to simulate more accurately the characteristics (e.g., duration, visibility) of the fog successfully. Figure 28, Figure 29 shows the PBL sensitivity results of simulated time series of vertical profile of

LWC at the grid points near the location of the observation at Pecs and Szeged. These plots clearly correspond to back scatter data (Figure 23). Over Pecs both the observation and the numerical simulation exclude the fog formation during morning on 24th November. At the location of Szeged, the WRF simulations with each PBL scheme produce fog during the early morning on 24th November.

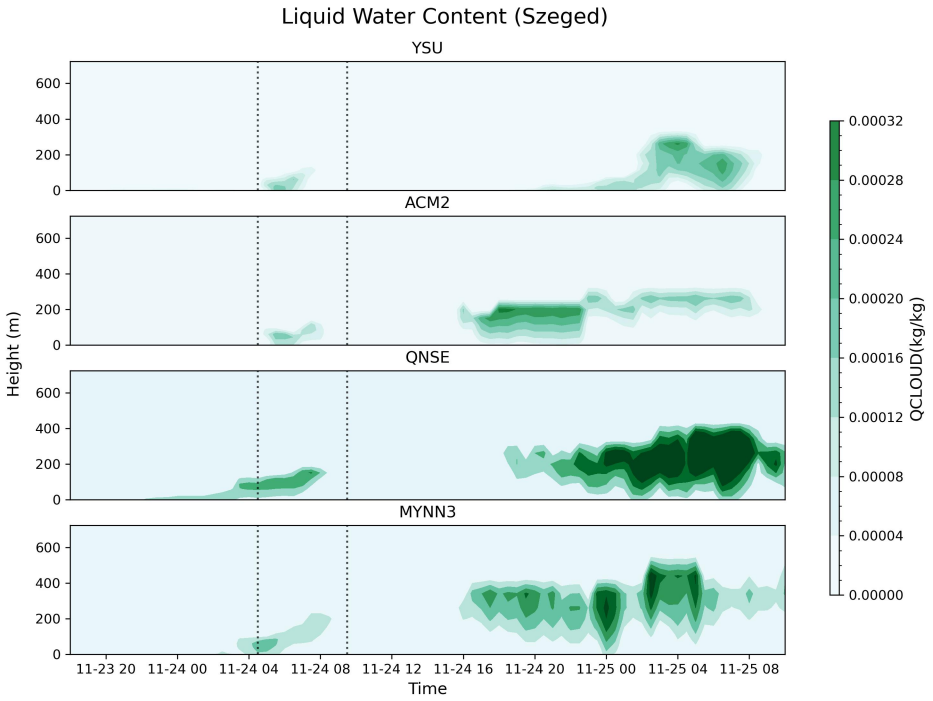

Figure 29: Time series of vertical profile of LWC over Szeged

The simulated onset time of the fog is not accurate comparing with the ceilometer data and all the PBL schemes produced early fog onset at model first level (Figure 24g). YSU and ACM2 schemes produced less amount of LWC at fog onset (04:30 UTC). QNSE and MYNN3 schemes produced significantly high amount of LWC at fog onset (04:30 UTC) and its corresponding to low visibility (Figure 24g). However, numerical models forecast significantly earlier dissipation of the fog. The different PBL schemes result in fog with different lifetimes, LWC and thicknesses. YSU and ACM2 schemes simulate significantly smaller LWC compared to QNSE and MYNN3 schemes. The faster dissipation of the fog in the case of YSU and ACM2 schemes can be explained by the fact, that these schemes are characterized by producing warmer and drier daytime in the PBL (Cohen et al., 2015). QNSE scheme seems to overestimate both the LWC and duration of the fog due to it depicts too cool, moist shallow PBL for simulations (Cohen et al., 2015; Sukoriansky et al., 2005). Our results support the results published by (Nakanishi and Niino, 2006) that MYNN3 PBL

scheme reasonably depicts the formation of the statically stable boundary layer, which contributes the reliable simulations of radiation fog. The LWC are integrated for entire model domain (below 1000 m height) to analyze the impact of the different PBL schemes on the drop formation. Figure 30 shows the histograms about the frequency of the LWC for different ranges of mixing ratios at the simulation time of 24-Nov-2020 06:00 UTC. The height of the columns means the integrated LWC over the domain at each range of the mixing ratio. The most evident characteristics of the histograms that while QNSE scheme produces significantly larger amount of LWC in the last three ranges than the three other PBL schemes, the MYNN3 schemes results in more liquid drops at the smaller ranges and less liquid in the larger ranges.

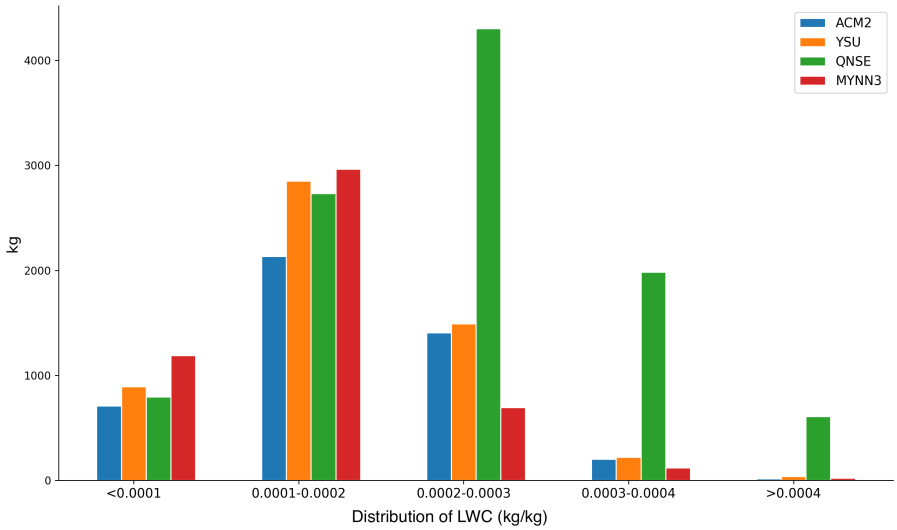

Figure 30: Histograms of the domain integrated LWC at different ranges at the simulation time of 24-Nov-2020 06:00 UTC (approximately at the middle of the fog period).

Figure 31 shows spatial distribution of LWC at the model first level in the case of the different PBL schemes at 24-Nov-2020 06:00 UTC. All the schemes produced LWC over a relatively large area in the eastern and west-north part of Hungary. The numerical simulation using MYNN3 PBL scheme gives the best agreement with the satellite observation (Figure 22). While QNSE scheme produces large values of LWC and overestimate the horizontal extension of the fog, the two other schemes underestimate the horizontal extension of the fog near the southern border of Hungary.

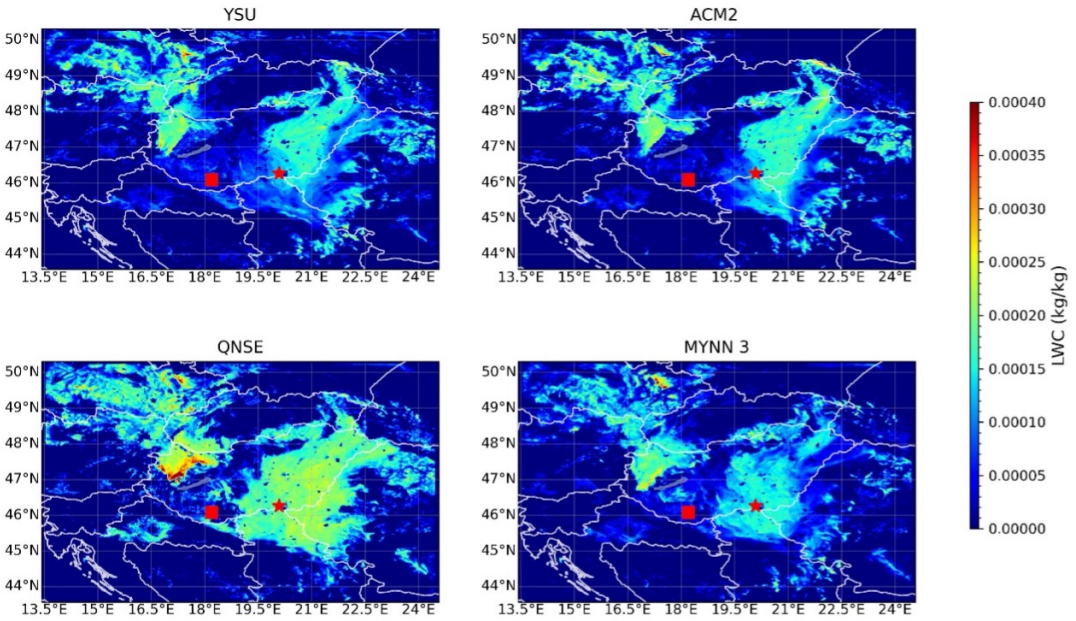

Figure 31: Spatial distribution of LWC at 24-Nov-2020 06:00 UTC at the altitude of 6 m.

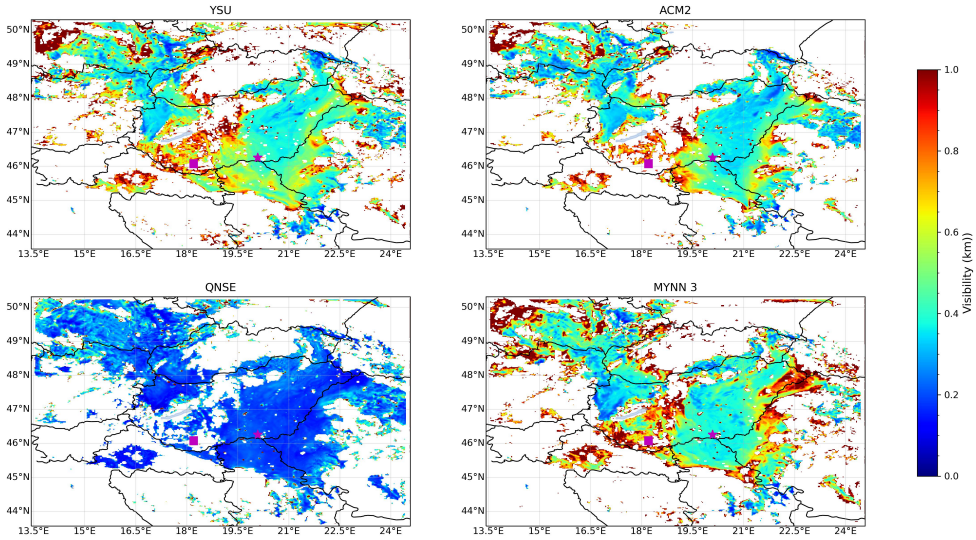

Figure 32: Spatial visibility over 10 m height (first model level) at 24-Nov-2020 06:00 UTC

6.4.4 Visibility calculation

The forecast of the visibility is one of the largest challenges for meteorologists. As it was presented above the LWC is impacted not only by the cloud microphysics, but the accurate simulation of PBL processes is also required. Even more, although the impact of the soil or that of the radiation has not been studied in this research, they also play important role in the fog evolution. Another issue is that the visibility can be evaluated accurately

if the size distribution of the drops in the fog is available (see eq. 33). Unfortunately, the implementation of bin microphysical scheme in the operational weather forecast numerical model is not an option. So a parameterized formula should be applied to estimate the visibility. Two-moment bulk microphysical schemes predict both the number concentration of liquid drops and LWC allow a more sophisticated evaluation of the visibility than the one-moment schemes (they forecast only the LWC). Gultepe et al. (2006b) asserted that evaluation of visibility without taking into consideration of the variability in Nd could cause 50% uncertainty in the estimation of the visibility. In this study we calculate visibility by substituting the forecasted LWC and drop concentration in the equation as follows (Song et al., 2019):

$$\text{Vis} = \frac{0.511}{(LWC \times N_d)^{0.52}} \tag{33}$$

Figure 32, shows the calculated ground (first model) level spatial visibility at 24-Nov-2020 06:00 UTC and noticed the spatial distribution is corresponded with satellite image. Figure 24g shows the time evolution of the observed and simulated visibility. All PBL schemes results in early onset of fog (Figure 24g), even more, QNSE scheme produced visibility less than 200 m at model fog onset and started to increase the visibility at fog onset observed. Both non-local schemes (YSU and ACM2) were produced visibility greater than 500 m at model fog onset and significantly start decreasing after fog onset observed. Among all PBL schemes MYNN3 results in significant decrease of visibility slightly before observed fog onset (04:30 UTC) and maintained low visibility until few hours of fog, and it results in earlier dissipation comparing with other observation (Figure 24g).

7 Discussion

A detailed, bin scheme was developed to simulate the life cycle of the fog. The impact of neglecting the dynamic and radiation processes were lessened by tracking the simulated time profile of the temperature with the observed time profile. The simulated life cycle of fog is in line with the observed life cycle in the Budapest case, while a slight bias occurs in the Delhi case. The simplified fog dynamic allows us to focus on the different types of scavenging processes and tracking the evolution of the drop size distribution formed on both activated and interstitial aerosol particles and haze particles. To the extent of the knowledge of the mine, a bin scheme has been never implemented in a numerical model

for the simulation of liquid chemistry in fog and this is complete novel approach.

The role of the scavenging processes in clouds has been published in many papers (Flossmann et al., 1985). While in the clouds, the activation significantly reduces the number concentration of the hygroscopic particles and the scavenging processes play a less important role (Geresdi et al., 2005), in the fog due to the very small value of supersaturation, the activation has a very small role in reducing the number concentration of hygroscopic aerosol particles. However, a self-cleaning (scavenging) process explained through Brownian motion and phoretic force in fog (Figure 16) significantly reduces the number concentration of aerosol particles with a radius less than 0.1 μm (Figure 17 and Figure 18). Although the rate of the Brownian and phoretic scavenging is small, they can have significant impact due to the long lifetime of the fog. The number concentration of activated aerosol particles is about one order of magnitude less than the decrease of the number concentration due to Brownian and phoretic scavenging. Note, the hygroscopicity of the LH particles is less than 0.5 (Table 4) in our simulated cases. The role of activation scavenging can be more important if the hygroscopicity of the aerosol particles is significantly larger than in our case studies (Gilardoni et al., 2014). On the basis of their field observation performed in Indo Gangetic Plain, Izhar et al. (2020) also concluded that the scavenging processes significantly reduce the amount of the aerosol in fog. The results of our study suggest that the initial size dependence of the hygroscopicity of aerosol particles can have a significant effect on the efficiency of Brownian scavenging. Unfortunately, the size dependence of the hygroscopicity is not available from most of the field observations. However, some field experiment suggests that aerosol particles with a radius smaller than 100 nm are mostly hydrophobic (e.g., Wang et al. (2018); Enroth et al. (2018)). Our results show that these small aerosol particles are efficiently collected by the fog droplets due to the long lifetime of the fog. The role of the phoretic forces in the impaction scavenging is controversial. Geresdi et al. (2005) asserted that phoretic force has no significant impact in stratified clouds when compared to activation. However, our sensitivity test reveals that the efficiency of phoretic scavenging can be more decisive, and its role in reducing the concentration of aerosol particles with a radius about 0.1 μm depends on the duration of the onset and dissipation periods of the fog.

The dashed lines in Figure 10c and Figure 14c reveal the simulated time profiles of the particle concentration (aerosol particles as well as both haze particles and droplets are

considered). Due to the applied observational technique, these plots show not only the interstitial aerosol particles but include aerosol particles inside the water drops (activated aerosol particles). As such, the sedimentation of fog drops, and the impaction scavenging should have resulted in the observed decrease of the aerosol particle concentration. Although in our model the local emission and the advection of the particles, as well as the sedimentation of the fog drops are not taken into consideration in the Budapest case, the time profile of the simulated concentration is in line with the observation data which is to say that the decrease of the particle concentration in the Budapest case can be explained by the scavenging processes. In the Delhi case, the difference between the simulated and observed profiles is significant. This difference between the two cases may stem from the fact that while in downtown Budapest the emission rate due to local sources (vehicle traffic) must have been small during the night, in the Delhi case the local emission due to the exhaust of airplanes is significant even during the night (see spikes in the observed time profile of the particle concentration in Figure 14c). The advantages of using bin resolved liquid chemistry against the bulk chemistry was published by Schmeller and Geresdi (2019). Due to the size resolved simulation of the liquid chemistry the model output allows to reveal both the size dependence of the pH of the fog drops and the bulk pH. Because during the field projects the size resolved pH values are not available, the time profiles of the bulk pH are plotted in Figure 19g and h. The lower pH in the Delhi case compared to the Budapest case is in line with results published by Wang et al. (2020). They asserted that fog formed in less polluted air mass had much higher pH than polluted haze even under high ammonia (NH_3) conditions. Ghude et al. (2017) showed the fog water pH varied between 6.12–7.62 with an average of 6.91, which indicates the alkaline nature over Delhi. Also, Nath and Yadav (2018) published results about analyzing the chemical compounds in fog and dew samples collected during the winter of 2014–2015 over Delhi (7 km distance from WIFEX site) and reported the mean bulk ion concentrations inside the drops and bulk pH of the droplets. They found that the pH of the droplets is more acidic, and it changes between 4.0 and 6.6, and that the ratio of the masses of the two acidic compounds of $S(VI)$ and $NO_3^-$was about two. Comparison of this observed data with our simulated results is not evident, because data about trace gas concentrations was not published in this paper. However, the ratio of the masses of the two acidic compounds ($S(VI)/NO_3^-$) and the calculated pH of the fog drops for the DSK1 and DMK1 cases (Figure 19h and Figure 20) agree well with the observations of Nath and Yadav (2018). While the simulated value of the acidic component ratio was ~2.3, the published data was 2.2. While

the simulated value of the pH is in the range of 5.2 - 6, the published data was 4.0 – 6.6. However, our results also shows that the pH of the drops can change in wide intervals during the evolution of the fog in highly polluted atmospheres even in the mature period. As such, the measured pH may depend on the timing of the sampling.

The importance of the fog – aerosol interaction has been presented in a number of papers (e.g., Boutle et al. (2018)). These studies have mostly focused on the microphysical processes, and less attention has been devoted to the aging of the aerosol particles due to liquid chemistry in fog (e.g., Izhar et al. (2020)). The bin resolved liquid chemistry model allows us to track the changes in the chemical composition of each bin. Due to liquid chemistry in fog droplets, both the chemical composition and the mass of the aerosol particles are subject to change. Figure 17a, 17c and Figure 18a, 18c, show the aerosol size distribution along with time and the broadening of the spectrum (mostly at larger particles) for both the Budapest and the Delhi case. These regenerated aerosols contain ionic compounds which formed through the liquid chemistry and have more hygroscopicity due to their ionic nature. This result of our numerical experiment is in line with the findings of a field experiment published by (Izhar et al., 2020). They asserted, that the enhancement of sulfate concentration in fog water was due to the liquid chemistry, which results in an increase of the aerosol mass after the evaporation of fog droplets. The enhancement of the hygroscopicity (Figure 21) can impact the evolution of the fog as follows: (i) The dissipation of the fog can be mitigated by the enhanced solution effect. (ii) The increased solubility of the regenerated aerosol particles can assist the formation of the successive fog formation. In this study the simulation of liquid chemistry is confined to the drops larger than 1 μm. Because supersaturation is small in the fog, the initial size of the aerosol particles inside these drops is larger than 0.1 μm. As such, we cannot follow the impact of the liquid chemistry in the case aerosol particles smaller than 0.1 μm, and we cannot deduce how the liquid chemistry impacts the size dependence of the hygroscopicity of these small aerosol particles. We can conclude that due to the long residence time of the droplets in the fog, the liquid chemistry has a strong impact on the hygroscopicity of the regenerated aerosol particles, and in a more polluted atmosphere the hygroscopicity becomes larger than in a less polluted atmosphere.

A detailed PBL sensitivity experiments have been accomplished by using numerical mesoscale model (WRF) to understand the model ability for fog prediction. The results of

four different PBL schemes have been compared by simulating numerically a fog event, occurred in time period of 24-November-2020 04:30 UTC - 24-November-2020 09:30 UTC. These schemes involve different parametrization for the turbulence contributes to mixing of heat and moisture. The model data are compared with observational data such as surface temperature, backscatter data from ceilometer measured at two locations Pecs, Szeged, and radio sounding data at Szeged. Agreement with the observation the numerical models, independently off the applied PBL schemes, provide fog at Szeged, do not provide at Pecs. Strong impact of the boundary layer processes on fog microphysics is proved by comparing the LWC calculated by using different PBL schemes. Unfortunately, observation data about the LWC is not available for this fog event. So, comparison of the satellite observation and visibility data (it depends on both the drop concentration and LWC) with the model results, allows us to validate the simulated values. The QNSE results in unrealistic such as early fog formation, high amount of LWC and underestimated visibility at fog onset. The numerical models are not able to forecast the duration (too early onset and early dissipation) of the fog independently which PBL schemes are used (Figure 24g). Figure 24g, shows that all the PBL schemes are simulated early onset fog over Szeged and understand that not particular scheme is suitable fog forecasting. Based on our simulations, previous publications (Pithani et al., 2018, 2019; Smith et al., 2021) and the calculated characteristics, MYNN3 scheme is suggested to use for the numerical forecast of the fog.

8 Conclusions

The interaction between fog microphysics and liquid chemistry was examined with a 1D model for two distinctive locations of Budapest, Hungary and Delhi, India. This model involves a detailed moving bin microphysics scheme to properly simulate the diffusional growth and evaporation of water drops, as well as the liquid chemistry. A comprehensive sensitivity study has been carried out to investigate how the initial hygroscopicity of aerosol impacts the scavenging of sub-micron particles through different mechanisms, and liquid chemistry. Also, the impact of atmospheric pollution characterised by the concentration of $SO_2, H_2O_2, O_3, HNO_3, CO_2$ and NH_3 gases on $NH_4^+, NO_3^-, S(VI)$ accumulating inside of water drops is studied. On the base of the results of the numerical simulations the conclusions are as follows:

- Due to the low supersaturation, particle scavenging through activation nucleation

is less important than other mechanisms, such as Brownian and phoretic. On an average, 40 - 50% total particles are collected due to impact scavenging (Figure 16), and less than 1% of the LH particles are activated due to the low supersaturation and small hygroscopicity of the LH particles.

- The role of phoretic scavenging depends on the concentration of aerosol particles with a radius around 0.1 μm, as well as on the duration of the dissipation phase of the fog.

- Due to the long duration of the fog, the droplets absorb significant amounts of different trace gases. The presence and absorption of ammonia promote the absorption of SO_2 the sulphate formation is very efficient in the simulated cases.

- The acidity of the drops is affected not only by the liquid chemistry, but it also depends on the diffusional growth of the drops. While the increase of the LWC results in the increase of the bulk pH, the evaporation of the drops in the dissipation periods significantly reduces the pH.

- Our numerical model allows us to track the accumulation of chemical compounds such as $S(VI), NH_4^+, NO_3^-$inside of the drops. Additionally, it should be noted that the size dependence of hygroscopicity has no effect on the liquid chemistry occurring in the drops.

- The results reveal that liquid chemistry contributes to the broadening of the aerosol size distribution (regenerated aerosol or aging of the aerosol), and significantly increases the hygroscopicity of the regenerated aerosol particles formed after the evaporation of the liquid phase. This increased hygroscopicity may impact the duration of fog dissipation by enhancing the solution effect and helps to promote successive fog event in favorable environmental conditions.

Thermodynamics and dynamics occur in PBL plays fundamental role in fog formation. In this research a sensitivity test was accomplished to study how the parametrization of PBL processes impact the accuracy of the fog forecast. The conclusions of PBL sensitivity experiment are as follows:

- The parametrization of the PBL schemes significantly impacts the fog microphysics. The results about the LWC are very sensitive on the applied PBL schemes. While QNSE scheme results in unrealistic early formation of the fog (and too large LWC),

the duration of the fog is rather short if the non-local schemes (YSU and ACM2) are applied. Although even the MYNN3 scheme results in too early dissipation of the fog, the results suggests that MYNN3 is well suitable for fog prediction over Hungary.

- Unfortunately, all the simulation results (independently of the applied PBL scheme) show the dissipation of the fog starts too early (Pithani et al., 2018, 2019). The reason of this is not known. Because not only PBL processes, but the interaction between the atmosphere and the soil, and the effect of the radiation can be also decisive further research is required to solve this problem.

Acknowledgment

I am incredibly grateful to my supervisor Professor István Geresdi, Institute of Geography and Earth Sciences, Faculty of Science, University of Pecs, Hungary. This work would be impossible without his unlimited patience, noble guidance, and continuous support in every step of my PhD studies. I wish to offer my sincere thanks to faculty members of the Institute of Geography, Faculty of Science, University of Pecs, Hungary, for their kind support and encouragement during my study. I am obliged to administrative staff members of the University of Pecs for their co-operation during my PhD program. I can't thank enough my office mates for being there for me when I needed help. Last but not least, I would also like to thank all my friends and family members for encouraging and supporting me whenever I needed them. I extend my thank to the Ministry of Finance, the Hungarian Scientific Research Fund (K132254) for research support and the Tempus public foundation for the scholarship (Stipendium Hungaricum) for my PhD.

References

Acharja, P., Ali, K., Trivedi, D. K., Safai, P. D., Ghude, S., Prabhakaran, T., and Rajeevan, M. (2020). Characterization of atmospheric trace gases and water soluble inorganic chemical ions of PM1 and PM2.5 at Indira Gandhi International Airport, New Delhi during 2017-18 winter. *The Science of the total environment*, 729:138800.

Arub, Z., Bhandari, S., Gani, S., Apte, J. S., Hildebrandt Ruiz, L., and Habib, G. (2020). Air mass physiochemical characteristics over New Delhi: impacts on aerosol hygroscopicity and cloud condensation nuclei (CCN) formation. *Atmospheric Chemistry and Physics*, 20(11):6953–6971.

Badarinath, K. V., Kharol, S. K., Sharma, A. R., and Roy, P. S. (2009). Fog Over Indo-Gangetic Plains—A Study Using Multisatellite Data and Ground Observations. *IEEE Journal of Selected Topics in Applied Earth Observations and Remote Sensing*, 2(3):185–195.

Benjamin, S. G. and al., E. (2004). An hourly assimilation/forecast cycle: the RUC model. *Mon. Weath. Rev*, 132:495–518.

Benoit, R., Desgagné, M., Pellerin, P., Pellerin, S., Chartier, Y., and Desjardins, S. (1997). The Canadian MC2: A semi-Lagrangian, semi-implicit wideband atmospheric model suited for finescale process studies and simulation. *Monthly Weather Review*, 125(10):2382–2415.

Boutle, I., Price, J., Kudzotsa, I., Kokkola, H., and Romakkaniemi, S. (2018). Aerosol-fog interaction and the transition to well-mixed radiation fog. *Atmospheric Chemistry and Physics*, 18(11):7827–7840.

Cereceda, P., Larrain, H., Osses, P., Farías, M., and Egaña, I. (2008). The spatial and temporal variability of fog and its relation to fog oases in the Atacama Desert, Chile. *Atmospheric Research*, 87(3-4):312–323.

Chaouch, N., Temimi, M., Weston, M., and Ghedira, H. (2017). Sensitivity of the meteorological model WRF-ARW to planetary boundary layer schemes during fog conditions in a coastal arid region. *Atmospheric Research*, 187:106–127.

Chen, C., Zhang, M., Perrie, W., Chang, R., Chen, X., Duplessis, P., and Wheeler, M. (2020). Boundary Layer Parameterizations to Simulate Fog Over Atlantic Canada Waters. *Earth and Space Science*, 7(3).

Chen, F. and Dudhia, J. (2001). Coupling an advanced land surface–hydrology model with the Penn State–NCAR MM5 modeling system. Part I: Model implementation and sensitivity. *Monthly weather review*, 129(4):569–585.

Chin, M., Ginoux, P., Kinne, S., Torres, O., Holben, B. N., Duncan, B. N., Martin, R. V., Logan, J. A., Higurashi, A., and Nakajima, T. (2002). Tropospheric aerosol optical thickness from the GOCART model and comparisons with satellite and sun photometer measurements. *Journal of the Atmospheric Sciences*, 59(3 PT 1):461–483.

Cohen, A. E., Cavallo, S. M., Coniglio, M. C., and Brooks, H. E. (2015). A review of planetary boundary layer parameterization schemes and their sensitivity in simulating southeastern U.S. cold season severe weather environments. *Weather and Forecasting*, 30(3):591–612.

Collett, J. L., Herckes, P., Youngster, S., and Lee, T. (2008). Processing of atmospheric organic matter by California radiation fogs. *Atmospheric Research*, 87(3-4):232–241.

Coniglio, M. C. (2012). Verification of RUC 0-1-h forecasts and SPC mesoscale analyses using VORTEX2 soundings. *Weather and Forecasting*, 27(3):667–683.

Cséplő, A., Sarkadi, N., Horváth, Á., Schmeller, G., and Lemler, T. (2019). Fog climatology in Hungary. *Idojaras*, 123(2):241–264.

Dimri, A. P., Niyogi, D., Barros, A. P., Ridley, J., Mohanty, U. C., Yasunari, T., and Sikka, D. R. (2015). Western Disturbances: A review. *Reviews of Geophysics*, 53(2):225–246.

Dunn, M. (1989). *Exploring your world: The adventure of geography*. National Geographic Society.

Elbert, W., Hoffmann, M. R., Krämer, M., Schmitt, G., and Andreae, M. O. (2000). Control of solute concentrations in cloud and fog water by liquid water content. *Atmospheric Environment*, 34(7):1109–1122.

Enroth, J., Mikkilä, J., Németh, Z., Kulmala, M., and Salma, I. (2018). Wintertime hygroscopicity and volatility of ambient urban aerosol particles. *Atmospheric Chemistry and Physics*, 18(7):4533–4548.

Fisak, J., Tesar, M., Rezacova, D., Elias, V., Weignerova, V., and Fottova, D. (2002). Pollutant concentrations in fog and low cloud water at selected sites of the Czech Republic. *Atmospheric Research*, 64(1-4):75–87.

Flossmann, A. I., Hall, W. D., and Pruppacher, H. R. (1985). A Theoretical Study of the Wet Removal of Atmospheric Pollutants. Part I: The Redistribution of Aerosol Particles Captured through Nucleation and Impaction Scavenging by Growing Cloud Drops. *Journal of Atmospheric Sciences*, 42(6):583–606.

Fuzzi, S., Laj, P., Ricci, L., Orsi, G., Heintzenberg, J., Wendisch, M., Yuskiewicz, B., Mertes, S., Orsini, D., and Schwanz, M. (1998). Overview of the Po Valley fog experiment 1994 (CHEMDROP). *Contributions to atmospheric physics*, 71(1):3–19.

García-Díez, M., Fernández, J., Fita, L., and Yagüe, C. (2013). Seasonal dependence of WRF model biases and sensitivity to PBL schemes over Europe. *Quarterly Journal of the Royal Meteorological Society*, 139(671):501–514.

Garland, J. A. (1971). Some fog droplet size distributions obtained by an impaction method. *Quarterly Journal of the Royal Meteorological Society*, 97(414):483–494.

Gautam, R., Hsu, N. C., Kafatos, M., and Tsay, S. C. (2007). Influences of winter haze on fog/low cloud over the Indo-Gangetic plains. *Journal of Geophysical Research Atmospheres*, 112(5):1–11.

Geresdi, I., Rasmussen, R., Grabowski, W., and Bernstein, B. (2005). Sensitivity of freezing drizzle formation in stably stratified clouds to ice processes. *Meteorology and Atmospheric Physics*, 88(1-2):91–105.

Ghude, S. D., Bhat, G. S., Prabhakaran, T., Jenamani, R. K., Chate, D. M., Safai, P. D., Karipot, A. K., Konwar, M., Pithani, P., Sinha, V., Rao, P. S., Dixit, S. A., Tiwari, S., Todekar, K., Varpe, S., Srivastava, A. K., Bisht, D. S., Murugavel, P., Ali, K., Mina, U., Dharua, M., Jaya Rao, Y., Padmakumari, B., Hazra, A., Nigam, N., Shende, U., Lal, D. M., Chandra, B. P., Mishra, A. K., Kumar, A., Hakkim, H., Pawar, H., Acharja, P., Kulkarni, R., Subharthi, C., Balaji, B., Varghese, M., Bera, S., and Rajeevan, M. (2017). Winter fog experiment over the Indo-Gangetic plains of India. *Current Science*, 112(4):767–784.

Gilardoni, S., Massoli, P., Giulianelli, L., Rinaldi, M., Paglione, M., Pollini, F., Lanconelli, C., Poluzzi, V., Carbone, S., Hillamo, R., Facchini, M., and Fuzzi, S. (2014). Fog scavenging of organic and inorganic aerosol in the po valley. *Atmospheric Chemistry and Physics*, 14(13):6967–6981.

Ginoux, P., Chin, M., Tegen, I., Goddard, T., and In, G. (2001). model Brent Holben •' Oleg Dubovik •,•' and Shian-Jiann Lin e CART) model . In this model all topographic from

the Goddard Earth Observing System Data Assimilation System (GEOS emission is estimated to be between. *2-Journal of Geophysical Research*, 106:20255–20273.

Giulianelli, L., Gilardoni, S., Tarozzi, L., Rinaldi, M., Decesari, S., Carbone, C., Facchini, M. C., and Fuzzi, S. (2014). Fog occurrence and chemical composition in the Po valley over the last twenty years. *Atmospheric Environment*, 98:394–401.

Goldsmith, P., Delafield, H. J., and Cox, L. C. (1963). The role of diffusiophoresis in the scavenging of radioactive particles from the atmosphere. *Quarterly Journal of the Royal Meteorological Society*, 89(379):43–61.

Gultepe, I. (2007). *Fog and Boundary Layer Clouds: Fog Visibility and Forecasting*.

Gultepe, I. (2019). Low-Level Ice Clouds-Ice Fog. *Encylopedia of Water: Science, Technology, and Society*, pages 1–19.

Gultepe, I., Müller, M. D., and Boybeyi, Z. (2006a). A new visibility parameterization for warm-fog applications in numerical weather prediction models. *Journal of Applied Meteorology and Climatology*, 45(11):1469–1480.

Gultepe, I., Müller, M. D., and Boybeyi, Z. (2006b). A new visibility parameterization for warm-fog applications in numerical weather prediction models. *Journal of Applied Meteorology and Climatology*, 45(11):1469–1480.

Gultepe, I., Tardif, R., Michaelides, S. C., Cermak, J., Bott, A., Bendix, J., Müller, M. D., Pagowski, M., Hansen, B., Ellrod, G., Jacobs, W., Toth, G., and Cober, S. G. (2007). Fog research: A review of past achievements and future perspectives.

Gundel, L. A., Benner, W. H., and Hansen, A. D. (1994). Chemical composition of fog water and interstitial aerosol in Berkeley, California. *Atmospheric Environment*, 28(16):2715–2725.

Hong, S. Y., Noh, Y., and Dudhia, J. (2006). A new vertical diffusion package with an explicit treatment of entrainment processes. *Monthly Weather Review*, 134(9):2318–2341.

Iacono, M. J., Delamere, J. S., Mlawer, E. J., Shephard, M. W., Clough, S. A., and Collins, W. D. (2008). Radiative forcing by long-lived greenhouse gases: Calculations with the AER radiative transfer models. *Journal of Geophysical Research: Atmospheres*, 113(D13).

Izhar, S., Gupta, T., and Panday, A. K. (2020). Scavenging efficiency of water soluble inorganic and organic aerosols by fog droplets in the Indo Gangetic Plain. *Atmospheric Research*, 235(November 2019):104767.

Jeevan Kumar, B., Geresdi, I., Ghude, S. D., and Salma, I. (2021). Numerical simulation of the microphysics and liquid chemical processes occur in fog using size resolving bin scheme. *Atmospheric Research*, 266(August 2021):105972.

Jenamani, R. K. (2007). Alarming rise in fog and pollution causing a fall in maximum temperature over Delhi. *Current Science*, pages 314–322.

Kelvin, L. (1998). differential analyzer (1870). *Science Museum of Aarhus, Denmark*.

Kerminen, V. M. and Wexler, A. S. (1995). Growth laws for atmospheric aerosol particles: An examination of the bimodality of the accumulation mode. *Atmospheric Environment*, 29(22):3263–3275.

Köhler, H. (1936). The nucleus in and the growth of hygroscopic droplets. *Transactions of the Faraday Society*, 32(1152):1152–1161.

Kunkel, B. A. (1982). Microphysical Properties of Fog at Otis AFB. *Environmental Research Papers*, page 113.

Li, P., Li, X., Yang, C., Wang, X., Chen, J., and Collett, J. L. (2011). Fog water chemistry in Shanghai. *Atmospheric Environment*, 45(24):4034–4041.

Mazoyer, M., Burnet, F., Denjean, C., Roberts, G. C., Dupont, J.-C., and Elias, T. (2019). Experimental study of the aerosol impact on fog microphysics at the Instrumented Site for Atmospheric Remote Sensing. *Atmos. Chem. Phys*, 19:4323–4344.

Meng, Z. and Seinfeld, J. H. (1994). On the Source of the submicrometer droplet mode of urban and regional aerosols. *Aerosol Science and Technology*, 20(3):253–265.

Mihailovic, D. T. (2006). Impact of local and non-local eddy-diffusivity schemes on calculating the concentration of pollutants in environmental models. *Proceedings of the iEMSs 3rd Biennial Meeting," Summit on Environmental Modelling and Software"*, (January 2006).

Mohan, M. and Payra, S. (2009). Influence of aerosol spectrum and air pollutants on fog formation in urban environment of megacity Delhi, India. *Environmental monitoring and assessment*, 151(1):265–277.

Mohan, M. and Payra, S. (2014). Aerosol number concentrations and visibility during dense fog over a subtropical urban site. *Journal of Nanomaterials*, 2014.

Molnár, A., Bécsi, Z., Imre, K., Gácser, V., and Ferenczi, Z. (2016). Characterization of background aerosol properties during a wintertime smog episode. *Aerosol and Air Quality Research*, 16(8):1793–1804.

Molnár, A., Imre, K., Ferenczi, Z., Kiss, G., and Gelencsér, A. (2020). Aerosol hygroscopicity: Hygroscopic growth proxy based on visibility for low-cost PM monitoring. *Atmospheric Research*, 236(November 2019):104815.

Moore, K. F., Sherman, D. E., Reilly, J. E., Hannigan, M. P., Lee, T., and Collett, J. L. (2004). Drop size-dependent chemical composition of clouds and fogs. Part II: Relevance to interpreting the aerosol/trace gas/fog system. *Atmospheric Environment*, 38(10):1403–1415.

Morrison, H., Tessendorf, S. A., Ikeda, K., and Thompson, G. (2012). Sensitivity of a simulated midlatitude squall line to parameterization of raindrop breakup. *Monthly Weather Review*, 140(8):2437–2460.

Müller, M. D., Masbou, M., and Bott, A. (2010). Three-dimensional fog forecasting in complex terrain. *Quarterly Journal of the Royal Meteorological Society*, 136(653):2189–2202.

Nakanishi, M. and Niino, H. (2006). An improved Mellor-Yamada Level-3 model: Its numerical stability and application to a regional prediction of advection fog. *Boundary-Layer Meteorology*, 119(2):397–407.

Nakao, S., Suda, S. R., Camp, M., Petters, M. D., and Kreidenweis, S. M. (2014). Droplet activation of wet particles: Development of the Wet CCN approach. *Atmospheric Measurement Techniques*, 7(7):2227–2241.

Nath, S. and Yadav, S. (2018). A comparative study on fog and dew water chemistry at New Delhi, India. *Aerosol and Air Quality Research*, 18(1):26–36.

Nieberding, F., Breuer, B., Braeckevelt, E., Klemm, O., Song, Q., and Zhang, Y. (2018). Fog water chemical composition on ailaoshan mountain, Yunnan province, SW China. *Aerosol and Air Quality Research*, 18(1):37–48.

Niranjan, K., Sreekanth, V., Madhavan, B. L., and Krishna Moorthy, K. (2007). Aerosol physical properties and Radiative forcing at the outflow region from the Indo-Gangetic plains during typical clear and hazy periods of wintertime. *Geophysical Research Letters*, 34(19).

Pandis, S. N. and Seinfeld, J. H. (1989). Mathematical modeling of acid deposition due to radiation fog. *Journal of Geophysical Research*, 94(D10):12911.

Pasricha, P. K., Gera, B. S., Shastri, S., Maini, H. K., John, T., Ghosh, A. B., Tiwari, M. K., and Garg, S. C. (2003). Role of the water vapour greenhouse effect in the forecasting of fog occurrence. *Boundary-layer meteorology*, 107(2):469–482.

Petters, M. D. and Kreidenweis, S. M. (2007). A single parameter representation of hygroscopic growth and cloud condensation nucleus activity. *Atmospheric Chemistry and Physics Discussions*, 6(5):8435–8456.

Pithani, P., Ghude, S. D., Chennu, V. N., Kulkarni, R. G., Steeneveld, G. J., Sharma, A., Prabhakaran, T., Chate, D. M., Gultepe, I., Jenamani, R. K., and Madhavan, R. (2019). WRF Model Prediction of a Dense Fog Event Occurred During the Winter Fog Experiment (WIFEX). *Pure and Applied Geophysics*, 176(4):1827–1846.

Pithani, P., Ghude, S. D., Jenamani, R. K., Biswas, M., Naidu, C. V., Debnath, S., Kulkarni, R., Dhangar, N. G., Jena, C., Hazra, A., Phani, R., Mukhopadhyay, P., Prabhakaran, T., Nanjundiah, R. S., and Rajeevan, M. (2020). Real-Time Forecast of Dense Fog Events over Delhi: The Performance of the WRF Model during the WiFEX Field Campaign. *Weather and Forecasting*, 35(2):739–756.

Pithani, P., Ghude, S. D., Prabhakaran, T., Karipot, A., Hazra, A., Kulkarni, R., Chowdhuri, S., Resmi, E. A., Konwar, M., Murugavel, P., Safai, P. D., Chate, D. M., Tiwari, Y., Jenamani, R. K., and Rajeevan, M. (2018). WRF model sensitivity to choice of PBL and microphysics parameterization for an advection fog event at Barkachha, rural site in the Indo-Gangetic basin, India. *Theoretical and Applied Climatology*, (Stull 1988):1–15.

Pleim, J. E. (2007). A combined local and nonlocal closure model for the atmospheric boundary layer. Part II: Application and evaluation in a mesoscale meteorological model. *Journal of Applied Meteorology and Climatology*, 46(9):1396–1409.

Pringle, K. J., Tost, H., Pozzer, A., Pöschl, U., and Lelieveld, J. (2010). Global distribution of the effective aerosol hygroscopicity parameter for CCN activation. *Atmospheric Chemistry and Physics*, 10(12):5241–5255.

Pruppacher, H. and Klett, J. (2010). *Microphysics of Clouds and Precipitation*, volume 18 of *Atmospheric and Oceanographic Sciences Library*. Springer Netherlands, Dordrecht.

Pruppacher, H. R., Klett, J. D., and Wang, P. K. (1998). Microphysics of Clouds and Precipitation. *Aerosol Science and Technology*, 28(4):381–382.

Quaas, J., Gilardoni, S., Massoli, P., Giulianelli, L., Rinaldi, M., Paglione, M., Pollini, F., Lanconelli, C., Poluzzi, V., Carbone, S., Hillamo, R., Russell, L. M., Facchini, M. C., Fuzzi, S., Ardon-Dryer, K., Huang, Y. W., Cziczo, D. J., Hung, H. M., Lu, W. J., Chen, W. N., Chang, C. C., Chou, C. C., Lin, P. H., Thesis, D., Poku, C., Ross, A. N., Blyth, A. M., Hill, A. A., and Price, J. D. (2014). Fog scavenging of organic and inorganic aerosol in the po valley. *Atmospheric Chemistry and Physics*, 14(4):6967–6981.

Raoult, F.-M. (1887). Loi générale des tensions de vapeur des dissolvants. *CR Hebd. Seances Acad. Sci*, 104:1430–1433.

Rockel, B., Will, A., and Hense, A. (2008). The regional climate model COSMO-CLM (CCLM). *Meteorologische Zeitschrift*, 17(4):347–348.

Román-Cascón, C., Yagüe, C., Steeneveld, G. J., Morales, G., Arrillaga, J. A., Sastre, M., and Maqueda, G. (2019). Radiation and cloud-base lowering fog events: Observational analysis and evaluation of WRF and HARMONIE. *Atmospheric Research*, 229(May):190–207.

Safai, P. D., Ghude, S., Pithani, P., Varpe, S., Kulkarni, R., Todekar, K., Tiwari, S., Chate, D. M., Prabhakaran, T., Jenamani, R. K., and Rajeevan, M. N. (2018). Two Way Relationship between Aerosols and Fog: A Case Study at IGI Airport, New Delhi. *Aerosol and Air Quality Research*, pages 71–79.

Safai, P. D., Kewat, S., Pandithurai, G., Praveen, P. S., Ali, K., Tiwari, S., Rao, P. S. P., Budhawant, K. B., Saha, S. K., and Devara, P. C. S. (2008). Aerosol characteristics during winter fog at Agra, North India. *Journal of atmospheric chemistry*, 61(2):101–118.

Saito, K., Fujita, T., Yamada, Y., Ishida, J. I., Kumagai, Y., Aranami, K., Ohmori, S., Nagasawa,

R., Kumagai, S., Muroi, C., Kato, T., Eito, H., and Yamazaki, Y. (2006). The operational JMA nonhydrostatic mesoscale model. *Monthly Weather Review*, 134(4):1266–1298.

Salma, I., Németh, Z., Kerminen, V. M., Aalto, P., Nieminen, T., Weidinger, T., Molnár, Á., Imre, K., and Kulmala, M. (2016). Regional effect on urban atmospheric nucleation. *Atmospheric Chemistry and Physics*, 16(14):8715–8728.

Santachiara, G., Prodi, F., and Belosi, F. (2012). A Review of Termo- and Diffusio-Phoresis in the Atmospheric Aerosol Scavenging Process . Part 1 : Drop Scavenging. 2012(April):148–158.

Santachiara, G., Prodi, F., and Belosi, F. (2013). Atmospheric aerosol scavenging processes and the role of thermo- and diffusio-phoretic forces. *Atmospheric Research*, 128:46–56.

Sawaisarje, G., Khare, P., Shirke, C., Deepakumar, S., and Narkhede, N. (2014). Study of winter fog over indian subcontinent: Climatological perspectives. *Mausam*, 65(1):19–28.

Schmeller, G. and Geresdi, I. (2019). Study of interaction between cloud microphysics and chemistry using coupled bin microphysics and bin aqueous chemistry scheme. *Atmospheric Environment*, 198(November 2018):366–380.

Silverman, B. A., Weinstein, A. I., and Hess, W. (1974). Fog, in Weather and Climate Modification.

Skamarock, W. C., Klemp, J. B., Dudhia, J. B., Gill, D. O., Barker, D. M., Duda, M. G., Huang, X.-Y., Wang, W., and Powers, J. G. (2008). A description of the Advanced Research WRF Version 3, NCAR Technical Note TN-475+STR. *Technical Report*, (June):113.

Smith, D. K., Renfrew, I. A., Dorling, S. R., Price, J. D., and Boutle, I. A. (2021). Sub-km scale numerical weather prediction model simulations of radiation fog. *Quarterly Journal of the Royal Meteorological Society*, 147(735):746–763.

Song, J. I., Yum, S. S., Gultepe, I., Chang, K. H., and Kim, B. G. (2019). Development of a new visibility parameterization based on the measurement of fog microphysics at a mountain site in Korea. *Atmospheric Research*, 229(June):115–126.

Steinfeld, J. I. (1998). Atmospheric chemistry and physics: from air pollution to climate change. *Environment: Science and Policy for Sustainable Development*, 40(7):26.

Straub, D. J. (2017). Radiation fog chemical composition and its temporal trend over an eight year period. *Atmospheric Environment*, 148:49–61.

Sukoriansky, S., Galperin, B., and Perov, V. (2005). Application of a new spectral theory of stably stratified turbulence to the atmospheric boundary layer over sea ice. *Boundary-Layer Meteorology*, 117(2):231–257.

Syed, F. S., Körnich, H., and Tjernström, M. (2012). On the fog variability over south Asia. *Climate dynamics*, 39(12):2993–3005.

Terry, J. P., Jia, G., Boldi, R., and Khan, S. (2018). The Delhi 'gas chamber': Smog, air pollution and the health emergency of November 2017. *Weather*, (November).

Thompson, G. and Eidhammer, T. (2014). A study of aerosol impacts on clouds and precipitation development in a large winter cyclone. *Journal of the Atmospheric Sciences*, 71(10):3636–3658.

Twomey, S. (1984). Pollution and the Planetary Albedo. *Atmospheric Environment*, 41(SUPPL.):120–125.

Vautard, R., Yiou, P., and Van Oldenborgh, G. J. (2009). Decline of fog, mist and haze in Europe over the past 30 years. *Nature Geoscience*, 2(2):115–119.

Wang, G., Zhang, R., Gomez, M. E., Yang, L., Zamora, M. L., Hu, M., Lin, Y., Peng, J., Guo, S., Meng, J., Li, J., Cheng, C., Hu, T., Ren, Y., Wang, Y., Gao, J., Cao, J., An, Z., Zhou, W., Li, G., Wang, J., Tian, P., Marrero-Ortiz, W., Secrest, J., Du, Z., Zheng, J., Shang, D., Zeng, L., Shao, M., Wang, W., Huang, Y., Wang, Y., Zhu, Y., Li, Y., Hu, J., Pan, B., Cai, L., Cheng, Y., Ji, Y., Zhang, F., Rosenfeld, D., Liss, P. S., Duce, R. A., Kolb, C. E., and Molina, M. J. (2016). Persistent sulfate formation from London Fog to Chinese haze. *Proceedings of the National Academy of Sciences of the United States of America*, 113(48):13630–13635.

Wang, J., Li, J., Ye, J., Zhao, J., Wu, Y., Hu, J., Liu, D., Nie, D., Shen, F., Huang, X., Huang, D. D., Ji, D., Sun, X., Xu, W., Guo, J., Song, S., Qin, Y., Liu, P., Turner, J. R., Lee, H. C., Hwang, S., Liao, H., Martin, S. T., Zhang, Q., Chen, M., Sun, Y., Ge, X., and Jacob, D. J. (2020). Fast sulfate formation from oxidation of SO2 by NO2 and HONO observed in Beijing haze. *Nature Communications*, 11(1):1–7.

Wang, X., Shen, X. J., Sun, J. Y., Zhang, X. Y., Wang, Y. Q., Zhang, Y. M., Wang, P., Xia, C., Qi, X. F., and Zhong, J. T. (2018). Size-resolved hygroscopic behavior of atmospheric aerosols

during heavy aerosol pollution episodes in Beijing in December 2016. *Atmospheric Environment*, 194(September):188–197.

Wang, X., Ye, X., Chen, H., Chen, J., Yang, X., and Gross, D. S. (2014). Online hygroscopicity and chemical measurement of urban aerosol in Shanghai, China. *Atmospheric Environment*, 95:318–326.

William C. Skamarock, Joseph B. Klemp, Jimy Dudhia, David O. Gill, Dale M. Barker, Michael G. Duda, Xiang-Yu Huang, Wei Wang, J. G. P. (2001). Advanced Research WRF. *Journal of Continuing Higher Education*, 49(2):14–22.

Young, K. C. (1993). *Microphysical processes in clouds*. Oxford University Press.

Zhang, J., Liu, Y., Cui, L. L., Liu, S. Q., Yin, X. X., and Li, H. C. (2017). Ambient air pollution, smog episodes and mortality in Jinan, China. *Scientific Reports*, 7(1):1–8.